TEST-CASE: HPP Schiffmühle, Switzerland

Prepared by Ismail Albayrak[1,1], Muhammadreza Maddahi[1], Cristina Rachelly[1], Martin Detert[1], Robert Boes[1], Armin Peter[2], Nils Schölzel[2], Christian Milzow[3], Lisa Heidler[3] Chidambaram Narayanan[3], Andrew Carlson[3], Jeffry Tuhtan[4], Kordula Schwarzwälder[5], Nils Ruther[5], Andreas Doessegger[6]

[1]VAW, ETH Zurich, [2]FCO, [3]AFRY AG (former AF-Consult), [4]TUT, [5]NTNU and [6]LKW

[1,1]Responsible person: albayrak@vaw.baug.ethz.ch

Updated on 30.10.2020.

Table of Contents

Figures

Tables

1 Description of the Test-Case

1.1 Description of the water bodies related to the HPP

The residual flow and main run-of-river hydropower plants (HPPs) Schiffmühle are located on the 35 km long river Limmat in Untersiggenthal and Turgi near Baden, some 27 km downstream of Lake Zurich. Between Lake Zurich and Schiffmühle there are seven HPPs, namely in flow direction Letten, Höngg, Dietikon, Wettingen, Aue, Oederlin and Kappelerhof (Fig.1). There are three more power plants between HPP Schiffmühle and the junction with river Aare, namely Turgi, Gebenstorf and Stroppel. Altitudes of the lowest and highest points of river Limmat are 330 m and 406 m asl, respectively, resulting in an average bed slope of 2.2 per mil. The surface area of the whole catchment amounts to 2384 km^2, of which 0.7 % are glaciated.

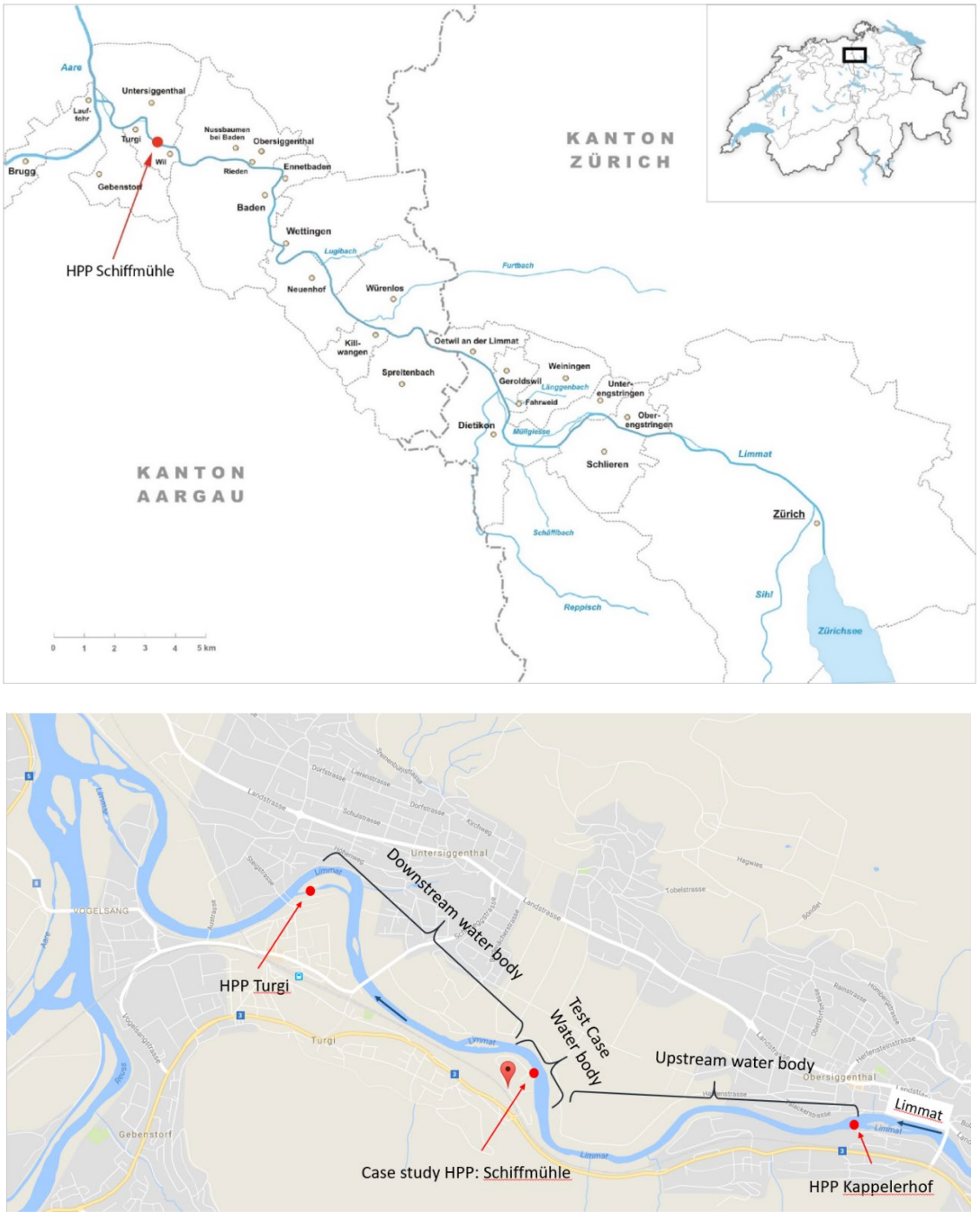

Figure 1: Water bodies related to the HPP Schiffmühle.

1.1.1 Hydrology of river Limmat

On river Limmat, the mean monthly discharge increases from March to June and then decreases until autumn (Fig. 2). The mean annual discharge in 2015 was 89 m^3/s (Fig. 2), while the long-term average is 101 m^3/s (1951-2015).

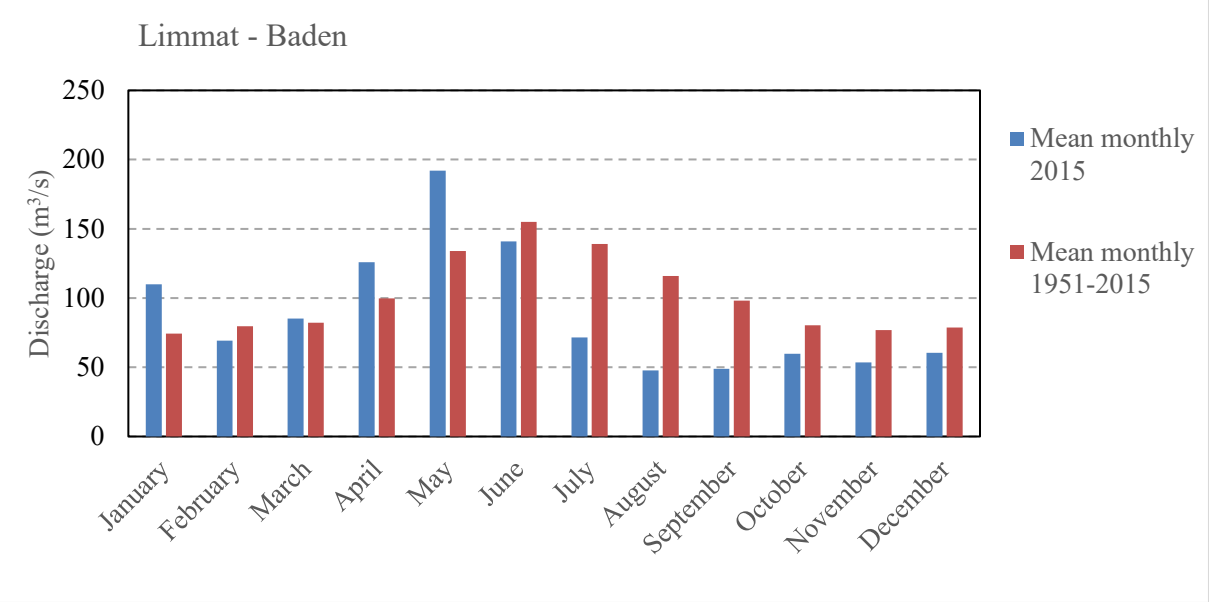

Figure 2: Mean monthly discharge of river Limmat at Baden (AG) (source: https://www.hydrodaten.admin.ch).

1.1.2 Main pressures

River Limmat is located in the river Rhine catchment, which was historically one of the most important Atlantic salmon rivers in Europe. The upstream migration of salmons (*Salmo Salar*) in the Rhine catchment became almost impossible due to transverse structures such as hydropower plants. In the past few years most of the HPPs at the river Limmat have been equipped with state-of-the-art fish upstream passage facilities. However, downstream migration measures and sediment management strategies are not entirely realized at each HPP in river Limmat. The following domestic species face potential mortality during downstream migration, or difficulties during upstream migration in the Limmat catchment. All of the occurring fish species (28 fish species, 2 of them non-native species) in the river Limmat are facing potential mortality during the downstream migration. Some of the most important species are:

- Eel (*Anguilla anguilla*)
- Brown trout
- Common barbel (*Barbus Barbus*)
- Grayling
- Spirlin
- Nase
- Chub
- Bleak
- Roach
- Perch

Before the year 1938, two anadromous species were present in the Limmat River (Atlantic Salmon and the European river lamprey, Voser & Bolliger 2004). Furthermore, river Limmat is highly influenced by HPPs and densely populated areas and considered as a heavily modified water body. The river has a moderate ecological potential. Various measures for sediment continuity, fish migration, flow changes, habitat in-channel and morphology off-channel have been implemented in the water body. In particular, an innovative vortex tube for bed load transport continuity, sediment flushing through weirs and upstream and downstream fish migration facilities have been installed and are in operation at the residual flow HPP Schiffmühle. Mitigation measures in River Basin Managements Plans, which are not yet implemented in the Limmat river, are: fish monitoring, restoration of upstream fish migration facilities along all HPPs in river Limmat and planning and implementation of fish protection and downstream fish migration measures.

1.2 Presentation of the HPP

At Schiffmühle, hydropower is exploited in two run-of-river HPPs on river Limmat, namely the main powerhouse located at the end of a headrace channel on the right shore and the residual flow HPP situated next to a flap gate at the upstream end of the weir on the left shore. They are located in the communities of Untersiggenthal and Turgi near Baden. The characteristics of both HPPs are listed in Table 1. Figures 3 and 4 show the locations and close-up photos of the HPPs, respectively. In the scope of FIThydro, the residual flow HPP is the case study HPP and hereafter referred as 'HPP Schiffmühle'.

1.2.1 Location of the HPP

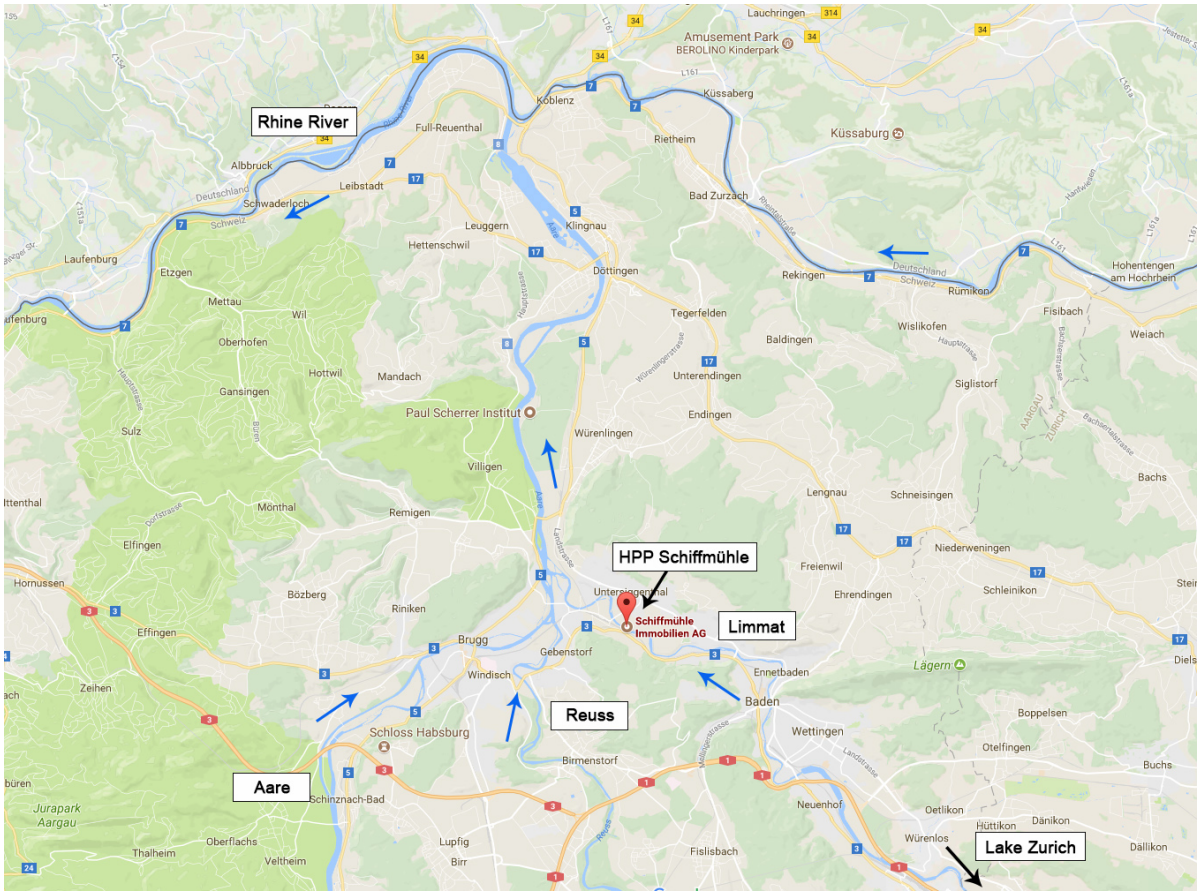

Figure 3: Location of HPP Schiffmühle.

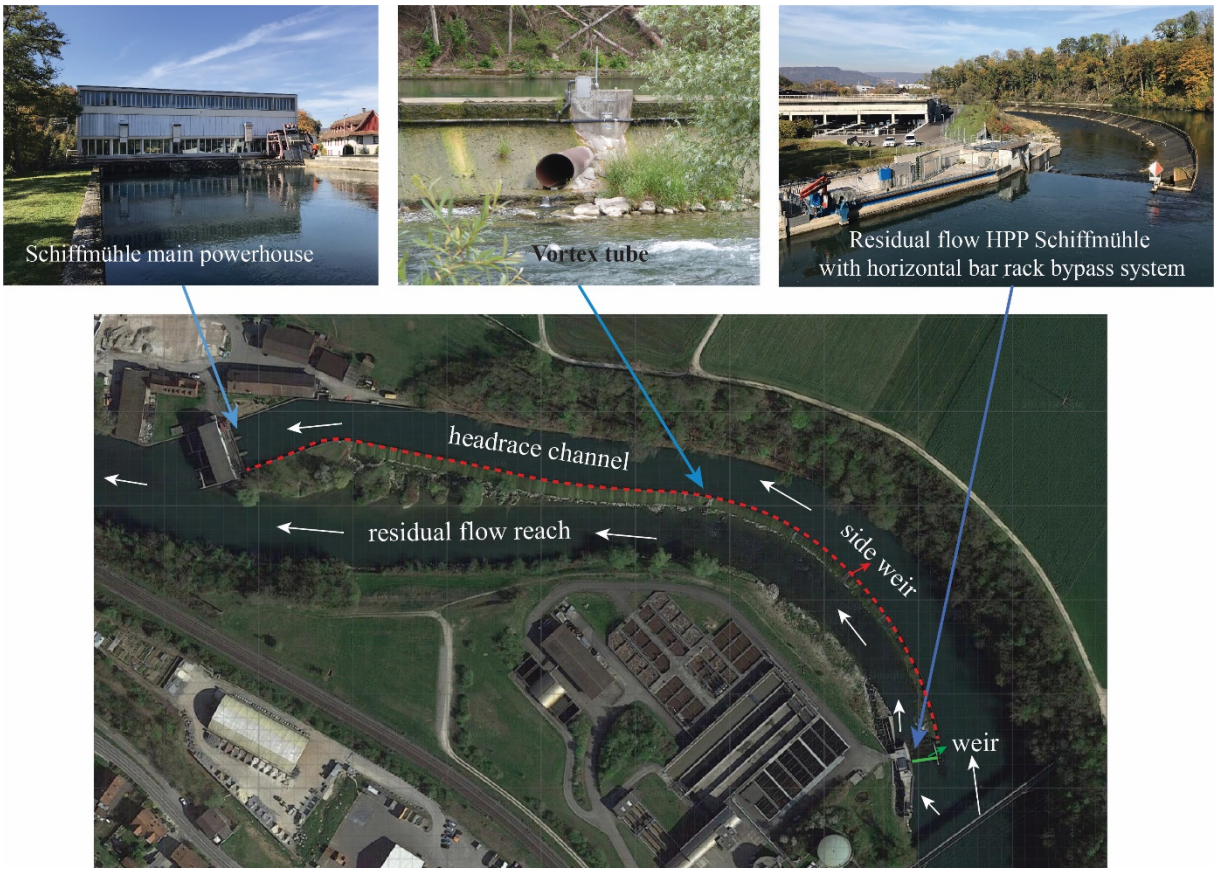

Figure 4: Schiffmühle main powerhouse and residual flow HPP.

Table 1: Main characteristics of the HPPs Schiffmühle

	Schiffmühle main powerhouse	Schiffmühle residual flow HPP
Watercourse	Limmat	
Location :	Untersiggenthal and Turgi near Baden	
Mean annual discharge (1951-2015)	101 m^3/s	
Design discharge	108 m^3/s	14 m^3/s
Head	3.2 m	2.97 m
Capacity	3.46 MW (three vertical Kaplan turbines)	0.50 MW (bevel gear bulb turbine)
Species concerned :	26 fish species known; target species barbel, sprilin, trout, grayling. Salmon expected in the next 10 - 20 years	

1.2.2 E-flow

The HPP Schiffmühle supplies up to 14.00 m^3/s of turbine water and 0.67 m^3/s of the water in the fish passes (upstream and downstream) to the downstream river reach as e-flow. Moreover, during high river discharges, additional water is supplied over the frontal weir at the HPP and over the side weir along the power canal to the residual flow reach (Fig. 4).

1.2.3 Downstream migration devices

At HPP Schiffmühle, an angled fish guidance structure with horizontal bars and a bypass, i.e. a Horizontal Bar Rack Bypass System (HBR-BS), has been implemented in 2013 to protect and guide fish to the downstream of the HPP (Fig. 5). The rack is positioned almost parallel to the main flow to have a lateral intake. The specifications of the HBR-BS are:

- Length of HBR : 14.60 m
- Height of HBR:1.82 m
- Total height of turbine intake: 2.32 m
- Angle of HBR to horizontal: 90°
- Clearance between the bars : 20 mm
- The bars have rectangular profiles/cross section.
- The approach flow velocity at design discharge is 0.5 m/s.
- At the end of the rack there is a bypass with two openings in a vertical chamber at different water depths (close to the bottom and close to the water surface).
- A 25 cm diameter pipe bypasses fish from the chamber to the tailwater reach
- Design discharge of the bypass pipe: 170 l/s
- Bypass pipe outlet is about 0.2 m above the tailwater
- 1 PIT-tag antenna has been installed at the bypass to monitor downstream migrating fish

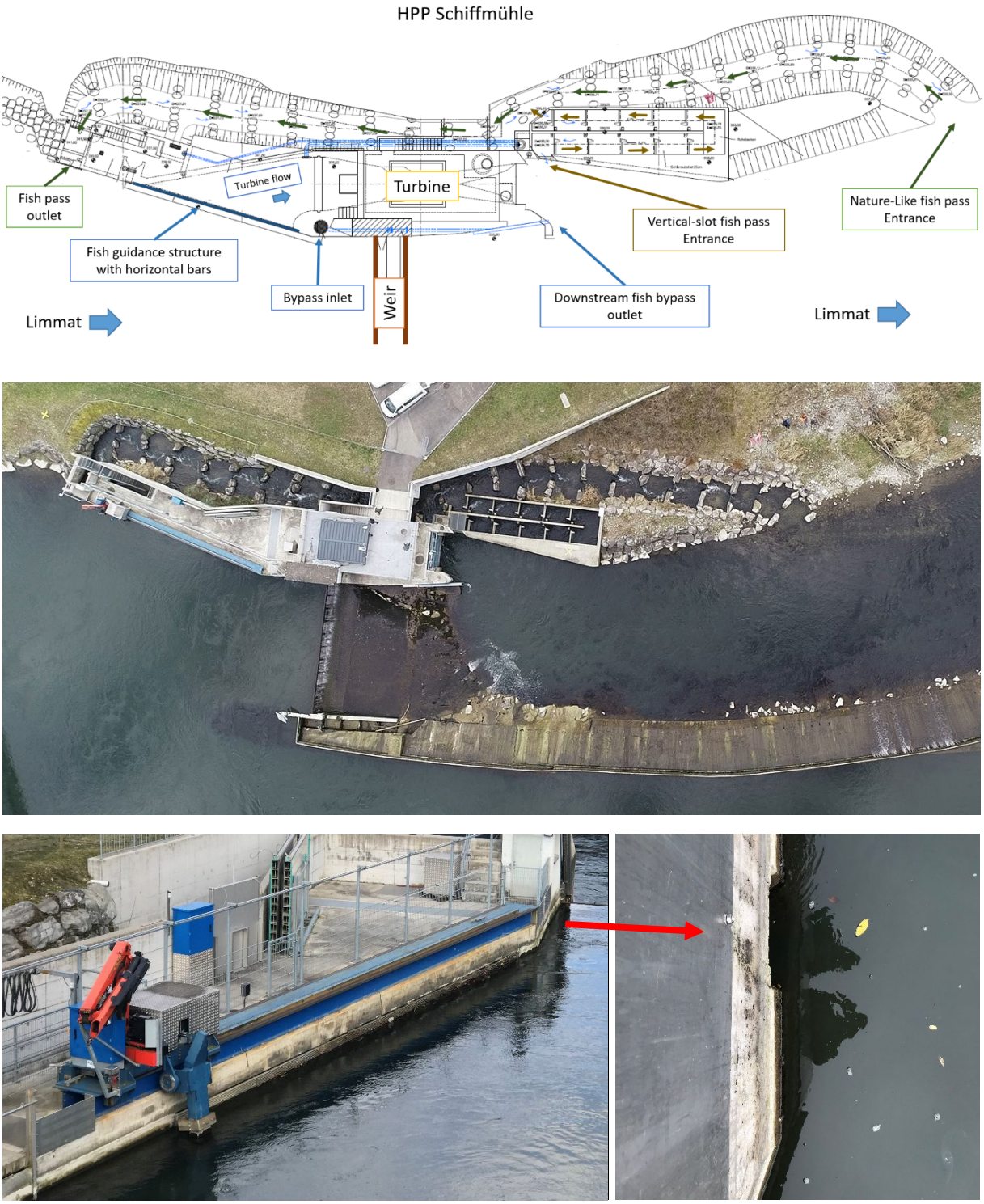

Figure 5: Plan view illustration (top), photo (middle) of HPP Schiffmühle and close-up photo of HBR & bypass inlet (bottom).

1.2.4 Upstream migration devices

The residual flow HPP Schiffmühle has a combination of a Vertical Slot Fish Pass (VSFP) and Nature-Like Fish Pass (NLFP) for upstream migration (Figs. 5 and 6). The specifications of the fish passes are:

- The NLFP entrance is located approx. 36 m downstream of the turbine flow outlet (Figs. 5, 6)
- The bottom slope of the NLFP is on average approx. 4 %.
- The VSFP entrance is located 2 m downstream of the turbine flow outlet (Figs. 5, 6)
- The bottom slope of the VSFP is approx. 6.28%
- The outlet of the VSFP is merged to the NLFP at an elevation of 336.83 m a.s.l.
- Total discharge in both fish passes : 0.5 m^3/s
- 5 PIT-tag antennas have been installed in the technical vertical slot fish pass and in the nature-like bypass to monitor upstream migration and fish behaviour in the migration facilities.

Figure 6: Nature-like and vertical-slot fish passes of HPP Schiffmühle.

1.2.5 Sediment management

The bedload transport continuity in the Limmat River is strongly impacted by its channelization realized in the 19th century and twelve hydropower plants along its course. The pre-industrial natural bedload transport rate in the reach of HPP Schiffmühle was estimated at 2'000-2'500 m^3/a, whereas today, it is reduced to a few 100 m^3/a, thus the bedload transport can be described as supply-limited. With the execution of multiple bedload restoration measures currently planned along the Limmat River in the context of the Swiss Water Protection Act, the bedload transport rate is estimated to increase again to 1'000-1'100 m^3/a over the next 10 to 15 years (Flussbau AG, 2017).

Due to the location of the frontal weir of HPP Schiffmühle in the crossover of a right to a left bend (Figure 1), considerable amounts of bedload are entrained into and deposited along the headwater channel of the power plant. The HPP is thus classified as a significant impairment to bedload transport continuity (Flussbau AG, 2017). The accumulated gravel in the headwater channel not only causes the sediment deficit in the downstream reach to further intensify, but also generates operational problems. To maintain the operation of the HPP, the accumulated gravel in the headwater channel has to be extracted regularly. To save extraction costs and restore the bedload continuity, the operator of HPP Schiffmühle installed a vortex tube system to divert bedload from the headwater channel to the residual flow reach in 2003 (Figure 7) (VAW, 2001). The analysis of past gravel extraction records shows that less dredging has been necessary since the installation of the vortex tube. Nevertheless, gravel extraction

was necessary in September 2018 and a total volume of 5'300 m^3 was dredged and placed in the residual flow reach (Figure 7). It can be concluded that the vortex tube is diverting a fraction of the entrained gravel to the residual flow reach, but quantitative data on its diversion efficiency is lacking, which is addressed in the scope of the present project.

Figure 7: View of the side weir and the vortex tube at HPP Schiffmühle with the gravel extracted from the headwater channel dumped into the residual flow reach.

2 Objectives of this Test Case

What are we researching?

Downstream fish migration:

The fish guidance efficiency and hydraulics of the HBR-BS are investigated by:

- Fish monitoring using PIT-tagging technique
- Velocity measurements using ADCP
- Numerical modelling of HBR-BS and weir

Downstream impact of sediment management at HPPs:

The dynamic changes in bedload transport rates and total transported masses will be quantified and their effects on river ecology and morphology will be qualitatively evaluated by:

- Monitoring of bedload transport in the vortex tube using innovative instruments
- Bathymetry measurements around the HPP
- Habitat mapping, sediment sampling, shelter measurements and substrate characterization

Upstream fish migration and habitat modeling:

The effectiveness, attraction flow and potential migration pathways of the nature-like fishway and the technical fish pass (vertical slot) for upstream migration will be investigated, respectively, by:

- Fish monitoring using PIT-tagging technique
- Habitat simulation system (CASiMiR)
- Lateral Line Probe (LLP) measurements

Why do we conduct the above-listed studies at this Test case?

The test case site of HPP Schiffmühle is very practical due to its location near Zurich and is a representative small low-head run-of-river HPP. The re-licensing of the Schiffmühle main powerhouse in 2011 resulted in an increase in the volume of residual water to be delivered. The HPP owner, Limmatkraftwerke AG, decided to use the environmental water flow by means of a weir turbine for the generation of renewable electrical energy. This led to build the residual flow HPP Schiffmühle with a fish-friendly intake design with a horizontal bar rack and a pipe bypass system. With the construction of the HPP Schiffmühle, the HPP owner replaced the existing fish pass with a new one, consisting of vertical slot and natural-like fish passes. Due to the re-licensing, the HPP owner has started to monitor the effectiveness of fish passes not only at HPP Schiffmuhle but also at his upstream and downstream HPPs, which will provide a good data basis to assess fish migration in that reach of river Limmat. The planned studies at this HPP will address various aspects of fish passes, downstream habitat and sediment transport. The findings of the above listed studies will have a wide range of applications for other similarly sized HPPs and answer the fundamental questions on the fish behavior at fish passes.

What are we expecting?

We expect from this test case (I) to consolidate the design recommendations for fish-friendly water intakes, and technical and nature-like fish passes and (II) to advance in the understanding of the effect of HPP operation including bed load transport via vortex tube on the downstream fish habitat and hydraulics of fish passes on the potential fish migration pathways.

Relevance in FIThydro?

We will respond to some objectives of the project and WP2 such as application of the existing SMTDs on a test case, and will have feedbacks on their use and application range.

3 Presentation and results of activities in FIThydro

3.1 Monitoring of bedload transport through a vortex tube

3.1.1 Data

The negative impact of hydropower plants on the bedload continuity in the Limmat River is of strong interest for the assessment of habitat quality (section 3.4). HPP Schiffmühle is equipped with a vortex tube, a diversion structure for bedload. The vortex tube consists of a steel tube embedded in the side weir, connecting the headwater channel to the residual flow reach (Figure 8). The section of the tube extending into the headwater channel has a slot opening along its soffit and an open end. A gate valve is positioned in the side weir, which is automatically opened when a critical discharge is exceeded. When it is open, a spiral flow develops and bedload transported across the bed of the headwater channel may be entrained into the vortex tube and flushed to the residual flow reach by the combination of the approach flow and the pressure gradient between the headwater channel and the residual flow reach (Mtalo, 1988; Atkinson, 1994a; Atkinson, 1994b; Awasthi, 2001). To quantify the diversion efficiency of the vortex tube, three passive acoustic sensors, a geophone, an accelerometer, and a microphone, have been attached to the steel vortex tube (Gray et al., 2010). All measurements only concern the sediment transported as bedload, because suspended sediment transport is not an issue.

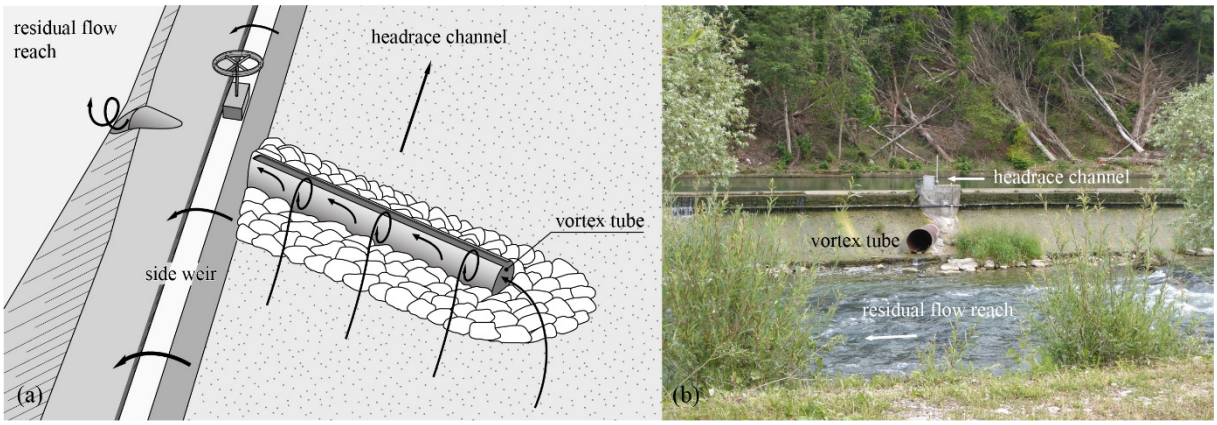

Figure 8: (a) Conceptual sketch of the vortex tube functionality and (b) the vortex tube at HPP Schiffmühle.

The gate valve operation is controlled by the discharge signal of the Swiss Federal Office for the Environment (FOEN) hydrometric station Baden, Limmatpromenade (Station ID 2243), approximately 4800 m upstream of the vortex tube. No major tributaries join the Limmat River in between. The gate valve is opened when the discharge exceeds Q_{open} = 150 m^3/s during the rising limb of a hydrograph and closes when the discharge falls below Q_{close} = 130 m^3/s during the receding limb. Since the beginning of October 2018, the vortex tube is also opened weekly for approximately 22 min, opening and closing time of approx. 5 min included. The goal of the operator is to more regularly divert bedload transported during discharges < Q_{open} into the residual flow reach. To test the functionality of the monitoring system, a test file of 2-4 s length is recorded every day at a set time.

The automatically recorded events up to December 23, 2019 can be sorted into the three main categories (i) flood events (17 events), (ii) weekly flushing (54 events), and (iii) tests (191 events). Figure 9 shows the data set collected until December 31, 2019, including unforeseen operational problems of the HPP or the data recording system. The geophone was installed first in April 2018, later followed by the installation of the accelerometer and the microphone in June 2018. Only the geophone data is thus available for the spring flood events of 2018.

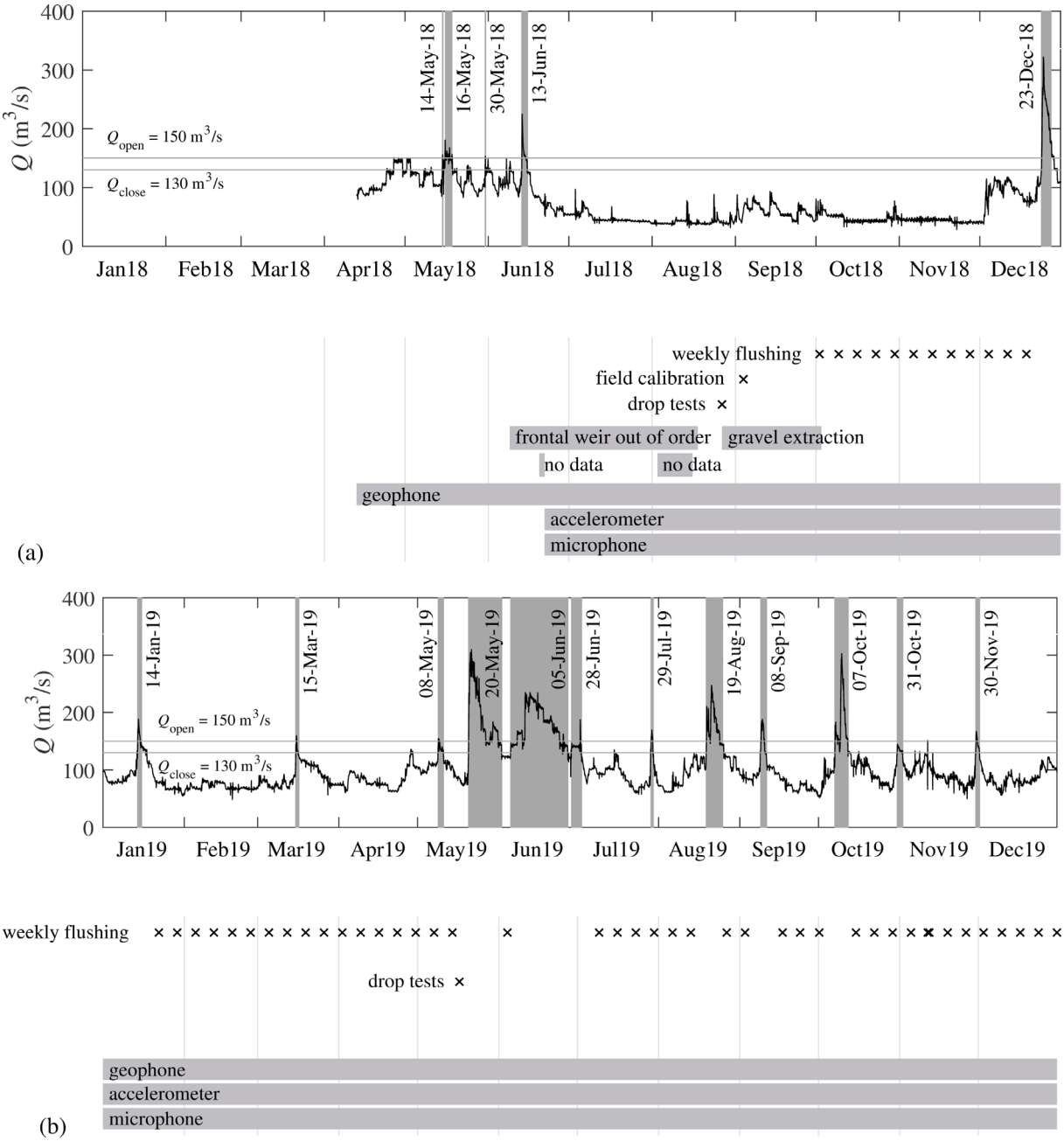

Figure 9: Overview of the dataset collected in the years (a) 2018 and (b) 2019. The vortex tube is automatically opened for $Q > Q_{open}$ and closed for $Q < Q_{close}$. Flood events are labeled with their start date. The bottom panel informs about the installation dates of the sensors and restrictions on the data availability due to operational problems of either the HPP or the data recording system. The test events are not displayed individually. (Discharge data: FOEN hydrometric station ID 2243).

Table 2 shows the characteristics of the recorded flood events. Due to difficulties with data storage during the 16-May-18 event, data is only available for 32.3% of its total duration. During the period marked ‘frontal weir out of order’, the discharge allocation to the headwater channel and the residual flow reach was not representative of normal operating conditions. Therefore, the pressure difference between the headwater channel and the residual flow reach may have influenced the hydraulic conditions and bedload transport in the vortex tube. For this reason, the flood 13-Jun-18 is excluded from the data analysis. Similarly, the first weekly flushing event is excluded due to ongoing gravel extraction works that may have influenced the functioning of the vortex tube.

Table 2 : Seventeen flood events that occurred between April 13, 2018 and December 31, 2019.

Notation	Start time (UTC)	End time (UTC)	Duration dd / hh:mm:ss	recorded (%)	Q_{max} (m^3/s)
14-May-18	2018/05/14 22:14:00	2018/05/15 01:24:05	-- / 03:10:05	100	155.7
16-May-18	2018/05/16 01:03:40	2018/05/18 09:47:33	02 / 08:43:53	32.3	180.9
30-May-18	2018/05/30 20:35:12	2018/05/30 23:12:16	-- / 02:37:04	100	153.2
13-Jun-18 *	2018/06/13 10:56:24	2018/06/15 12:56:29	02 / 02:00:05	100	224.8
23-Dec-18	2018/12/23 21:55:24	2018/12/27 09:57:51	03 / 12:02:27	100	321.9
14-Jan-19	2019/01/14 04:33:41	2019/10/15 16:32:22	01 / 11:58:41	100	188.5
15-Mar-19	2019/03/15 12:49:37	2019/03/16 15:57:41	01 / 03:08:04	100	159.5
08-May-19	2019/05/08 21:35:26	2019/05/10 20:49:31	01 / 23:14:05	100	154.6
20-May-19 **	2019/05/20 10:29:36	2019/06/02 02:07:52	12 / 15:38:16	100	309.7
05-Jun-19	2019/06/05 13:05:50	2019/06/27 07:47:11	21 / 18:41:21	tbd	235.1
28-Jun-19	2019/06/28 18:00:08	2019/07/02 13:35:14	03 / 19:35:06	tbd	187.4
29-Jul-19	2019/07/29 01:57:10	2019/07/29 20:52:14	-- / 18:55:04	tbd	169.4
19-Aug-19	2019/08/19 03:56:27	2019/08/25 09:11:27	06 / 05:15:00	tbd	247.5
08-Sep-19	2019/09/08 22:36:45	2019/09/11 03:40:50	02 / 05:04:05	tbd	188.3
07-Oct-19	2019/10/07 05:05:09	2019/10/12 06:10:17	05 / 01:05:08	tbd	302.7
31-Oct-19	2019/10/31 01:20:30	2019/11/02 02:41:35	02 / 01:21:05	tbd	144.9
30-Nov-19	2019/11/29 23:52:58	2019/12/01 10:54:03	01 / 11:01:05	tbd	167.1

* frontal weir out of order
** latest flood event currently processed

In this study, we aim to quantify (i) the total bedload volume and (ii) the grain size distribution of the bedload transported through the vortex tube, and (iii) to provide the operator of HPP Schiffmühle with recommendations on the vortex tube operation. A field calibration was performed to relate the obtained signals to bedload transport characteristics (Gray et al., 2010). In this report, only the analysis of the geophone data is shown.

3.1.2 Methodology

3.1.2.1 Passive acoustic sensors

Three passive acoustic sensors were installed on the vortex tube at HPP Schiffmühle to measure the oscillations of the steel tube caused by grain impacts. A geophone (GS-20DX manufactured by Geospace Technologies, Houston TX, USA), a single axis accelerometer (ICP352C03 manufactured by PCB Piezoelectronics, Depew NY, USA), and a microphone (ICP130A24 manufactured by PCB Piezoelectronics, Depew NY, USA) were mounted in a 0.22 m long, 0.12 m high, and 0.081 m deep, water-tight aluminum housing that was welded to the side of the vortex tube (Figure 10). All signals are recorded by an analog-digital converter with a sampling frequency of f_s = 51.2 kHz. These raw signals are then transmitted and further processed (see section 3.1.4).

Figure 10: The bedload monitoring setup with (a) the housing and the geophone and (b) the housing mounted to the vortex tube and all sensors installed.

3.1.2.2 Pressure sensor

In addition to the bedload monitoring sensors, a pressure sensor (26W manufactured by Keller AG, Winterthur, Switzerland) was installed next to the vortex tube outlet to record water levels in the residual flow reach relative to the vortex tube bottom (Figure 11). The sampling frequency is 1 min^{-1}, independent of the vortex tube operation. The information on the water level at the vortex tube outlet is of interest because the vibration signals may be influenced by submergence of the vortex tube outlet. Additionally, the diversion efficiency of the vortex tube is attenuated by a rising water level at the outlet (VAW, 2001; VAW, 2017). The pressure sensor data will not, however, be analyzed in this report.

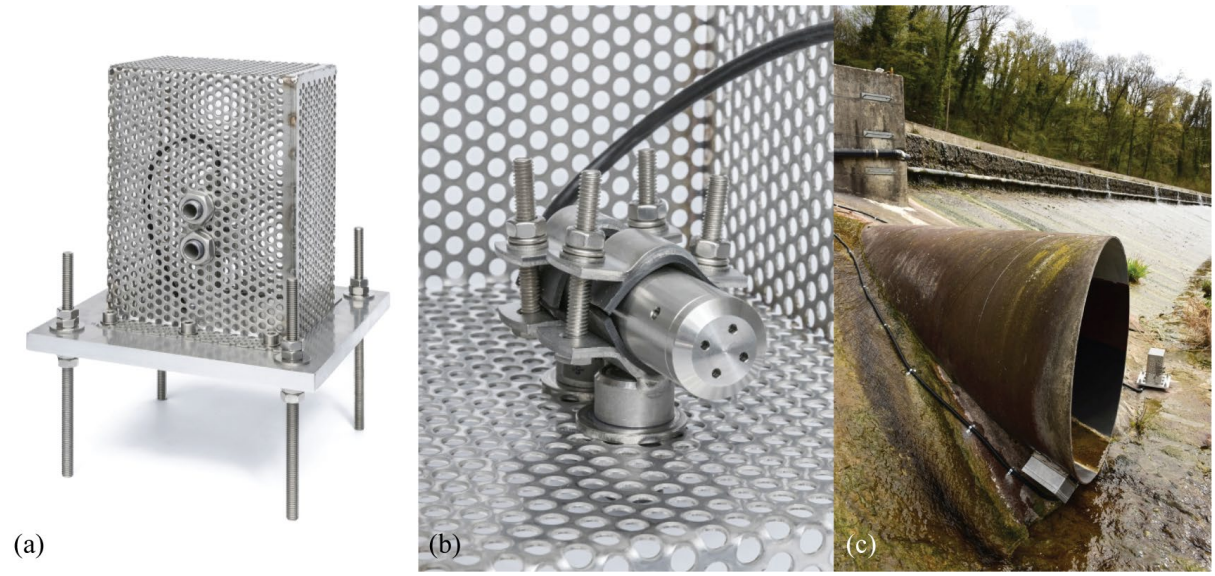

Figure 11: The setup for water level measurements with (a) the housing, (b) the sensor, and (c) the installation next to the vortex tube outlet.

3.1.2.3 Field calibration

On September 4, 2018, the vortex tube was calibrated in the field with four sediment mixtures of known grain size distributions that were flushed through the vortex tube. The grain size distribution analysis of these mixtures was conducted by square-hole sieving and with the grain-detection software BASEGRAIN (Detert and Weitbrecht, 2013). The images for BASEGRAIN were taken with a SONY ILCE-6000 and no distortion correction was applied. To obtain the real b-axis of the grains, a correction factor of $b_{sieve} / b = 0.80$ (Graham et al., 2010) and $b_{BASEGRAIN} / b = 0.85$ (Stähly et al., 2017) was applied.

The samples *fine*, *medium*, and *coarse* were obtained from an external gravel extraction site, whereas the sample *channel* is gravel directly excavated from the headwater channel (Figure 7). Table 3 and Figure 12 show the grain size distributions (GSD) and characteristic grain sizes of all sediment mixtures used in the field calibration.

Table 3: Characteristic grain sizes and the geometric standard deviation $\sigma_g = (D_{84}/D_{16})^{1/2}$ of the sediment mixtures used in the field calibration and in the turbine inlet (BG = BASEGRAIN, sieve = square-hole sieve).

sediment mixture	D_{16} **(mm)**	D_{50} **(mm)**	D_{84} **(mm)**	σ_g **(-)**
fine (sieve)	10.6	14.9	19.8	1.36
medium (sieve)	24.7	30.3	35.7	1.20
coarse (sieve)	41.2	52.1	60.9	1.22
channel (BG)	21.3	35.6	57.3	1.64
turbine inlet (BG)*	16.9	27.2	46.1	1.65

* not used in field calibration

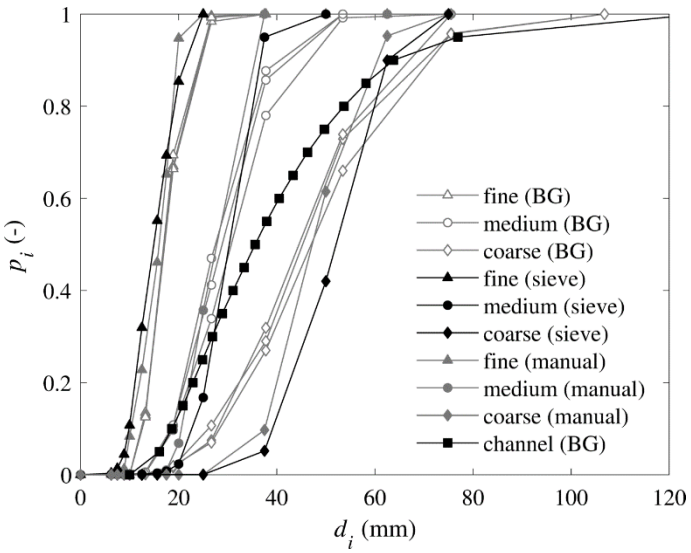

Figure 12: Grain size distribution of the four gravel mixtures used in the field calibration (fine, medium, coarse, channel). The legend indicates whether the grain size sample was processed by BASEGRAIN analysis (BG), by square-hole sieving (sieve), or by manual measurement of the b-axes (manual).

During the field calibration, the vortex tube was opened and closed six times (Table 4). The first opening CW served as calibration of the clear water signal and the flushing of any movable sediment in the vicinity of the vortex tube. During the subsequent calibration runs, the sediment mixtures were dumped in the upstream vicinity of the vortex tube by an excavator set up on a float (Figure 13). The material was dumped with the vortex tube closed and it was opened only afterwards. The river discharge Q was 72.5 m^3/s.

Table 4: Field calibration runs of September 4, 2018. The duration includes the opening and closing time of the vortex tube. The material was dumped in between the calibration runs, when the vortex tube was closed.

Notation	**Sediment mixture**	**Volume (m^3)**	**Start time (UTC)**	**End time (UTC)**	**Duration (s)**
CW	-	-	2018/09/04 08:06:53	2018/09/04 08:18:57	725
CF1	fine	0.5	2018/09/04 08:22:52	2018/09/04 08:34:56	725
CF2	fine	0.5	2018/09/04 08:36:53	2018/09/04 08:48:57	725
CM	medium	1	2018/09/04 08:50:53	2018/09/04 09:08:57	1085
CC	coarse	1	2018/09/04 09:10:53	2018/09/04 09:24:57	845
CCH	channel	approx. 2	2018/09/04 09:28:53	2018/09/04 09:43:57	905

The field calibration is based on the assumption that all of the dumped material was transported through the vortex tube. It is questionable if this assumption holds, as part of the sample may have been entrained by the flow to pass the vortex tube and be transported further along the headwater channel or it may have been deposited and not entrained by the increased flow velocity following the opening of the vortex tube. The relative importance of these processes can be assessed by considering the hydrological conditions. The bed shear stresses during the calibration runs (Q = 72.5 m^3/s) are too small to entrain grains larger than 4-8 mm, as was deduced from ADCP measurements in March 2018 with Q = 62-71 m^3/s (Section 3.3.3.1). Compared to the GSD of the sample mixtures shown in Figure 13, it is therefore unlikely that a large fraction of the sample was by-passing the vortex tube. Moreover, laboratory tests have shown that the opening of the vortex tube strongly influences the local flow field and establishes a suction effect that is especially strong when the water level difference between the headwater channel and the residual flow reach is large (VAW, 2017; Rachelly et al., 2019). As a result of the low discharge and therefore large water level difference on the day of the calibration, the relative flow field change caused by the vortex tube was strong and likely entrained most of the dumped gravel. Nevertheless, there is no way of knowing exactly what fraction of the total bedload volume was passing through the vortex tube and has thus induced impact signals. This uncertainty would have been reduced if the number of calibration runs and the variation in sample volume had been increased or if it had been possible to conduct systematic flume experiments, as it is generally recommended for indirect bedload monitoring systems (Gray et al., 2010; Wyss et al., 2016b; Wyss et al., 2016c). Also, a bedload sampling system downstream of the vortex tube outlet would have been necessary to improve the calibration (compare Rickenmann et al., 2012). The simple and relatively inexpensive calibration approach applied here was adjusted to the study purpose.

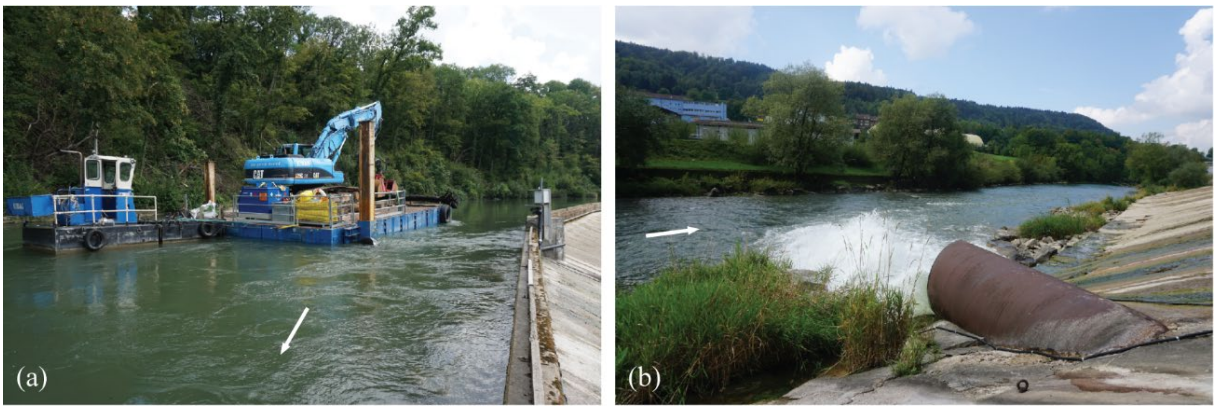

Figure 13: Field calibration on September 4, 2018 with (a) an excavator set up on a float and (b) the outlet of the vortex tube during a calibration run.

3.1.2.4 Drop tests

To gain more detailed knowledge about the relationship between grain characteristics such as grain diameter and the recorded signal, drop tests were performed. 19 grains of varying diameter, weight, and shape were dropped from varying heights onto four different locations inside the vortex tube (Figure 14). These tests were performed when the gate was closed, i.e. no water was flowing through the vortex tube. This means that the drop test conditions were very different from the conditions during actual vortex tube operation. Nevertheless, drop tests can help to isolate the effect of certain grain characteristics on the impact signal and they complement the dataset obtained during the field calibration tests.

The drop test signals often contained several distinguishable impacts, representing a rolling / hopping motion of the grain towards the tube bottom (e.g. from location A). As this is likely not a realistic representation of the grain motion in the very turbulent conditions during vortex tube operation, only the first impact was further analyzed.

Figure 14: Drop tests were conducted with (a) 19 grains of different diameters D_i, weight G_i, and shape factor C_i, which were (b) dropped at four different locations A-D, from drop heights of 0.1-0.7 m at locations A and D, and 0.1-1.1 m at locations B and C.

3.1.3 Results

3.1.3.1 Signal denoising

The clear water calibration sample (CW) was used to determine signal noise created by clear water flowing through the vortex tube and gate operation. A discrete wavelet transform (DWT) with the sym4 wavelet and 9 decomposition levels was applied to the CW sample. The maximum values of all resulting detail coefficients D1-D9 were defined as noise levels. The decomposed signals of the other calibration samples (CF1-CCH) are filtered by applying hard thresholding with these noise levels. Afterwards, the denoised signals are reconstructed with the inverse DWT. The remaining background noise level was determined to be A_{min} = 0.007 V for the geophone.

3.1.3.2 Amplitude classes

The impact of grain size has been shown to have an influence on the maximum amplitude and the frequency of the recorded impact signal. In general, the larger the grain the higher the amplitude and the lower the frequency of the impact signal (Barrière et al., 2015). This relation could be used to extract information on the grain size distribution from the signal of a passive acoustic bedload monitoring system. To do this, the signal is stratified into amplitude classes (AC) (Wyss et al., 2014; Wyss et al., 2016a). To define appropriate AC, the maximum amplitude per calibration event A_{maxmax} (V) was related to the maximum grain size diameter D_{max} (mm). D_{max} was determined from the square-hole sieve analysis and largest detected particle in the BASEGRAIN analysis (Figure 12).

Following Wyss *et al.* (2016a), a power law function of D_{max} is fitted to the 'Schiffmühle field cal' data points (Figure 15)

$$A_{\max\max} = 2.82 \cdot 10^{-4} \cdot D_{\max}^{1.81} \quad (1)$$

where Eq. (1) represents the geophone data with an RMSE = 0.11 V, which corresponds to the 95% quantile at ± 0.22 V. According to this equation, the smallest detectable grain is 6 mm for a noise threshold of A_{min} = 0.007 V. The drop tests are not included in the fit because they were recorded in different conditions, i.e. no water flow and vertical impingement. Nevertheless, the drop test data points

support the validity of Eq. 1 (Figure 15). In addition, the comparison to datasets of two studies (Wyss et al., 2016a; Müller-Hagmann, 2017) with Swiss Plate Geophone Systems (SPGS) also shows a good agreement (Figure 15).

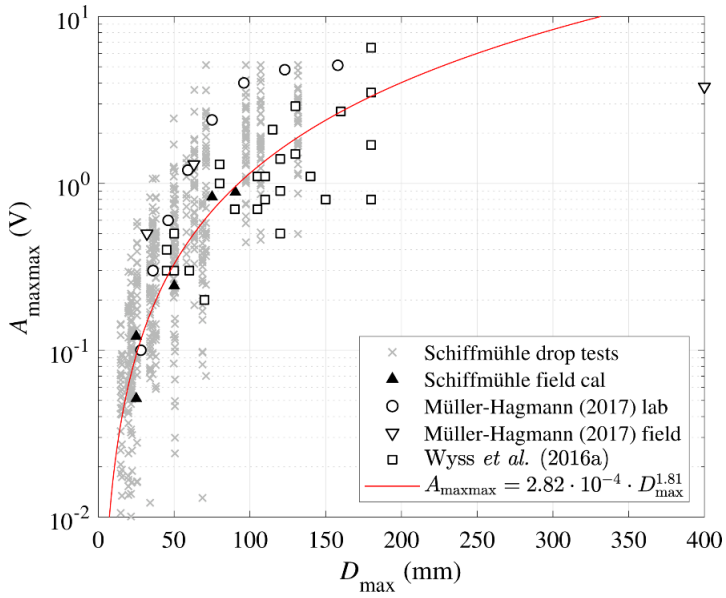

Figure 15: The maximum amplitude A_{maxmax} as a power law function of the maximum transported grain size D_{max} for all field calibration runs. Only the'Schiffmühle field cal' data points were used to fit the power law, the drop test and literature data is only displayed for comparison.

Based on Eq. (1), the grain size classes that were used in the calibration events (Figure 12) can be connected to corresponding amplitude classes (AC) (Table 5). The lower grain diameter D_{low} thereby represents the retaining sieve of the corresponding grain size class. This signal analysis based on amplitude classes can enable a more precise determination of the transported bedload volume as well as the extraction of information on the transported grain sizes (e.g. Wyss et al., 2016a; Mueller-Hagmann, 2017)

Table 5: Amplitude class (AC) definition for the geophone signal with the corresponding lower grain diameter D_{low}, upper grain diameter D_{up}, geometric mean grain diameter $D_{g,m}$, mean grain weight G_m, lower amplitude threshold th_{low}, upper amplitude threshold th_{up}, and mean amplitude th_m. The smallest grain size class (6.25-7.5 mm) corresponds to amplitude thresholds below the noise level (A_{min} = 0.007 V) and is therefore not defined as an amplitude class.

AC	D_{low} (mm)	D_{up} (mm)	$D_{g,m}$ (mm)	G_m (g)	th_{low} (V)	th_{up} (V)	th_m (V)
	6.25	7.5	6.8	0.73	0.0055	0.0076	0.0066
1	7.5	8.875	8.2	1.16	0.0076	0.0104	0.0090
2	8.875	10	9.4	1.69	0.0104	0.0128	0.0116
3	10	12.5	1.2	2.66	0.0128	0.0192	0.0160
4	12.5	15.625	14.0	4.78	0.0192	0.0288	0.0240
5	15.625	17.5	16.5	7.44	0.0288	0.0354	0.0321
6	17.5	20	18.7	10.29	0.0354	0.0451	0.0402
7	20	25	22.4	16.44	0.0451	0.0675	0.0563
8	25	37.5	30.6	37.57	0.0675	0.1406	0.1040
9	37.5	50	43.3	93.45	0.1406	0.2366	0.1886
10	50	62.5	55.9	182.89	0.2366	0.3543	0.2955
11	62.5	75	68.5	311.64	0.3543	0.4928	0.4236

3.1.3.3 Signal characteristics

Eight signal characteristics are computed for each calibration event and all monitoring data (Table 6). This extensive data preprocessing allows a detailed and diverse further data analysis (e.g. determination of grain size distribution). Figure 16 shows an example signal and the implementation of impulse and packet count.

Table 6: Computed signal characteristics per second and per single packet. All values are computed separately for each amplitude class.

s_Imp	(s^{-1})	Impulse count per second
s_Pac	(s^{-1})	Packet count per second
s_Amax	(V)	Maximum amplitude per second
s_Pdur	(s)	Total packet duration per second
p_Imp	(-)	Impulse count of single packet
p_Amax	(V)	Maximum amplitude of single packet
p_Pdur	(s)	Duration of single packet
p_Fcentr	(Hz)	Centroid frequency of single packet

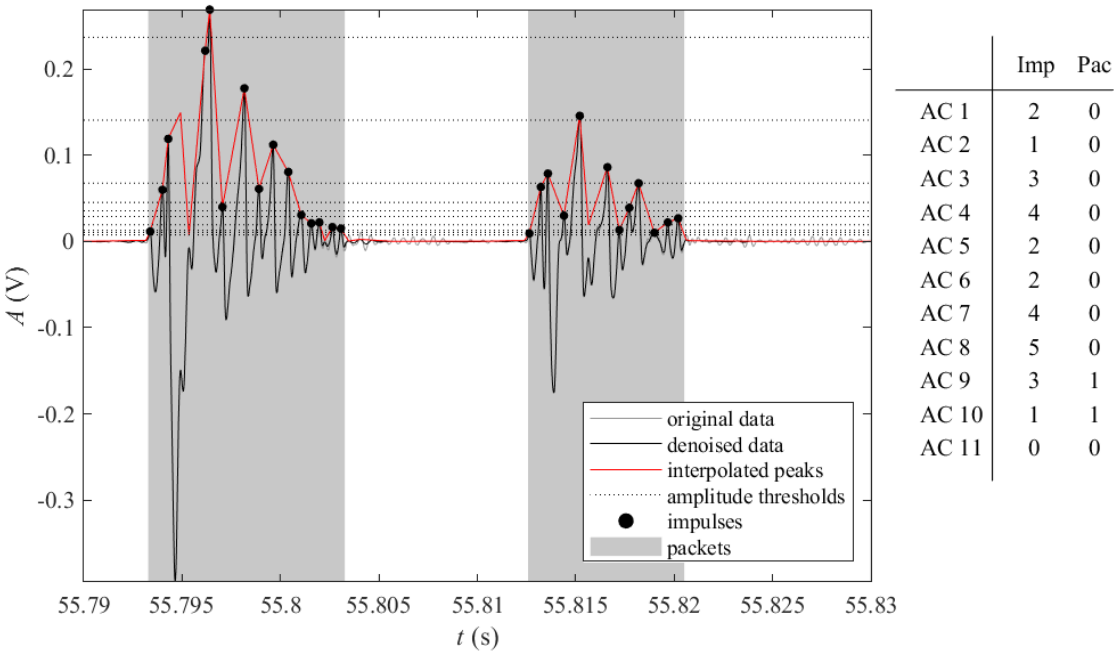

Figure 16: Example for an amplitude signal and the definition of the impulse (Imp) and packet count (Pac). The original signal was first filtered to remove clear water and gate operation noise. The impulses were then identified as the single signal peaks of this filtered signal and sorted into the corresponding amplitude class (AC). The packets were defined by interpolating between these peaks and identifying the sections where this interpolated signal surpasses the noise threshold (lowest AC). Each packet was then assigned to the AC corresponding to the highest peak within this packet.

Figure 17 shows the time series of impulse and packet counts per second and their total number for all field calibration events. Note that all plots have equal ordinates to emphasize the significant difference between finer and coarser samples. The CW sample recorded no impulses, which confirms the applied noise filter procedure (see section 3.1.3.1). The CF1 and CF2 samples show only a few impulses, indicating that their grain sizes (D_{84} = 19.8 mm) mostly lie below the detection limit, i.e. the detection limit would correspond to a grain size of approximately 20 mm. In contrast, the CM, CC, and CCH samples recorded significantly higher numbers of impulses and packets. The total number of impulses

scales with the coarseness of the grain sizes used (cf. Figure 12), i.e. the highest number of impulses was recorded for the CC sample (Figure 17e).

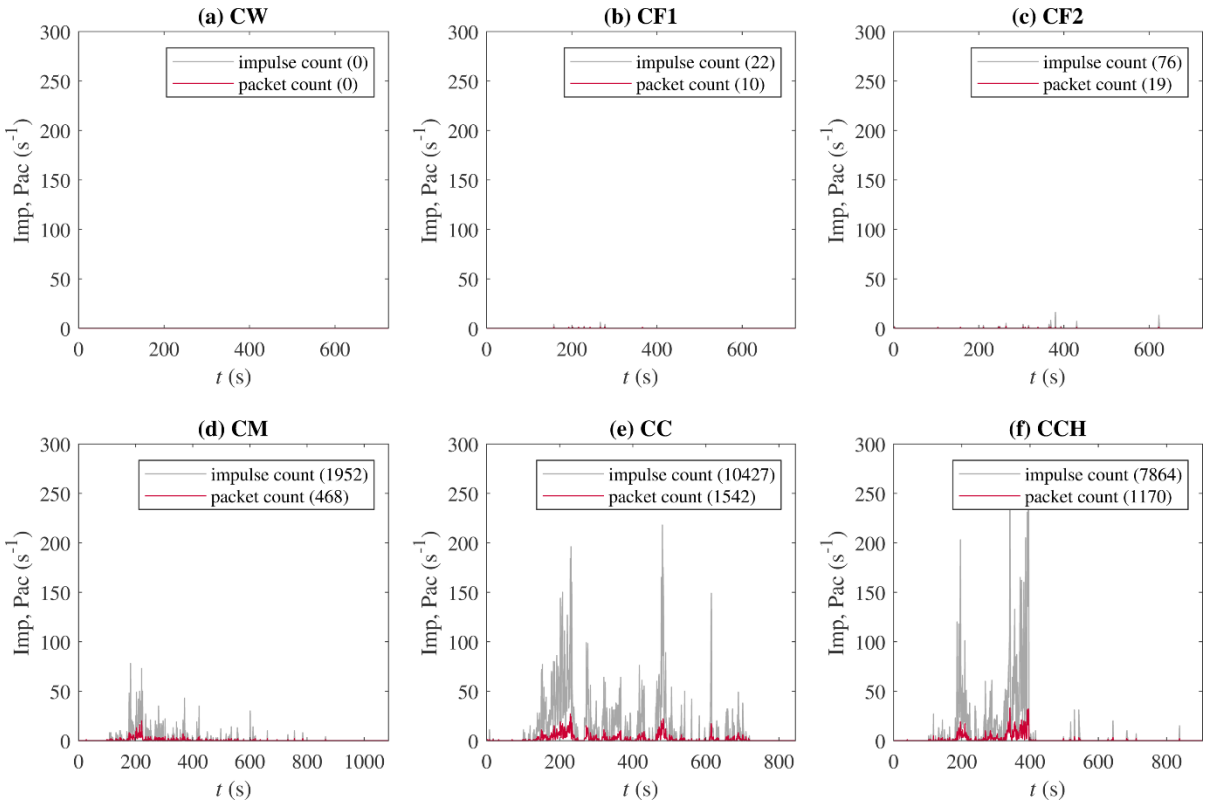

Figure 17: Time series of impulse and packet count for the (a) CW, (b) CF1, (c) CF2, (d) CM, (e) CC, (f) CCH calibration sample. The total number of impulses and packets recorded during each calibration sample are noted in brackets.

When too many grains are transported across the impact plate at the same time, their signals partly overlap and it may become difficult to distinguish single grains. The signal overlap z_p after Wyss et al. (2016a) with

$$z_p = \frac{\sum \Delta t_{p,i}}{T} \tag{2}$$

where $\Delta t_{p,i}$ = sum of packet duration (s) within total time T (s) should therefore not exceed 0.1. Figure 18 shows histograms of signal overlap z_p determined per second for all calibration events. Only seconds with at least one packet count were included in this analysis. The signal overlap does not seem to reach problematic levels, with the highest percentage of $z_p > 0.1$ being 2.1% during the CCH sample (Figure 18f).

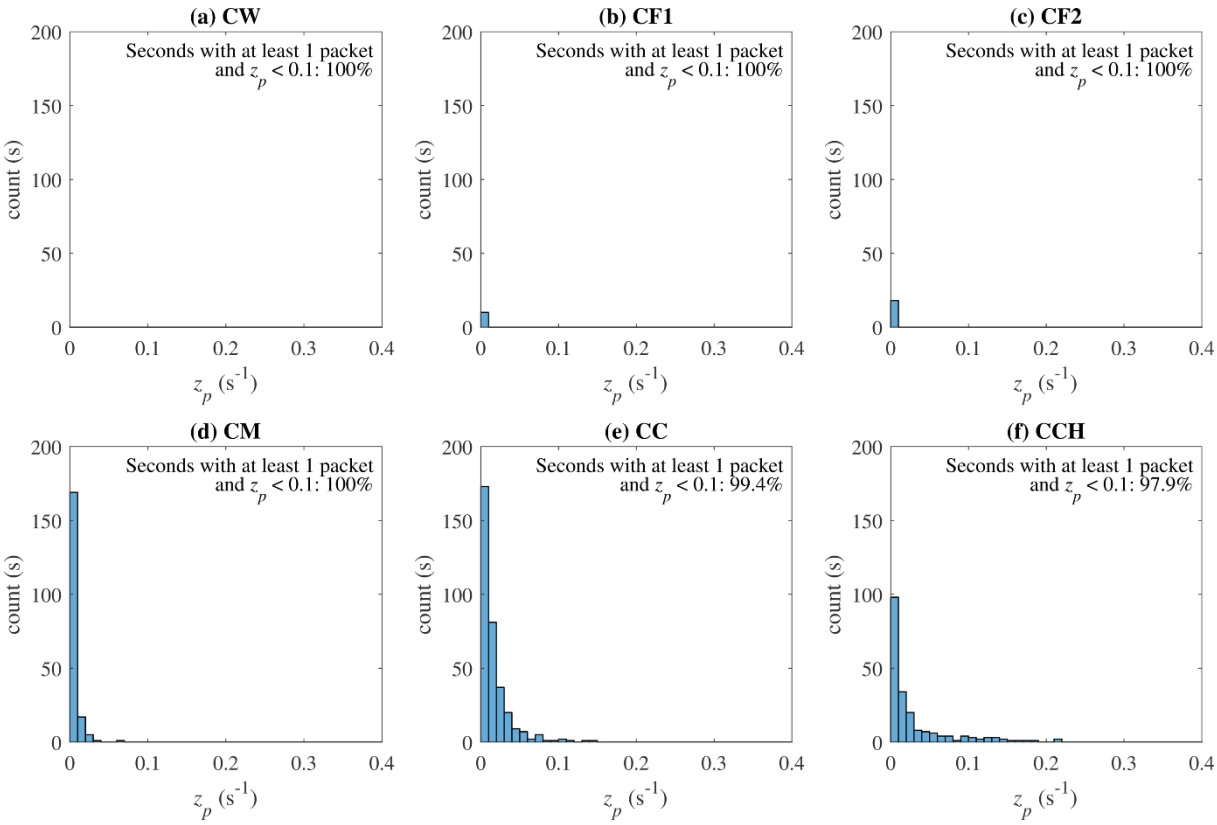

Figure 18: Histograms of signal overlap z_p per second for all seconds with at least one packet recorded for the (a) CW, (b) CF1, (c) CF2, (d) CM, (e) CC, and (f) CCH calibration sample. The lowest ratio of unproblematic signal overlap ($z_p < 0.1$) is obtained for the CCH sample.

3.1.3.4 Calibration analysis

Assuming that one packet corresponds to one grain and applying the signal stratification by amplitude class, the impulse count per grain can be determined as a function of grain size (Figure 19a). The larger the grain diameter the higher the number of impulses per grain, following a roughly linear trend.

Based on the known mass of the calibration samples (Table 4), a calibration coefficient k_b (Imp/kg) can be defined as number of impulses Imp divided by the mass of the transported sample. By applying the grain size distributions of the calibration samples (Figure 12) to the total mass of the sample, the partial mass in each amplitude class can be determined and thus, AC-specific calibration coefficients k_b are defined (Figure 19b).

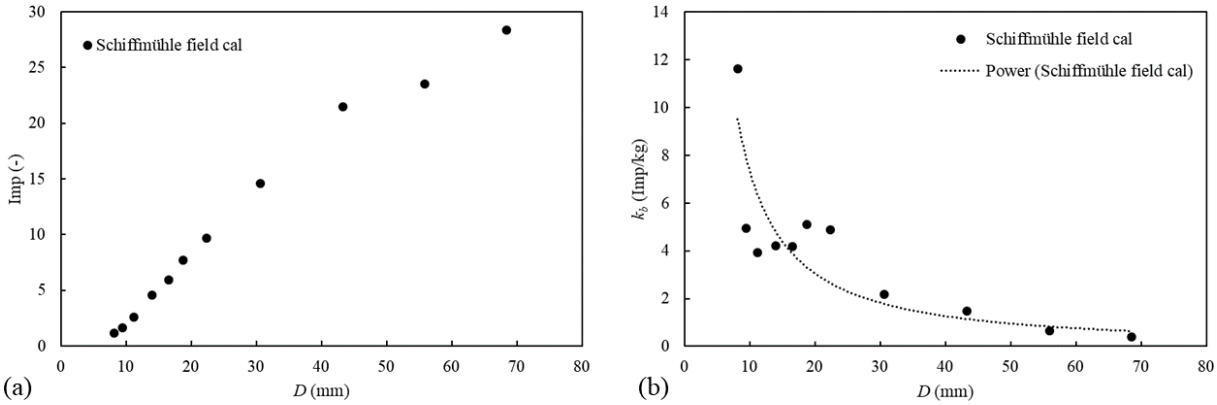

Figure 19: (a) Impulse count per grain (i.e. packet) related to grain size D and (b) AC-specific calibration coefficients k_b as a function of grain size D with the power law fit $k_b = 135.5 * D^{-1.27}$. Both plots show the aggregated data of the calibration events CF1, CF2, CM, CC, and CCH per amplitude class.

Based on the calibration coefficients per amplitude class, the total transported volume of a sample can be determined in two ways:

- The total impulse count of a sample is divided by a lumped k_b value that is defined as the weighted average of all AC-specific k_b values. The lumped k_b value for the field calibration samples is 2.2 Imp/kg.
- The impulse count of the unknown sample is divided into amplitude classes and each partial impulse count is divided by the corresponding AC-specific k_b (Figure 19b). The resulting AC-specific mass values are summed up to the total sample mass.

Table 7 compares the estimated mass for both calculation methods to the measured mass for all calibration samples. The lumped k_b method performs rather poorly, strongly overestimating the mass for the coarser samples. The weighted average seems to be too high to correctly represent the low AC-specific k_b values of coarse grain classes (Figure 19b). In contrast, the AC-specific k_b method produces more accurate results. It performs especially well for the CCH sample (11% deviation), which corresponds to the grain size distribution found in the channel.

Both methods strongly underestimate the mass for the fine samples CF1 and CF2. This may be due to fuzziness in the determination of the smallest detectable grain or because fine grains are transported through the vortex tube without much interaction with it. The true cause for this deviation cannot be determined, as we were not able to measure the sediment output of the vortex tube during field calibration and thus it is unclear whether the measured mass truly corresponds to the mass that was transported through the vortex tube. Generally speaking, the transported bedload mass or volume for small flood events with low bedload transport activity will most likely be significantly underestimated. Nevertheless, the good performance of the AC-specific k_b method for the channel sample CCH suggests that for larger flood events with substantial bedload transport activity (with coarser grains), the mass / volume estimation might be more reliable.

Table 7: Comparison of estimated and measured sample mass for both calculation methods, the lumped k_b value and the AC-specific k_b values for the five calibration samples CF1-CCH.

		Lumped k_b		**AC-specific k_b**	
	Measured mass (kg)	**Estimated mass (kg)**	**Error (%)**	**Estimated mass (kg)**	**Error (%)**
CF1	780	48	-94	4	-99
CF2	780	167	-79	25	-97
CM	1560	4297	175	588	-62
CC	1560	22954	1371	3686	136
CCH	3120	17312	455	3474	11

3.1.3.5 Grain sizes transported during flood events

A simple analysis of the transported grain sizes during flood events can be made based on the relation between maximum amplitude and maximum diameter (Figure 15). Figure 20 shows two flood events of different magnitude and duration. During the 14-Jan-19 event, much smaller grain diameters of up to 50 mm were recorded compared to the larger grain diameters of up to 130 mm during the 20-May-19 event. The 20-May-19 event shows a correlation between discharge magnitude and maximum transported grain diameter (Figure 20b). Furthermore, the comparison of the flood events shown in Figure 20 implicates that during both events, similar discharge magnitudes result in similar maximum grain sizes transported through the vortex tube.

The amplitude histogram analysis will result in even more detailed information, not only on the maximum transported grain size, but the grain size distribution of the transported material and the transported bedload volume or mass (see section 3.1.3.4). Due to the long processing time of the monitoring data, this analysis is pending. Furthermore, the calculation of bed shear stresses for different flood discharge from the 3D hydro-numerical model (see section 3.3.3.3) will allow the determination of maximum transported grain sizes in the headwater channel. This will provide an opportunity to validate the grain size diameters recorded in the vortex tube.

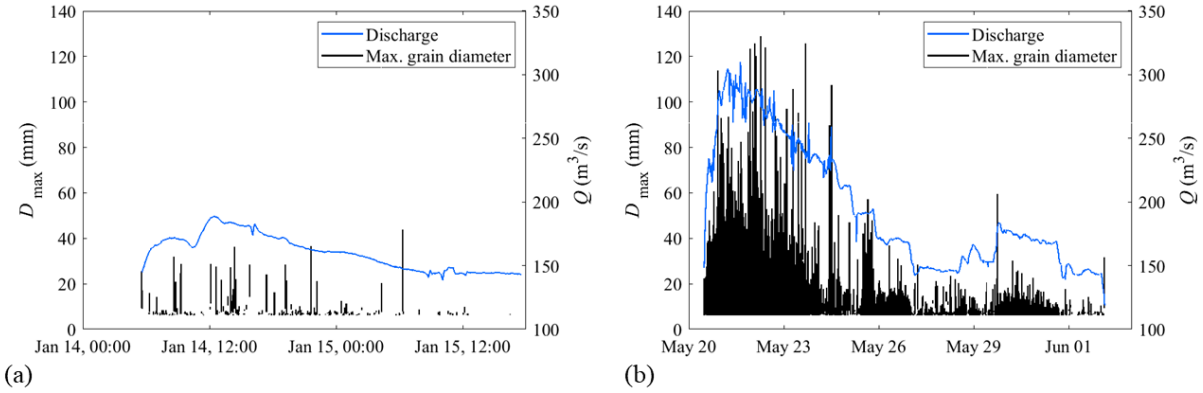

Figure 20: Time series of flood discharge and maximum transported grain diameter for the flood events (a) 14-Jan-19 and (b) 20-May-19. Only amplitudes above the noise level A_{min} = 0.007 V were converted to grain diameters.

3.1.4 Conclusions and Outlook

A bedload monitoring system with a geophone, an accelerometer, and a microphone has been installed on a vortex tube, a bedload diversion system at HPP Schiffmühle. It was calibrated in the field by repeatedly dumping sediment samples of known grain size distribution and volume upstream of the vortex tube and subsequently flushing them to the residual flow reach. In addition, drop tests with grains of varying diameter and shape were performed during non-operational conditions. The analysis of the calibration data showed that transported grain sizes can indeed be differentiated. Larger grains not only cause signals with higher maximum amplitudes than smaller grains, they also produce more impulses per grain. In contrast, the determination of the transported volume is more difficult, largely due to the limited calibration data. Because the real value of bedload transported through the vortex tube is unknown, the relation between impulse count and volume remains uncertain. The calibration relation is more reliable for events with transport of coarser grains compared to events with transport of primarily fine grains. More insight into the absolute values of transported bedload volume is expected from the comparison of the vortex tube monitoring data with repeated ADCP measurements in the headwater channel (see section 3.3.3.1) and with bed shear stresses extracted from the 3D hydro-numerical model (see section 3.3.3.3).

Overall, it can be concluded that the usage of the steel vortex tube as conveyance body and impact plate for passive acoustic bedload monitoring is possible. Furthermore, the monitoring data can provide information on transported bedload volume and grain size diameters. For future studies with similar systems, we recommend an improvement and expansion of the calibration procedure. It would be especially valuable to measure the actual bedload volume transported through the vortex tube during field calibration events.

A comprehensive analysis of all collected monitoring data along with the calibration data will be published in a peer-reviewed journal article during the next few months. This article will then also be made publicly available on the FIThydro Wiki.

3.2 Downstream impact of sediment management at HPPs (NTNU, ETHZ)

The dynamic changes in bedload transport rates and total transported masses were quantified and their effects on river ecology and morphology were qualitatively and numerically evaluated.

3.2.1 Data

The Data for the evaluations were collected in four different field campaigns in the residual flow reach. The sampling spots were chosen in a way which should cover as good as possible presumably different sediment and habitat conditions (Figure 21). As this depends to a high extend on the flow velocities / shear stresses and on stabilizing effects of the vegetation, the spots were chosen whenever possible to represent areas of

- high flow velocities / permanent wetted areas (Figure 21, yellow)
- high flow velocities / not permanent wetted areas (Figure 21, yellow)
- regions affected by the vortex tube (Figure 21, blue)
- low flow velocities / permanent wetted areas (Figure 21, green)
- low flow velocities / not permanent wetted areas (Figure 21, yellow and green)

The differentiation between areas of assumingly permanent submergence and changes between submerged and not submerged was made based on comparison of the water level during the measurements and satellite pictures as well as information given by the HPP operator. This is visible in Figure 21 already, as the picture shows a state with higher discharge then experienced during the measurements (red marked area in Figure 21).

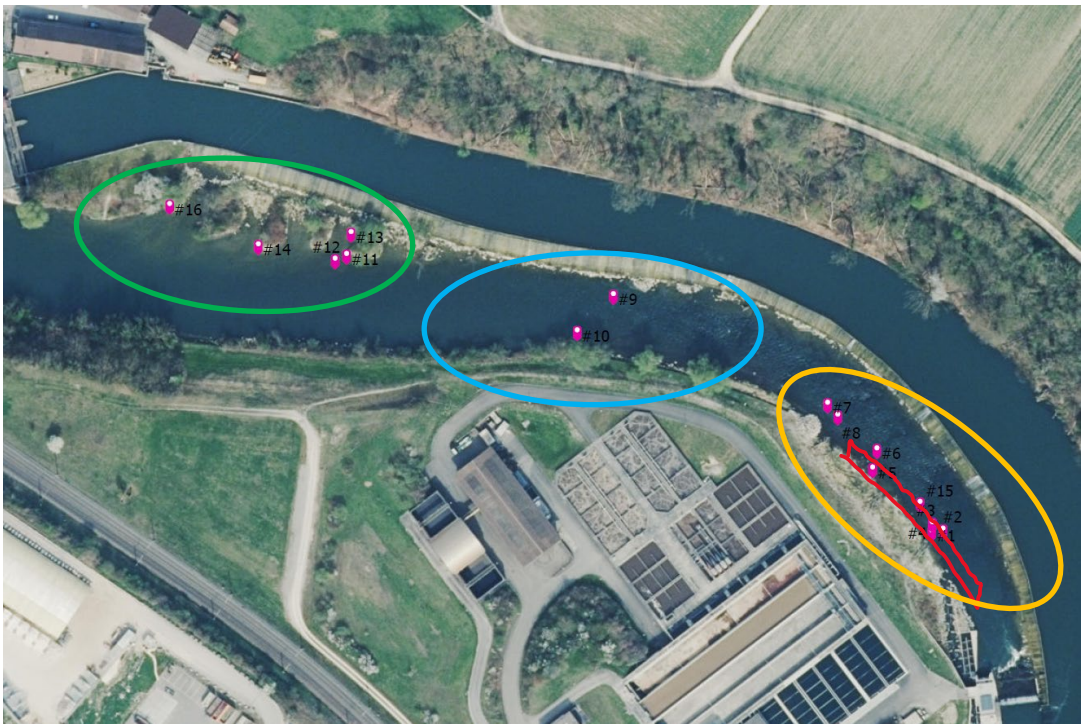

Figure 21: Positioning of the sampling sites at the residual flow reach in Schiffmühle in March 2018; the red area indicates the zone with changes between submerged and unsubmerged depending of the discharge. During the measurements in March 2018 this area was not submerged; the orange color along the weir indicates the approximate length of the sediment deposition

In summer 2018 sediment was dumped in the residual flow reach of the river with a height of up to 3m throughout the whole stretch (Figure 22).

Figure 22: Deposition of sediment in the residual flow reach in October 2018.

Until end of 2019 most of the sediment was eroded. Some was spread within the reach, especially forming a small island in the upper part of the reach (red circle in Figure 23) and a broader bank along the weir (green circle in Figure 23).

This spreading of the sediment throughout the reach had different effects. To be able to keep the differentiation between areas with high and low flow velocities, as described above, some of the sampling locations had to be moved accordingly in terms of geographic coordinates. Further effects can be seen in the results themselves as described later. A specific challenge on the evaluation of the data is given by the fact that it is unfortunately not defined which composition the deposited sediment had.

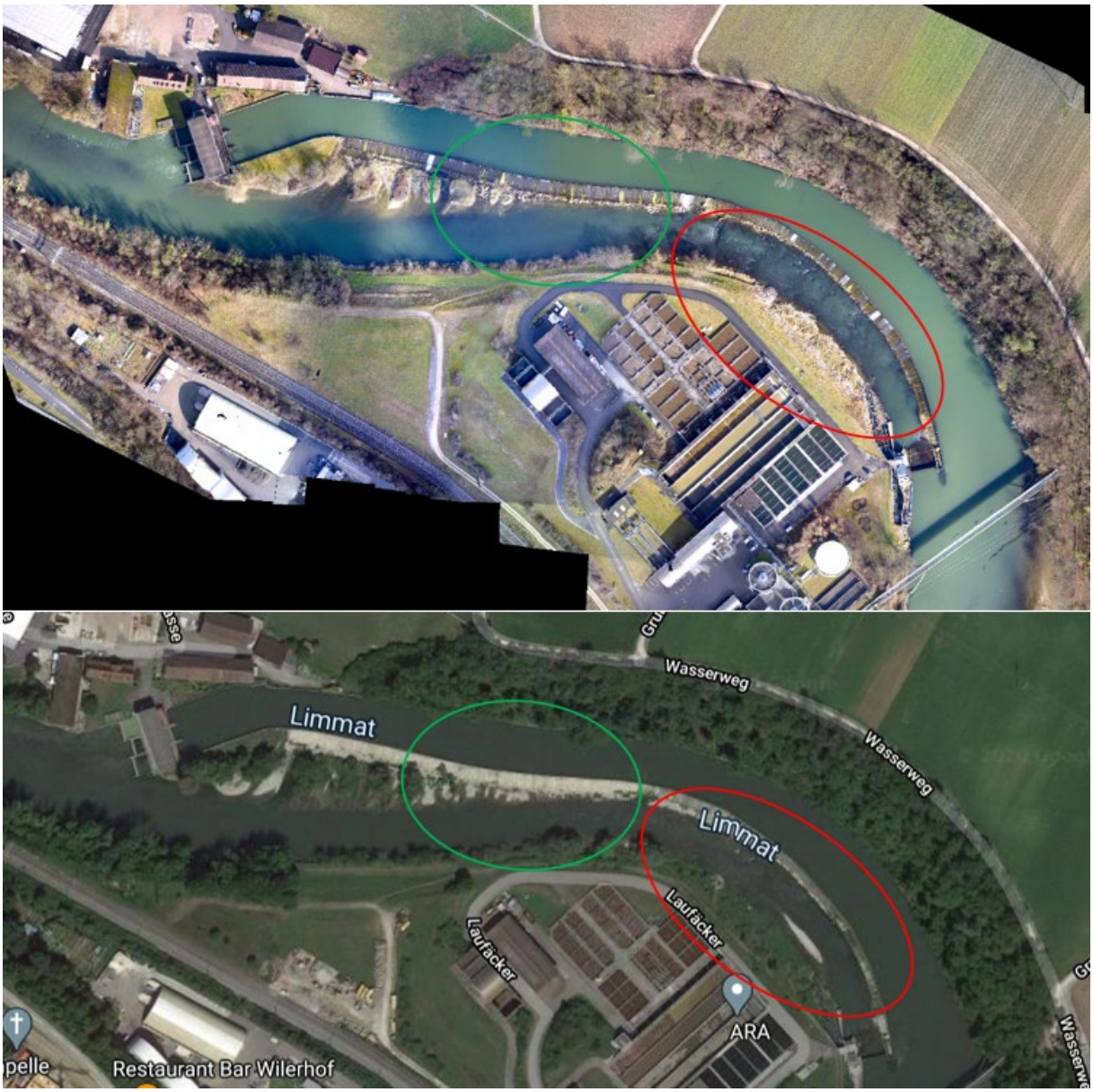

Figure 23: Bed changes as a result of the sediment deposition along the weir from March 2018 (before deposition, picture Martin Detert) until beginning of 2020 (picture google maps).

Habitat quality for fish depends to a high extend on the availability and the distribution of a specific sediment mixture in a river bed (Magee et al., 1996; Lake & Hinch, 1999; Fierz, 2009; Kemp et al., 2011; Schultz et al., 2012; Hauer et al., 2013; Michel et al., 2013). Under natural or nature like conditions this sediment provides a shelter for fish in the early stages of the lifecycle (Bellamy et al., 1992; Finstad et al., 2007; Teichert et al., 2010; Forseth et al., 2014) (Figure 24). Further it influences on a physical basis the current in a river and generates turbulent patterns on different size scales. On a larger scale allows this the differentiation between resting and swimming zones, regions for energy efficient swimming etc (Teichert et al., 2010; Wilkes et al., 2013).

An insufficient sediment quality availability on the other hand can lead to a serious degradation in the number of fish species present as well as the missing of certain life stages of fish and hence a degradation of the population (Osmundsen et al., 2002; Kemp et al., 2011; Kjelland et al., 2015). For a stable and self-sufficient fish population the sediment quality availability needs to be kept on a certain minimum

level. In case this level cannot be reached, mitigation measures need to be taken. Such mitigation measures are described in the FIThydro deliverables 2.1, 2.2, and 4.1.

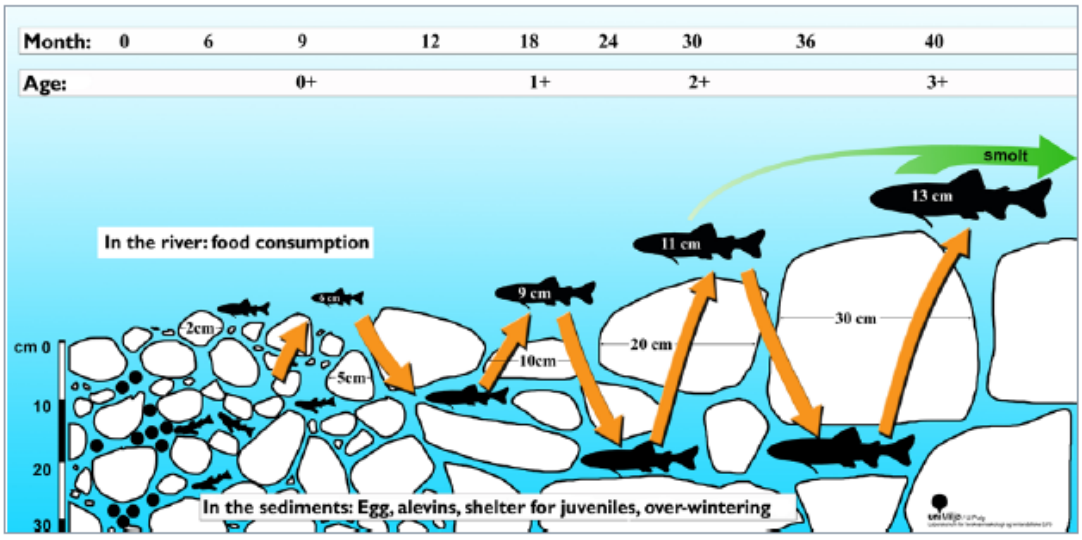

Figure 24: Hiding places in the sediment throughout different life stages salmon (Forseth et al, 2014)

Not only the specific needs of fish must be known to be able to give a detailed description of the sediment related habitat quality, but also detailed information of the sediment mixture present. Therefor certain sediment mixture parameter mainly related to the grain size and the distribution of the different fractions within and throughout the river reach of interest need to be evaluated.

Further information needs to be collected on the shelter availability using the Finstad method. A detailed description of this method can be found at the end of this subchapter. For both methods, the investigation of the grain size distribution as well as for the Finstad method, data from the test site is needed to be analyzed further in the laboratory.

3.2.2 Methodology

Grain Size distribution

The grain size distribution can be evaluated based on different sampling methods (Bunte & Abt, 2001). For this case the volumetric method was chosen based on previous work linking the particle distribution of D5 and D10 (Jocham, 2010; Szabo-Meszaros, 2015), which means that a specific layer of interest on the surface (the armor layer) was excavated (Figure 25) following the method described by Bunte & Abt (2001). The sediment sample will then be sieved in order to get the grain size distribution, which allows a more detailed characterisation of the sediment mixture.

In addition to the volumetric method, pebble count is used and a picture-based size evaluation with the software Basegrain (Detert & Weitbrecht, 2013; Rüther et al., 2013).

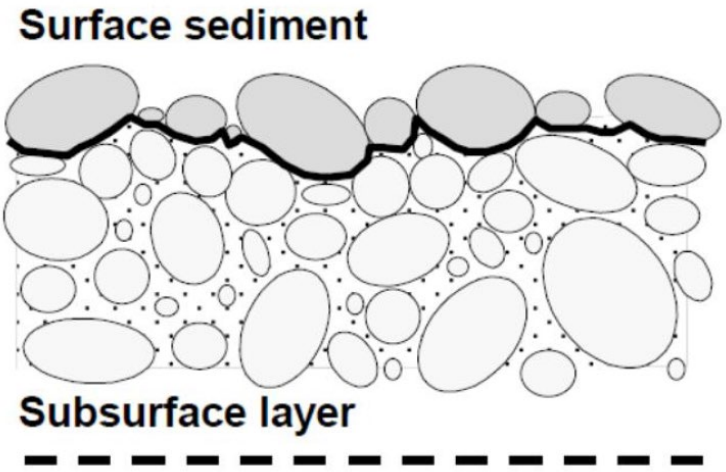

Figure 25: Stratigraphy of a river bed distinguishing between surface layer and subsurface layer (Bizzi et al., 2014).

The samples were dried in the laboratory and sieved. The percentiles used to investigate a correlation with the shelter availability in the river reach can be calculated following Bunte & Abt (2001):

$$D_x = 10^{[log(x_2)-log(x_1)]*\frac{y_x-y_1}{y_2-y_1}+x_1}$$

With

D_x the percentile at a percentage of x [mm]

y_1 – the value of the cumulative percent frequency just below the targeted cumulative frequency

y_2 – the value of the cumulative percent frequency just above the targeted cumulative frequency

y_x – the value of the cumulative percent frequency at the targeted cumulative frequency

x_1, x_2 the particle sizes associated with the cumulative

frequencies y_1 and y_2 and at the chosen position x.

Another option is a graphical evaluation based on the given data. Further specific percentiles where chosen for further investigations.

Shelter availability

The measurement of the shelter availability is based on the findings of Finstad et al. (2007). The method is based on the idea to detect and measure openings which can be used as shelter for fish. Based on the determined size and depth of the opening different quality classes are defined and the results can be summarized to give information about the functionality as a habitat based on shelter availability.

Following Forseth et al. (2014) this measurement is conducted by using a plastic tube with the diameter of 13mm, as this size was correlated to the highest extend with juvenile fish of different life stages (Finstad et al., 2007). In addition, tubes with a diameter of 8mm and 5mm were used, to possibly allow

to extend this method to other, smaller fish species as well. Each tube had marks at a depth basis of 3cm, 7cm and 12cm indicating the depth categories 1, 2 and 3. The shelter abundance is measured within a specific area which is given by a metal frame of 60cm x 60cm size. This frame is placed on the river bed (see Figure 26) and the openings are measured within the covered area.

Figure 26: The PVC tube with markers and metal frame.

With the results for the three categories a so-called weighted shelter is calculated (Forseth et al., 2014):

$$S = S_1 + S_2 * 2 + S_3 * 3$$

With:

S	Weighted shelter availability
S_1	Number of measured shelter in category 1
S_2	Number of measured shelter in category 2
S_3	Number of measured shelter in category 3

The values for the weighted shelter abundance can be assigned to different classes (Forseth et al., 2014), indicating the quality of the respective section as a habitat based on shelter (Table 8).

Table 8: Color-coded shelter abundance based on Forseth et al. (2014).

$S < 5$	$5 \leq S \leq 10$	$S > 10$
Low shelter	Moderate shelter	High shelter

Methodology of linking grain size distributions and shelter availability

The methodology to link grain size distributions and the shelter availability was first developed and tested for Norwegian rivers and salmon (Jocham, 2010; Szabo-Meszaros, 2015). As the shelter availability is defined as an open space between sediment grains and the spaces between the grains are influenced by the sediment distribution (Beschta et al., 1979; Schälchli, 1992) it can be assumed that the physical parameters as described by the percentiles can be linked with the shelter availability in certain areas. It could be shown that for Norwegian rivers a clear correlation between D5 / D10 and the shelter availability exists. In this study this applies as well to the weighted as to the unweighted values for shelter abundance. Both show a clear linear correlation for both D5 and D10 (Figure 27).

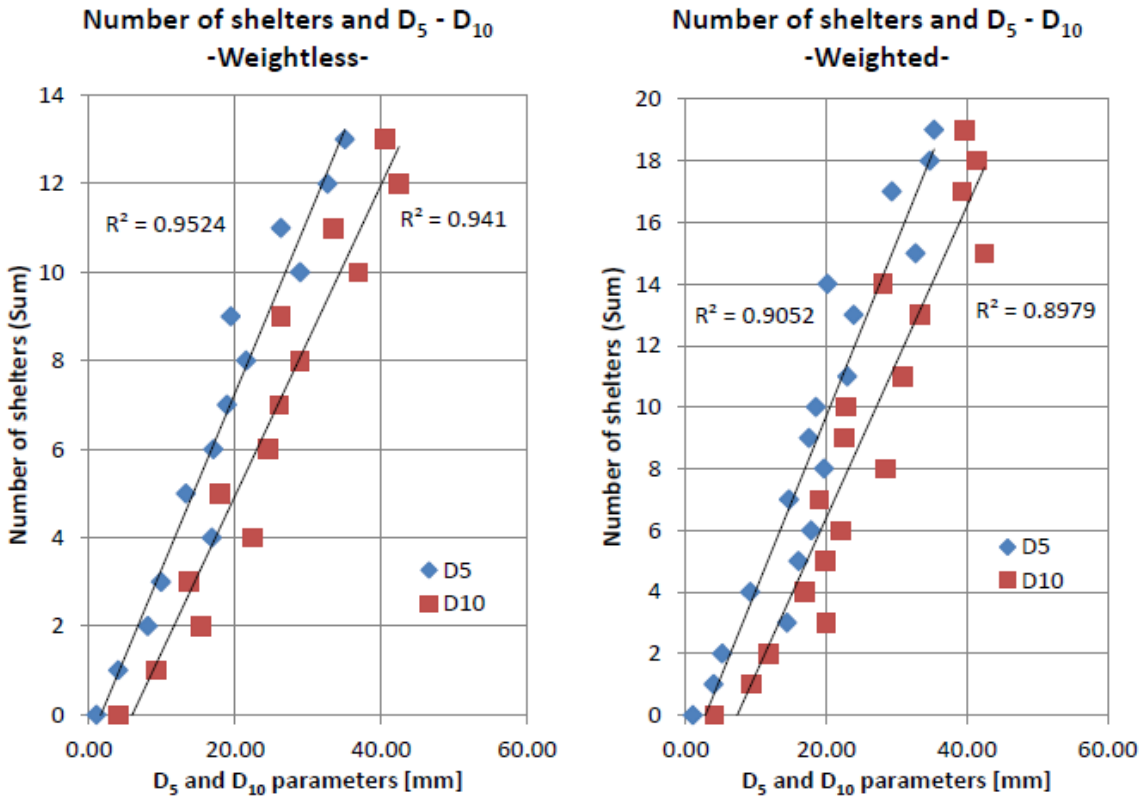

Figure 27: Correlation of the extended database between D5 and D10 averaged parameters and number of weightless (left) and weighted (right) shelters with the R2 coefficients (Szabo-Meszaros, 2015).

3.2.3 Results

Habitat mapping, sediment sampling, shelter measurements and substrate characterization

For habitat mapping and sediment sampling in the residual flow reach three different well established techniques are used (Table 9), such as collecting and sieving of the sediment material, picture based sediment distribution evaluation (Buscombe et al., 2010) with the program BASEGRAIN and the pebble count method (Bunte at al., 2004). The results were compared throughout the whole project period and the sieving results used to evaluate the substrate based shelter evaluation.

Table 9: List of the different methods applied at the testing spots

Data Point	Basegrain	Sieving	Pebble Count
#1	x	x	x
#2		x	x
#3		x	
#4			x
#5	x	x	x
#6		x	x
#7			
#8		x	x
#9			
#10			
#11	x	x	x
#12	x	x	x
#13		x	x
#14	x	x	x
#15	x		x
#16			x

All the three different techniques show advantages and disadvantages as a results of the circumstances of the sampling such as submerged spots vs. non-submerged spots etc. This can be seen in Figure 28 where smaller fractions are underrepresented in comparison with the other two methods. A reason might be that collecting / sieving is an invasive method and the very fine fractions might get lost during sampling.

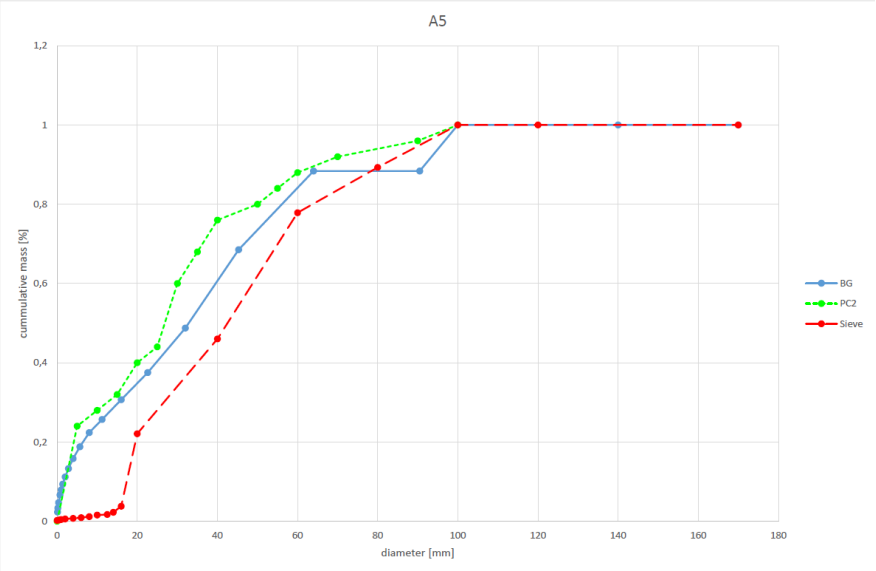

Figure 28: Results of sieving (red dashed), pebble count (green dotted) and BASEGRAIN (blue line) at spot number 5.

Evaluating the shelter availability, it shows as expected a quite big variation between different spots. This include also variations between spots which are very close to each other or between spots which show on the first sight similar conditions (such as for instance high flow velocities in not permanently wetted areas as for #1, red marker, and #5, green marker, in Figure 29).

Figure 29: Position of different sampling spots in the river. The colours of the ring marker indicate the shelter availability following the colour code of table 8.

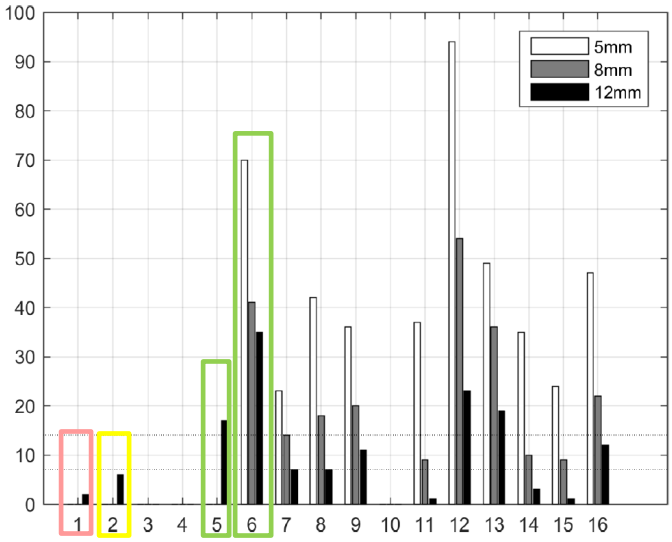

Figure 30: Sampling results for the shelter availability for the three different tubes at different spots.

Figure 30 shows, that for spot #2 (submerged, also Figure 29) for instance the shelter availability is counted to 2 with the 12mm tube, which results in a low availability, while spot #5 (part-time submerged) offers 17 shelters for the same tube size, which leads to a high availability.

The comparison of the grain size distributions between the different spots also shows a fairly big variation, especially for the finer fractions and above the 50%.

Following the method described in chapter 1.3 the sediment and shelter data are evaluated. The R-squared values in both cases are < 0.01 and hence the model cannot be seen as explaining the changes in the data. The fit is higher for the larger fractions, D50 up to D95 show a clearly better correlation with R-squared = 0.087, however it is not really good as well.

Now considering the assumed effect of the deposited sediment the data is evaluated separately for the different dates of the sampling. The results show a much clearer and better picture now (Figure 31). It can also be seen that the sampling right after the sediment deposition and the first distributing flood event is fairly affected by this event (R-squared = 0.019) while for the sampling event after the model shows a very good fit (R-squared = 0.855).

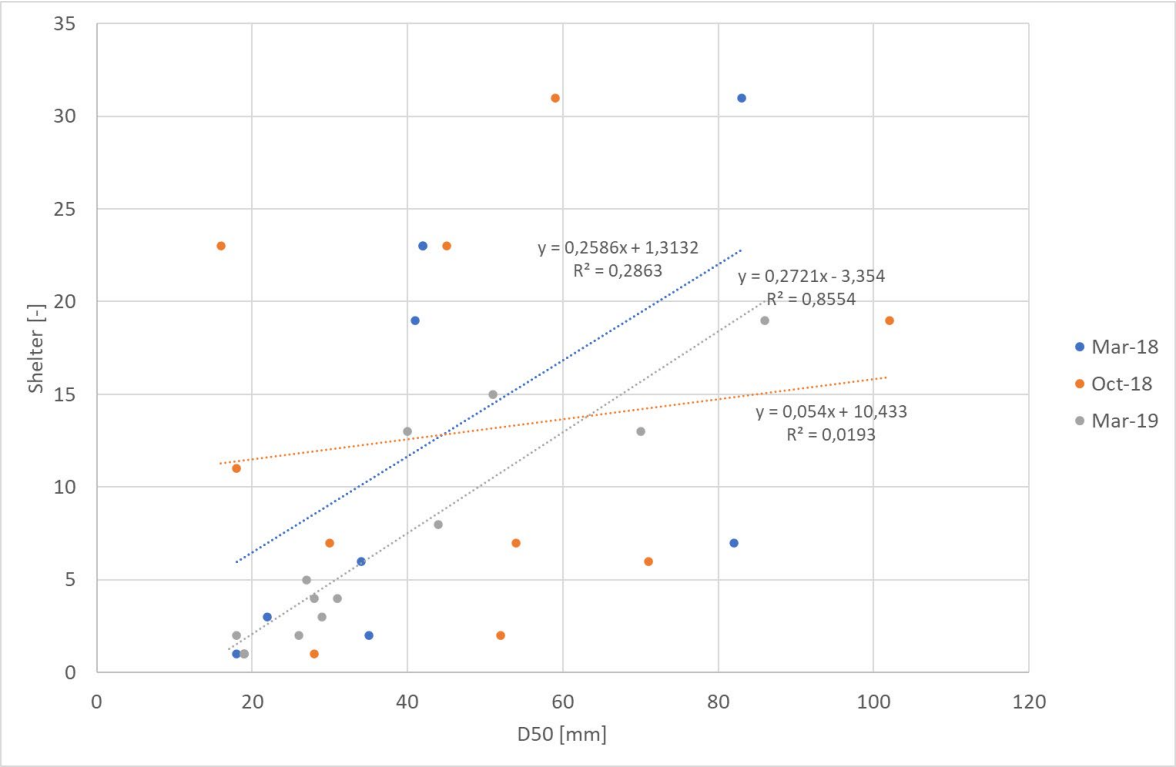

Figure 31: Correlation between D50 parameters and number of shelters with the R^2 coefficient separated by the date of the sampling campaign.

It can further be found, that in general the fit is the best for D50 in absolute terms, while the fit considering a lower difference between the different campaigns is better for higher fractions (Table 10):

Table 10: R-squared for different sampling dates and Dx values.

	R-squared March 2018	R-squared March 2019
D5	0.33	0.20
D10	0.18	0.50
D50	0.28	0.85
D84	0.37	0.60
D90	0.40	0.55
D95	0.42	0.53

3.2.4 Conclusion & Outlook

The method of correlating the sediment distribution patterns with the shelter does not apply only for Norwegian rivers, but also for Alpine rivers such as the river Limmat. The exact parameter, however, need to be adapted to the changed type of sediment mixture present. This cannot be found and determined based barely on the sieving data. To determine a correlation both, the presence of certain fractions and the availability of shelter need to be linked. Further the history of disturbance of the

respective area has to be considered, as the results for the correlation show a clear dependency of the sediment changes throughout the project time, which leads to the problem in interpretation, that detailed information of the sediment mixture of the added sediment is missing. Further results will be published in a paper summing up the results of this study for FIThydro.

In addition, numerical simulations are currently carried out to simulate the sediment movement throughout the residual flow reach. For these simulations we use the software tool SSIIM (Olsen, 1994; Haun et al., 2012; Harb et al., 2014). The discharges simulated are based on the relevant statistical flood events which are also simulated by the FIThydro partner AFRY (former AF-Consult for the whole test site.

The very first results with SSIIM show that even with a high discharge, mass movement is little and only the fine fraction of the total size distribution is transported. Further post processing will show the rate of change of the individual fractions in the bed mixture, which will allow to determine possible shelter in the residual reach.

3.3 Efficiency of downstream and upstream migration devices (ETHZ, FCO, LKW, AF-CONSULT)

At the residual flow HPP Schiffmühle**,** an angled fish guidance structures with horizontal bars, i.e. a Horizontal Bar Rack (HBR) has been implemented in 2013 to shield fish from the turbine intake and guide them into an adjacent bypass and to the tailwater. The current situation is documented through field monitoring and 3D numerical modelling in the area near the HBR-BS and the frontal weir. The monitoring comprises the characterization of the flow field and bathymetry using an Acoustic Doppler Current Profiler (ADCP), 3D numerical modelling and a survey of the fish movements. The latter is made with the PIT-tagging technique.

The detailed hydraulic data on the HBR-BS are obtained from the laboratory investigation in WP3, Task 3.5 (Meister et al., 2020a, b; Meister, 2020; FIThydro Deliverable 3.4, 2020), and served as a basis for the implementation of the HBR into the numerical model. The flow field around the HBR-BS, head losses and upstream and downstream flow fields at HPP Schiffmühle were simulated using the 3D numerical model. The results from the simulation are compared to the measured values to assess the performance of the numerical model and to deduce potential paths for improvement. Furthermore, fish movements and fish guidance efficiency of the implemented HBR-BS and fish passes were quantified by PIT-tagging technique (FCO). An antenna mounted in the bypass system and fish passes confirm the fish passage. Similar fish monitoring campaigns were carried out in two other HPPs upstream and downstream of HPP Schiffmühle on the river Limmat and the obtained data were shared by the operator Limmatkraftwerke. Finally, a comprehensive data set is compiled to study the fish movements on a larger scale. Hydraulics and fish data are evaluated to assess the fish guidance efficiency (FGE) of the HBR and fish passes. Furthermore, four variants of new bypass systems as an alternative to the current bypass system were numerically modelled and their hydraulic conditions were simulated in the scope of a study funded by Swiss Federal Office of Energy (SFOE) (contract number: SI/501759-01). The results of this study are published in https://www.aramis.admin.ch/Grunddaten/?ProjectID=41588 and are partly also included in this document.

3.3.1 Data

Data are collected from the field campaigns, the HPP operator and literature.

3.3.2 Methodology

- Velocity and bathymetry measurements using ADCP and Drone
- Numerical modelling of HBR and weir flow
- Fish monitoring using PIT-tagging technique

3.3.2.1 Hydraulics and bathymetry measurements (ADCP)

Acoustic Doppler Current Profiler (ADCP)

High-resolution 3D velocity as well as bathymetry measurements were conducted using an Acoustic Doppler Current Profiler (ADCP) mounted on a remote control boat in March and October 2018. The models of the ADCP and the boat are River Pro 1200 kHz including piston style four-beam transducer with a 5th, independent 600 kHz vertical beam and Q-Boat supplied by Teledyne Marine, USA, respectively (Figure 32).

The first campaign took place during an average river discharge of Q = 70 m^3/s from 13-15 March 2018, while the second campaign was done on 31st October and 1st November 2018 with an average river discharge of Q = 45 m^3/s. The main goals of both campaigns were to map river bathymetry and measure flow velocities in the upstream and downstream river reaches of the HPP. The data were used to construct, calibrate and validate the 3D numerical model, study the hydraulics of the HBR-BS at the HPP and quantify sediment erosion and deposition in the river. The post-processing was done according to the workflow sketched in Figure 33 using the software WinRiver II[1] and VMT[2]. In addition to the ADCP measurements, we measured flow velocities inside the downstream bypass inlet using a propeller type handheld probe.

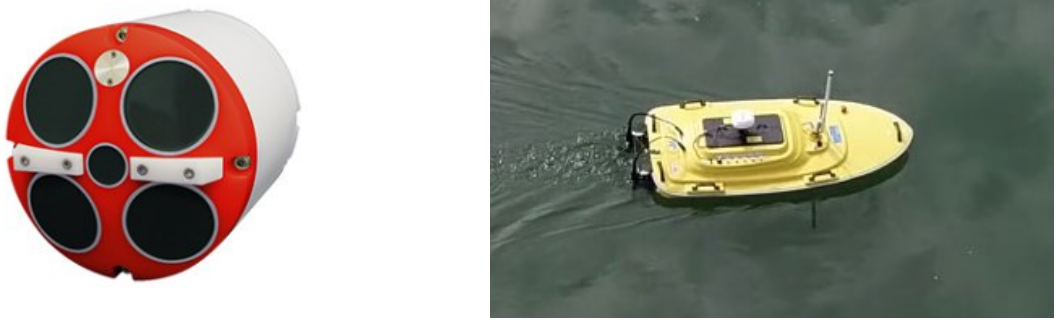

Figure 32: ADCP and Q-boat.

[1] Data collection and post processing software provided by U.S. Geological Survey
[2] Matlab based software for processing and visualizing ADCP data provided by U.S. Geological Survey

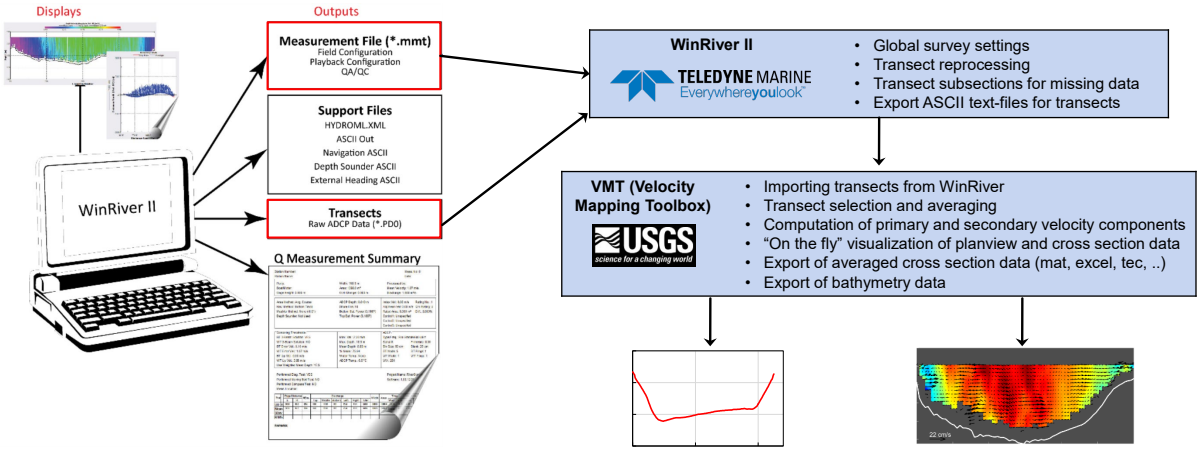

Figure 33: ADCP data analysis workflow.

ADCP measurement cross-sections at the first (46 cross-sections) and second field campaigns (69 cross-sections) are shown in Figures 34 and 35. Due to a low accuracy of altitude measurement with the DGPS system of the ADCP, we used a TS02 Leica total station and a target on the boat to determine the water surface elevation at each transect during the second field campaign (Figure 36).

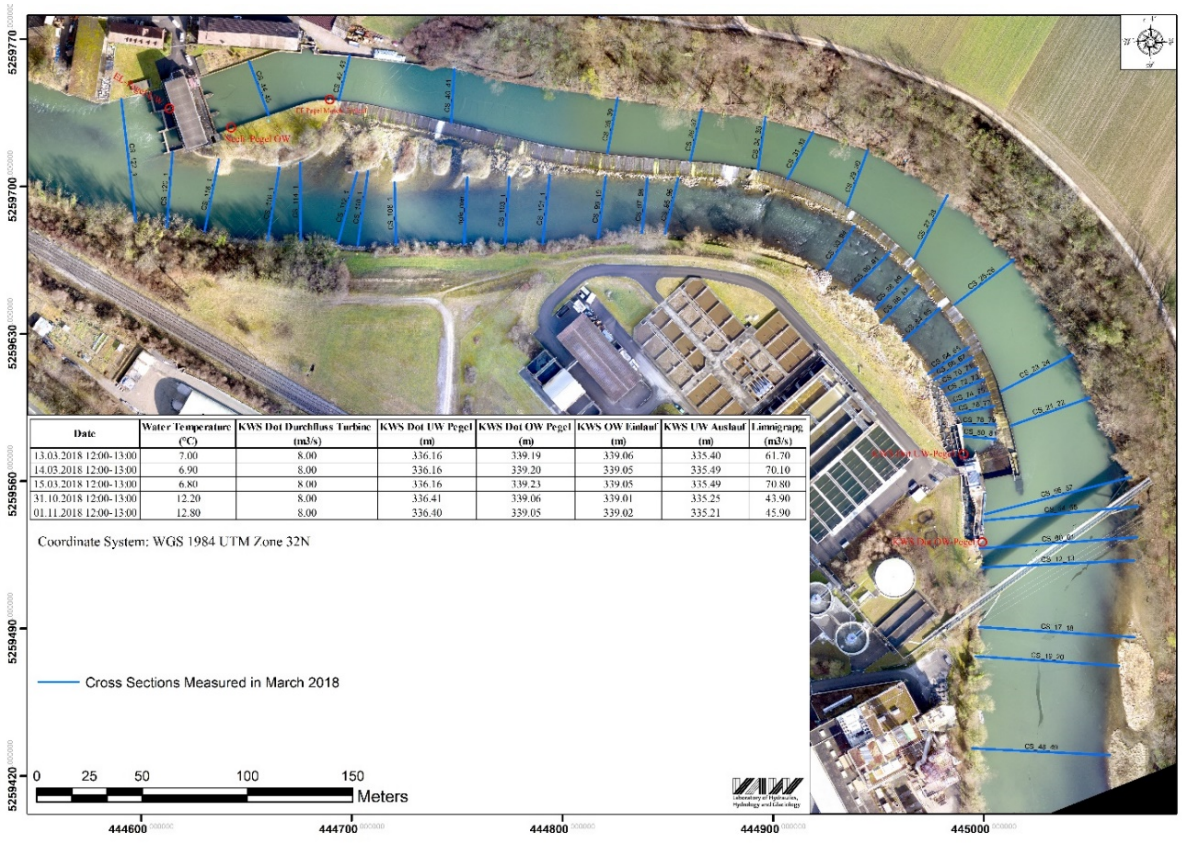

Date	Water Temperature (°C)	KWS Dot Durchfluss Turbine (m3/s)	KWS Dot UW Pegel (m)	KWS Dot OW Pegel (m)	KWS OW Einlauf (m)	KWS UW Auslauf (m)	Limnigraph (m3/s)
13.03.2018 12:00-13:00	7.00	8.00	336.16	339.19	339.06	335.40	61.70
14.03.2018 12:00-13:00	6.90	8.00	336.16	339.20	339.05	335.49	70.10
15.03.2018 12:00-13:00	6.80	8.00	336.16	339.23	339.05	335.49	70.80
31.10.2018 12:00-13:00	12.20	8.00	336.41	339.06	339.01	335.25	43.90
01.11.2018 12:00-13:00	12.80	8.00	336.40	339.05	339.02	335.21	45.90

Figure 34: Velocity and bathymetry measurement locations at HPP Schiffmühle in March 2018.

Figure 35: Velocity and bathymetry measurement locations at HPP Schiffmühle in October 2018.

Figure 36: Water surface elevation measurements using a total station and a target on the boat

3.3.2.2 Hydraulics (Airborne Image Velocimetry (AIV))

1) Measurement of dry topography

Regionalwerke Baden AG (Zabah, 2018) performed measurements to get a detailed data of the non-wetted topography. To this end, eleven ground control points (GCP) had been measured by geotechnical surveying on 2018/03/08 and a measurement flight had been performed on 2018/03/08 between 10:00-11:00 at a height of 140–145 m over ground. Based on 104 images, a high resolution 3D point cloud had been computed by photogrammetry software *PIX4D*, which combines structure from motion (SfM) technique with MultiView Stereo (MVS) methods. A Digital Surface Model (DSM) as well as an RGB orthoimage each with raster sizes of 0.0244 m had been computed out of it (Figure 37). Georeference is given by the new Swiss survey LV95.

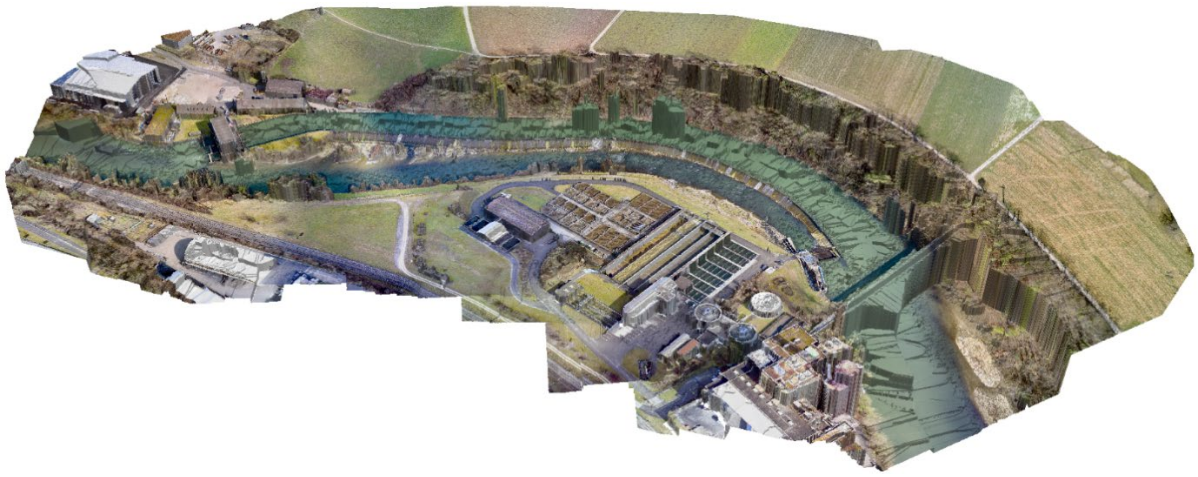

Figure 37: 3D snapshot view to the dry topography area observed by Regionalwerke Baden AG.

2) Measurement of surface velocity fields by Airborne Image Velocimetry

Airborne Image Velocimetry (AIV) measurements of surface velocities fields were performed on 2018/03/13 between 11:00-11:45 by VAW/ ETH Zürich (Figure 38). The flow discharge at this time was almost constant at 71–72 m^3/s, as deduced from the FOEN gauging station Baden-Limmat[3]. The goal of these measurements was to get an overview of the time-averaged far field approach flow.

The AIV technique applied was similar to the one presented by Detert at al. (2017). A crude description of the set-up, performance and image analysis is given in the following, with more information at details deviating from Detert at al. (2017). The AIV measurement setup consisted of an UAV *DJI Phantom 4 Pro+* with a weight of 1.4 kg including a three-axis Gimbal-stabilized action-camera. The latter has a 1" CMOS-sensor and the lens providing a field of view of 84° and a 35 mm focal length equivalent. The total cost of the quadcopter and accessories was below 2 kCHF (March 2018).

Surveying flights were performed at 30–70 m over ground, recording in h.256 video mode at 23.976 fps with a resolution of 4096×2160 px^2. To have a significant grayscale contrast on the video frames the flow was seeded with tracer from the upstream bridge, from a boat and from diverse riparian points during the measurements. Eco foam chips (*FILL-PAC Bio* from *MEDEWO*, Switzerland) were selected with diameters of 30-40 mm (Figure 38).

The total length of the video data set comprises > 20 min, which is too large to be analyzed in total. Therefore, a reduced data set consisting of 579 image pairs each with an internal time shift of $\Delta t_{0:1}$ =

[3] Station #2243, located 4.6–5.1 km upstream, with assumption of an average flow velocity of 1–2 m/s.

5/23.976 s and a median time shift of $\Delta t_{0:1–4:5}$ = 40/23.976 s between the image pairs had been chosen manually for the subsequent image analysis.

Image orthorectification was performed using the photogrammetry software *PhotoScan*, based on the 2×579 = 1158 image frames, combined with the eleven GCPs from Regionalwerke Baden AG (Zabah, 2018) and, to provide more supporting points for the computation, 17 additional characteristic markers as virtual GCPs (e.g. gully holes, larger stones) identified on their dry topography data set.

During the workflow process of *PhotoScan* a frame camera type setting was used to initialize implementation of a camera model that adequately fits the actual lens distortions. The whole process of photograph alignment at original resolution, including computation of camera parameters and positions took about 10 h computational time on a standard PC. The camera positions of the resulting sparse cloud had a reprojection error of ±0.2 px (in image coordinates). *PhotoScan* corrected the 3D coordinates of the GCPs by an average value of ±1.26 m according to the positions measured in the field and gave a reprojection error of ±1.2 px (in image coordinates) for all GCPs. The dense point cloud was reconstructed with medium quality, i.e. the images had been resized by a factor of four, and aggressive depth filtering within 17 h computational time on a typical office PC. The resulting point cloud had a density of 8.1 million points, which is >25 times higher than the density of the sparse cloud. A mesh with 420,000 vertices was build based on 4.5 million manually selected points of the point cloud, i.e. the dense point cloud with misleading points at the water surface and non-riparian points deleted. Finally, 1158 RGB orthoimages with raster sizes of 0.016 m have been exported for the subsequent image velocimetry analysis.

Flow velocities were determined by PIV via the previously described geo-referenced images. The images were converted to 8-bit grayscale, with each individual Gaussfilter-computed background image substracted, and the image intensity was adjusted and pixel values < 40 were capped – as described by the following MATLAB-code lines

```
I = rgb2gray(I);
J = imerode (imbinarize(I,0),strel('square',40));
I = imadjust((I-imgaussfilt(I,10)).*uint8(J));
I(I<40)=0;
```

Then, the MATLAB-based open source software *PIVlab* by Thielicke and Stamhuis (2014) was used to determine the surface flow velocities. PIV analysis was performed to the 579 image pairs in mode [(0,1), (4,5), (8,9), . . .] on a final window size of 64×64 px^2 with 50% overlap. Postprocessing comprised masking out non-water surface areas and applying a universal outlier detection method (Westerweel & Scarano, 2005) to the instantaneous velocity fields to eliminate misleading velocity vectors. The median value of the time series at each grid point was chosen to describe a characteristic time averaged surface velocity. Due to inhomogeneous flow-seeding conditions and non-perfect image orthorectification results (shivering between image pairs) the chosen approach is prone to overestimate near-zero flow velocities. Therefore, velocities <0.2 m/s finally have been deleted.

Figure 38: DJI Phantom 4 Pro and Ecofoam as seeding particles.

3.3.2.3 Fish monitoring

Fish have been monitored at HBR-BS and both vertical slot fish pass (VSFP) and nature-like fish pass (NLFP) using the PIT-tagging technique between 2017-2020 (Figures 39 and 40).

Two antennas in the NLFP and another two antennas in the VSFP detected the entrance behavior of fishes (Figure 39). One additional antenna at the exit of the fish pass registered the fish leaving the pass. One antenna was installed in the downstream bypass pipe to detect downstream migrating fish. All six antennas were connected to the readers recording detections at a rate of about 14 scans per second. Data from the readers were remotely downloaded and the function of the readers was controlled from the office.

Figure 39: PIT-Tag antennas (left picture in the nature-like fish pass, right picture in the vertical-slot pass.

Fish tagging started in September 2017. In the first year (2017), we tagged 549 fishes belonging to 10 different species. In 2018, 1'782 fishes belonging to 17 species were tagged. A total of 2'331 individuals tagged in 2017 and 2018 were released downstream of the fish passes. Additional tagging occurred in 2019 and finally 3'087 individuals were tagged at the Schiffmühle HP. Most of the fish were caught in the counting facilities (N=2'890), except 73 individuals that were electro-fished on 26-9-2018 upstream of the hydropower plant and translocated to downstream areas and additional 124 individuals caught in 2019 by electrofishing in the tail water. These 124 individuals were translocated upstream of the HPP to track the downstream migration behaviour. Smaller fishes (< 160 mm) were tagged with 12 mm PIT tags, larger fishes (> 159 mm) with 32 mm tags. We used HDX PIT-Tags from OREGON RFID

(Manufacturer Texas Instruments, ISO 11784/11785). With a small incision the tags were placed in the body cavity. For the handling fishes were anesthetized with clove oil (30 mg/l) (Figure 40). Before releasing fish back to the water they could fully recover from anesthesia. Fishes caught in the counting facilities and from the forebay were released after the recovery about 160 m downstream of the fish hydropower plant.

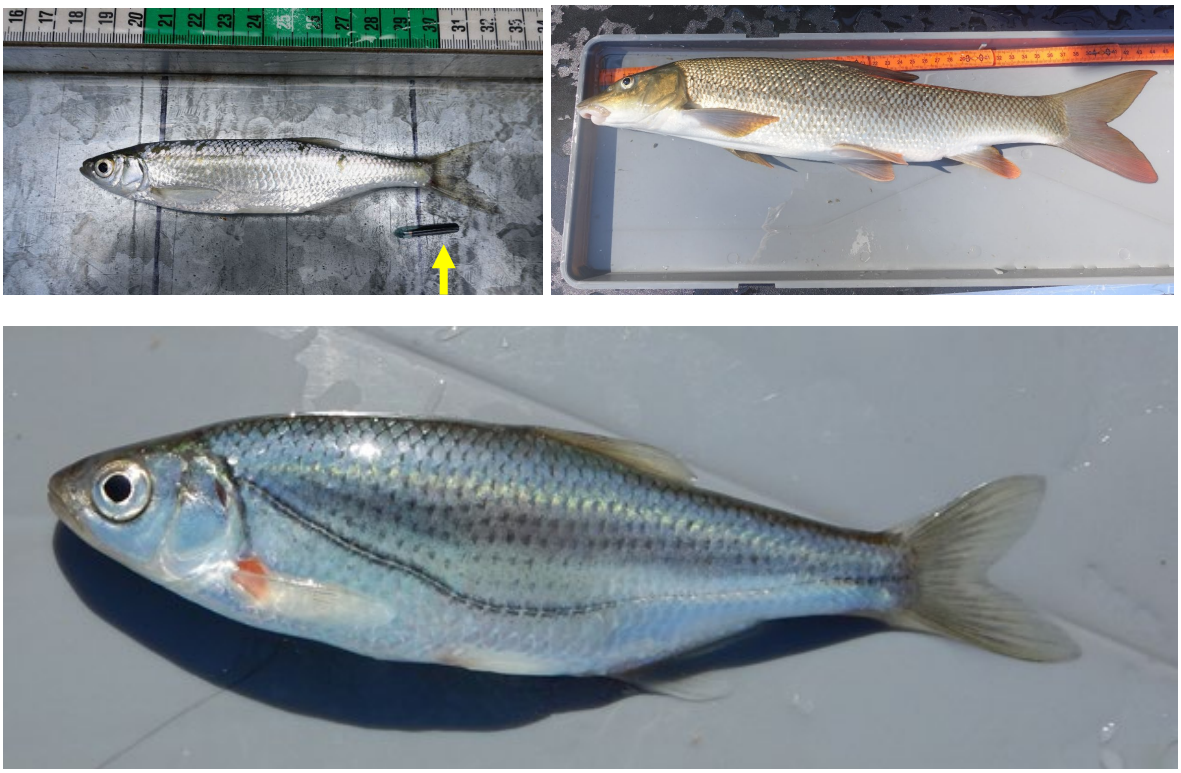

Figure 40: at the top: left: bleak with 12 mm PIT-tag, right: barbel, one of the most abundant species in the Limmat River. At the bottom: spirlin. Bleak and spirlin are small-sized fish species.

3.3.2.4 Hydraulics (Numerical modelling)

Flow conditions upstream and downstream of the HPP were simulated with the software FLOW-3D (Flow Science, 2014). The goal is to simulate flow conditions at the in- and outlets of the fish migration structures at variable Limmat discharges and, accordingly, with variable operating conditions of the hydropower plants. The following modelling concepts were applied.

Horizontal Bar Rack-Bypass System (HRB-BS)

The HBR-BS was simulated in FLOW-3D by applying a baffle. This allowed to account for the hydraulic effects of the rack without having to simulate each individual bar by direct numerical simulation with a resolution fine enough to properly resolve its hydraulic effects – an almost impossible endeavour given the trash rack size and bar spacing. It has been shown by specific research (Krzyzagorski, 2016), that the representation of a trash rack by a baffle leads to correct hydraulic effects.

Since the rack was not aligned with the orthogonal model cells, FLOW-3D fitted the rack in a stepped shape on the grid. This artificially increased the rack surface. By reducing the porosity of the rack, the increase was compensated as follows:

$$\phi_{model} = \sin(\alpha) \cdot \phi_{rack}$$

where:

ϕ_{model} Porosity to be entered into model

ϕ_{rack} Porosity of the rack

α Angle between grid and rack (0 = aligned)

With this correction, the open surface of the rack and therewith the flow velocities within the rack were properly represented.

The horizontal direction of the approach flow was not influenced by the rack since the bars were horizontally arranged. The impact on the vertical flow direction was not considered here because of the small vertical velocity component.

The loss coefficient assuming a 5 % obstruction and perpendicular flow was calculated based on the formula developed by Meusburger (2002, pages 170/171).

$$\zeta_{obstruction} = \left(\frac{P}{1-P}\right)^{\frac{3}{2}}$$

where P is the obstructed flow area. With 5 % obstruction the coefficient is 0.012. Oblique flow direction is directly accounted for by the FLOW-3D simulation.

Turbine

The flow through the turbine was not simulated. The model ended before the impeller with an outflow rate boundary condition equalling to the turbine flow. The water was returned to the model by an equivalent inflow boundary condition at the end of the suction tube.

Fish downstream migration device

The bypass system of the HBR is designed for a bypass flow of Q_b = 0.170 m^3/s when the weir flap is fully raised. The inlet of the device consists of two rectangular openings at different depth in the side wall of the HPP structure approximately 4 m upstream of the weir. The openings lead to a chamber from where a DN250 pipe leads to the residual flow river section. In the model, this flow was specified by an outflow boundary condition at the top and an inflow boundary condition at the bottom of the pipe.

Fish passes for upstream migration devices

To limit the computational power of the simulations the flow through the VSFP and NLFP was not explicitly simulated over the entire length of these structures. Only the flow through the lowest pools of each of the structures was simulated, such that the attracting flows in the residual water section were well represented by the model. The discharges are known and set in the model with outflow and inflow boundary conditions.

Model geometry

For generation of the model geometry, two types of data were combined:

1. As-built drawings of the structures of the residual HPP and of the near-natural bypass.
2. Bathymetry data measured in the present project and additional cross sections further upstream and downstream recorded by Swiss Federal Office of Environment (FOEN) in 2013.

From the as-built drawings a 3D geometry of the residual HPP was established (Figure 41). The bathymetric cross sections used for establishing the geometry of the Limmat river, the headwater channel and the residual flow section are displayed in Figure 42.

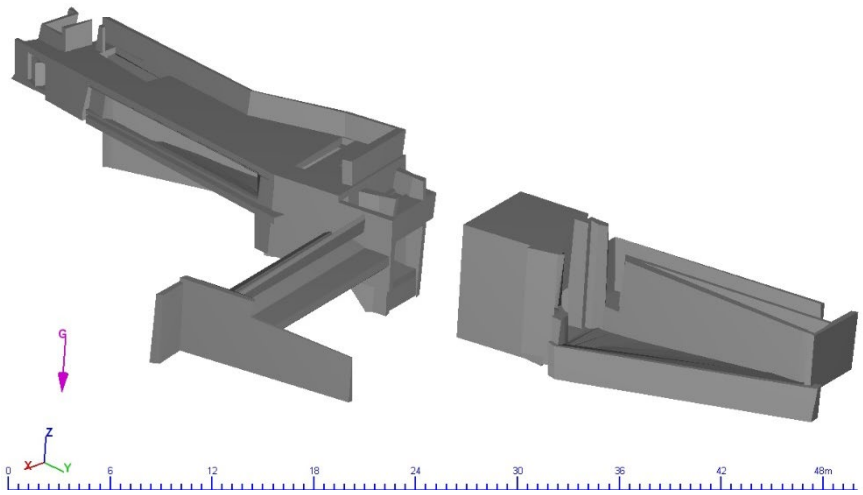

Figure 41: 3D geometry of the residual HPP with upstream (left) and downstream (right) parts

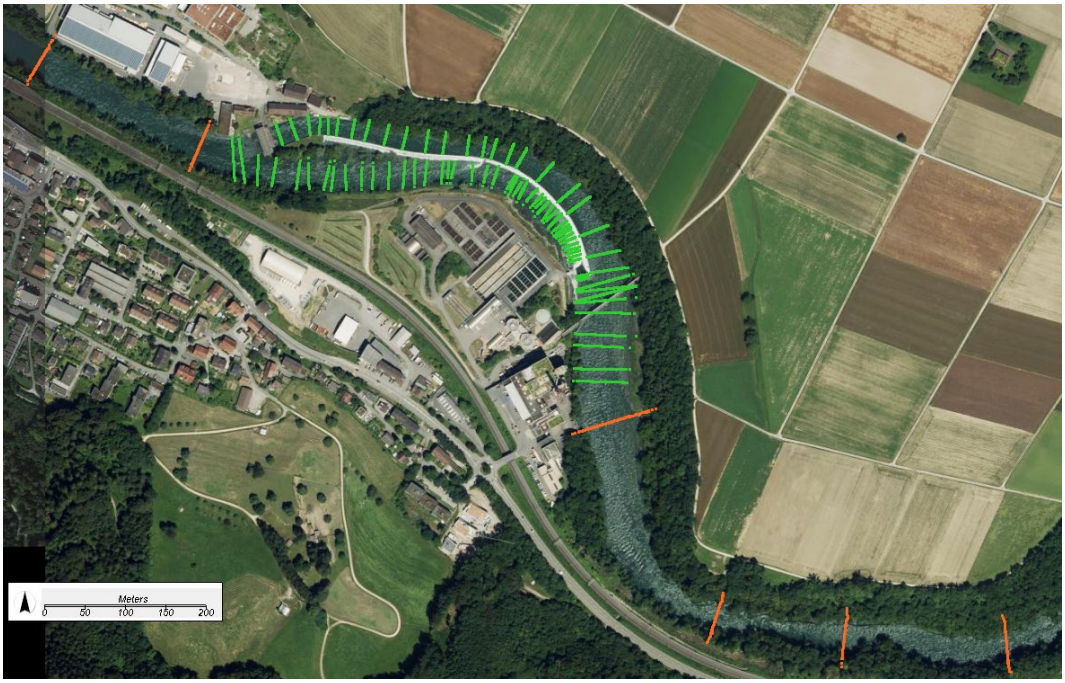

Figure 42: Available bathymetric cross sections, green (this project) and orange (FOEN, 2013).

Boundary conditions

Inner model boundary conditions for individual elements such as the turbine, the fish downstream migration device and the fish upstream migration devices are described in above sections. The outer model boundary conditions are defined as:

- Inflow boundary condition at the upstream
- Water level to discharge relation at the downstream

Flow condition scenarios

The goal is to simulate flow conditions at the in- and outlets of the HBR-BS and both fish passes at variable Limmat discharges and, accordingly, with variable operating conditions of the hydropower plants.

The Limmat discharge conditions and operating conditions for which the model are selected in a two-step approach:

1. Only the periods in which fish migration occurs are considered. These are mid-May to mid-June in springtime and September till beginning of October in fall. In these periods the three residual flow allocations of 8, 10 or 14 m^3/s can occur. As seen in Figure 43, four sub-periods with different prescribed residual flows must be considered.
2. For these four sub-periods, the Limmat hydrograph is analysed and Limmat flows of 5 %, 20 %, 50 % and 95 % are evaluated (Table 11, Figure 43). In total a set of 16 flow conditions are thus considered to be studied as scenarios.

It can be noted that weir overflow, starting at 123 m^3/s, takes places for 6 out of the 16 scenarios.

Flow structures around bypass inlet, in front of the HBR and weir are of prime importance to evaluate the efficiency of HBR-BS. Simulations in these areas were run for the river discharge of 100 m^3/s (~ mean discharge with 50% exceedance probability in migration months) with all possible discharges through residual flow power plant (8,10,14 m^3/s).

Table 11: Limmat flow conditions and prescribed residual flows during fish migration periods in spring and fall.

Period	Q_{Limmat}				$Q_{residual}$
	5%	50%	80%	95%	min.
2nd half of May	295	125	98	68	10
1st half of June	289	136	95	62	14
September	227	91	61	45	10
1st half of October	173	82	57	43	8

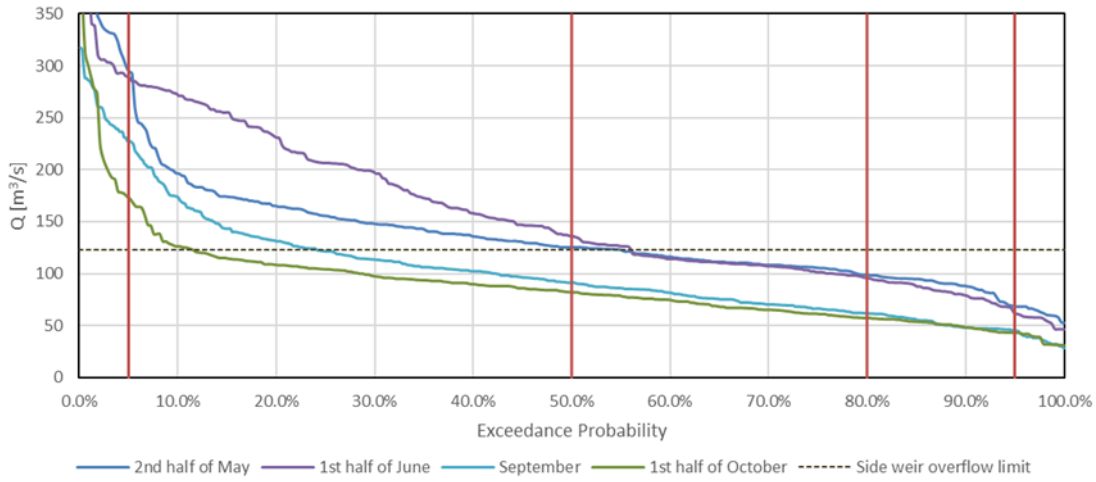

Figure 43: Flow duration curves established based on 1997-2018 Limmat flow data for the four sub-periods of fish migration.

3.3.3 Results

3.3.3.1 Hydraulics and Bathymetry data (ADCP)

During the field measurements, the discharge in the river Limmat slightly fluctuated around $Q = 70$ m^3/s and 49 m^3/s in March and October 2018, respectively. The discharge of the residual flow HPP was around 8 m^3/s and the total discharge in the residual flow reach was approx. 10 m^3/s including the discharges from the HPP, fish passes, downstream bypass flow and the side weir along the headwater canal in both field measurements.

Figure 44 show the upstream and downstream river reach bathymetry in March and October 2018. It is clearly seen that the bathymetry in the headwater canal changed and deepened from March to October 2018. This is mainly because of the removal of settled gravels from the headrace channel in September 2018. The removed gravels amounted to approx. 5300 m^3 calculated using the bathymetry maps and were damped into the residual flow reach (Figure 45). Such replenishment of gravels is considered as a measure to improve the downstream fish habitat and to mitigate river bed armouring, bank erosion, channel incision. Major bathymetry and flow depth changes occurred between the vortex tube and the residual flow HPP causing high flow velocities around the fish pass inlets (Figure 46). We expect that after several flood events, the damped gravels will be transported further downstream of the main HPP and the bathymetry of the residual flow reach will become similar to that in March 2018 with improved habitat quality. Therefore, for 3D numerical model, the bathymetries of the residual flow reach in March 2018 and that of the headrace channel in October 2018 were used.

Figure 46a and b shows the depth-averaged flow velocity distribution in the upstream and downstream flow reaches of the HPP Schiffmühle in March and October 2018, respectively. Note that the river discharges were different but the discharges in the residual flow reach were similar in March and October in 2018. The flow velocity increases from the downstream of the residual flow HPP up to the entrance of the fish ladder and reaches its maximum of 250 cm/s in October 2018 due to bathymetry changes caused by gravel replenishment in September 2018. Downstream of that location, it gradually decreases along the river reach until the downstream of the main powerhouse. In this region, a similar trend is observed in velocity distribution measured in March 2018 (Figure 46a). Although velocity magnitudes are different in March and October 2018, the overall velocity distribution in the headrace channel has changed because of gravel removal in September 2018 compared to that in March 2018.

One of the foci of the present study is to investigate the hydraulics and efficiency of HBR-BS in HPP Schiffmühle. To this end, we conducted densely-spaced ADCP measurements as well as velocity measurement inside the bypass at the HPP. Figure 47 shows the depth-averaged velocity distribution and streamlines around the HPP measured in October 2018. The flow velocities are high just upstream of the HPP close to the left bank of the river. Velocities slightly decrease towards the turbine intake. A discharge of 8 m^3/s goes into the turbine intake and a little flow goes towards the weir and the bypass inlet. The rest of the flow, i.e. about 41 m^3/s, goes into the headrace channel corresponding to about 80% of the river discharge. As indicated with red arrows in Figure 47, most of the fish in the river follow the main stream towards the headrace channel, while a small portion swims towards the HPP. When fish arrive at the HPP, it is likely that they do not find the bypass entrance because of the re-circulation zone and low velocities between the weir and the bypass inlet compared to high flow velocity at the turbine intake (Figures 47 and 48). The design discharge of the bypass is 0.170 m^3/s and the corresponding average velocities in front of the bypass, at two rectangular bypass openings and in the pipe are approx. 0.35 m/s, 2 m/s and 3.46 m/s, respectively (Figure 49). However, the ADCP field data show that the velocity in front of the bypass is around 0.10 m/s instead of 0.35 m/s (Figure 48). To confirm this result, we measured velocities inside the bypass and show the measurement points and velocity data in Figure 49. The average flow velocity at the two rectangular bypass openings is 0.66 m/s and the total bypass discharge amounts to 0.055 m^3/s. For this bypass discharge, the average flow velocity in front of the bypass is 0.11 m/s (Figure 49b), which is in agreement with the ADCP measurement. The measured bypass discharge is less than 1/3 of the design discharge, which is likely due to clogging of the bypass pipe. Although the bypass pipe entrance is regularly cleaned according to the operator, the clogging seems to be unavoidable. Overall, due to mainly the re-circulation zone, low flow velocities in front of the bypass as well as almost zero tangential velocity between the turbine and bypass intakes, the fish guidance efficiency of the bypass system is expected to be low. We discuss this result together with the fish monitoring result in the next subsection and present alternative solutions studied with 3D numerical modeling.

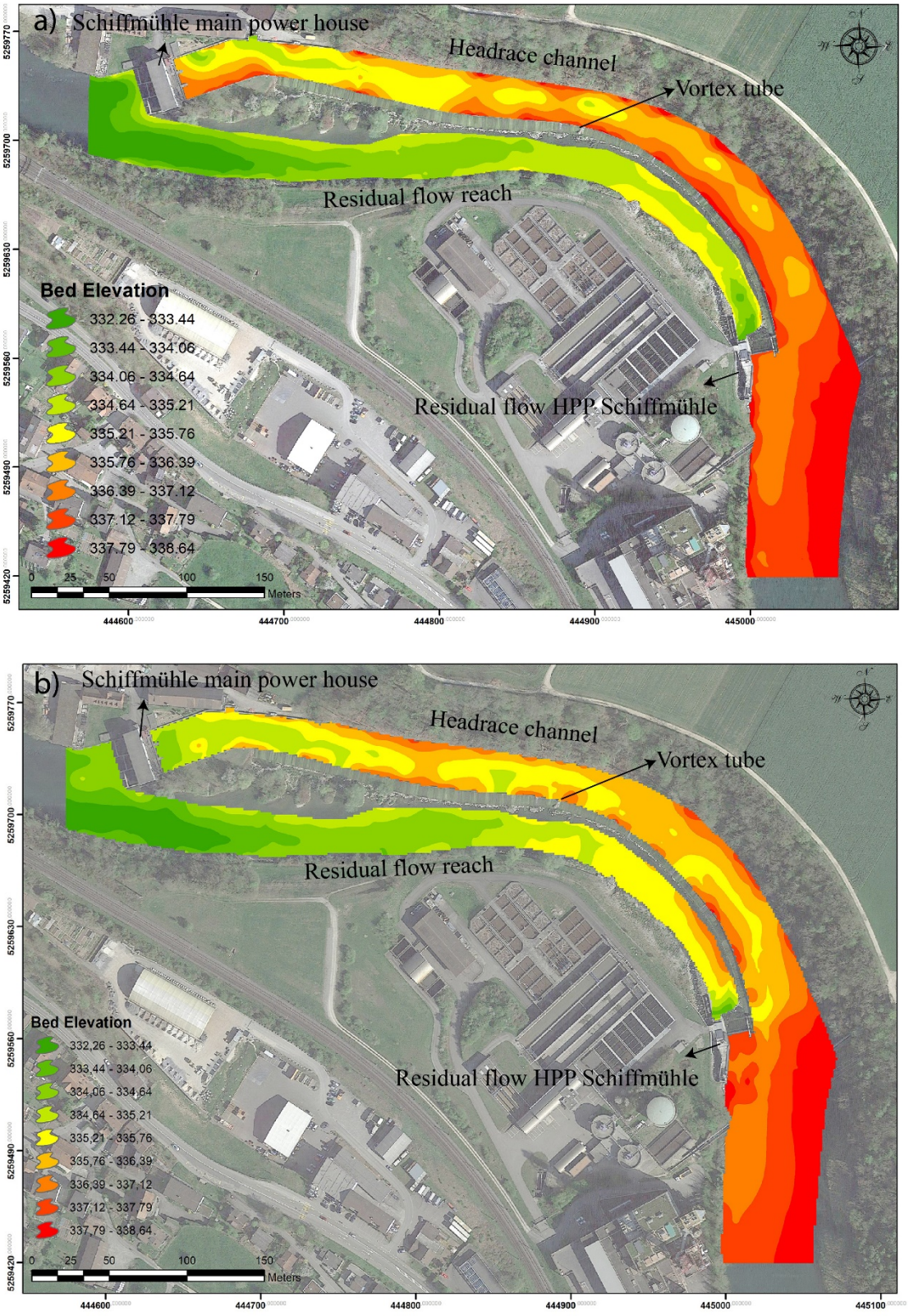

Figure 44: Bathymetry of upstream and downstream flow reaches of the residual flow HPP Schiffmühle in March (a) and October (b) 2018.

Figure 45: Photos of residual flow reach in March (a) and October (b) 2018.

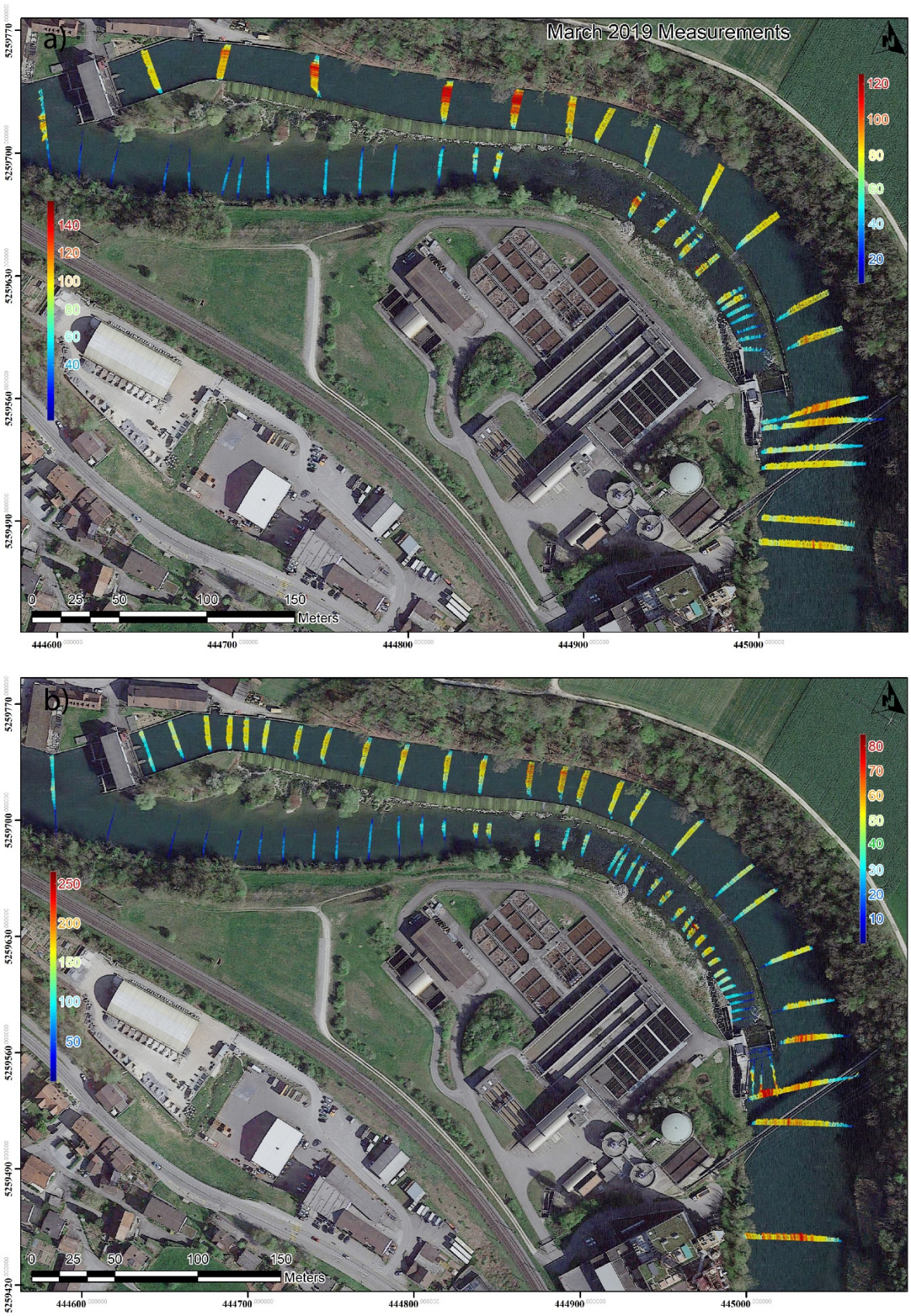

Figure 46: Depth-averaged velocity profiles from ADCP measurements at HPP Schiffmühle in (a) March and (b) October 2018. Note that the left and right colorbars are for the residual flow reach and headrace channel, respectively.

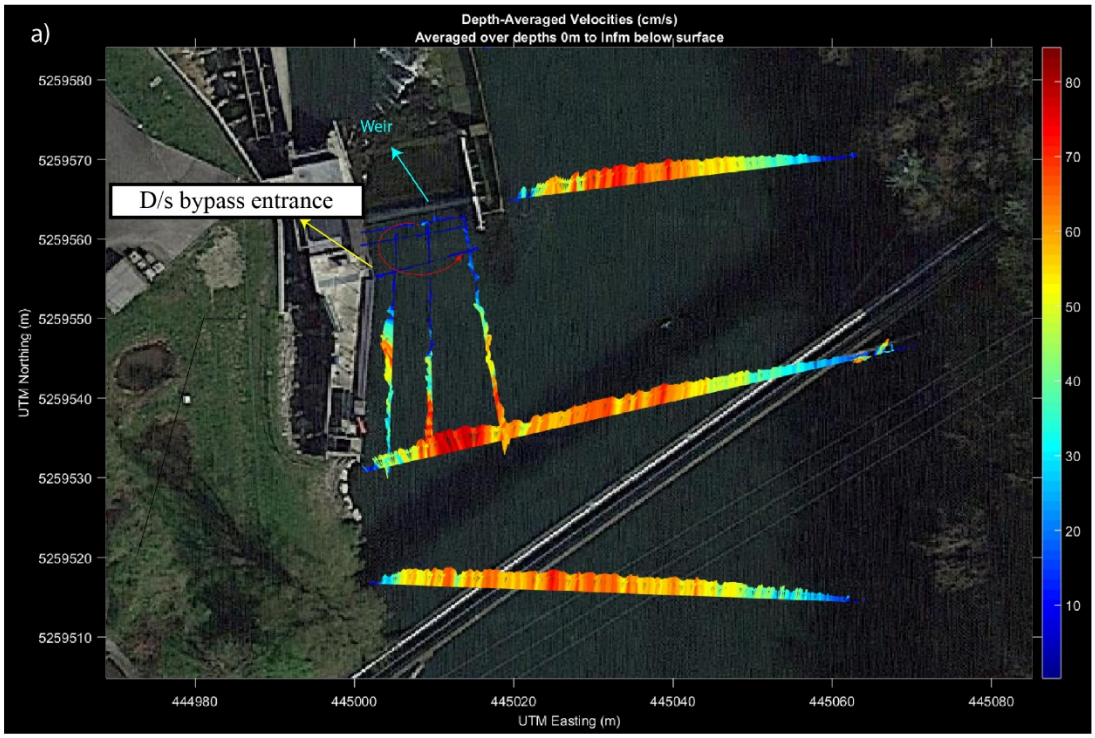

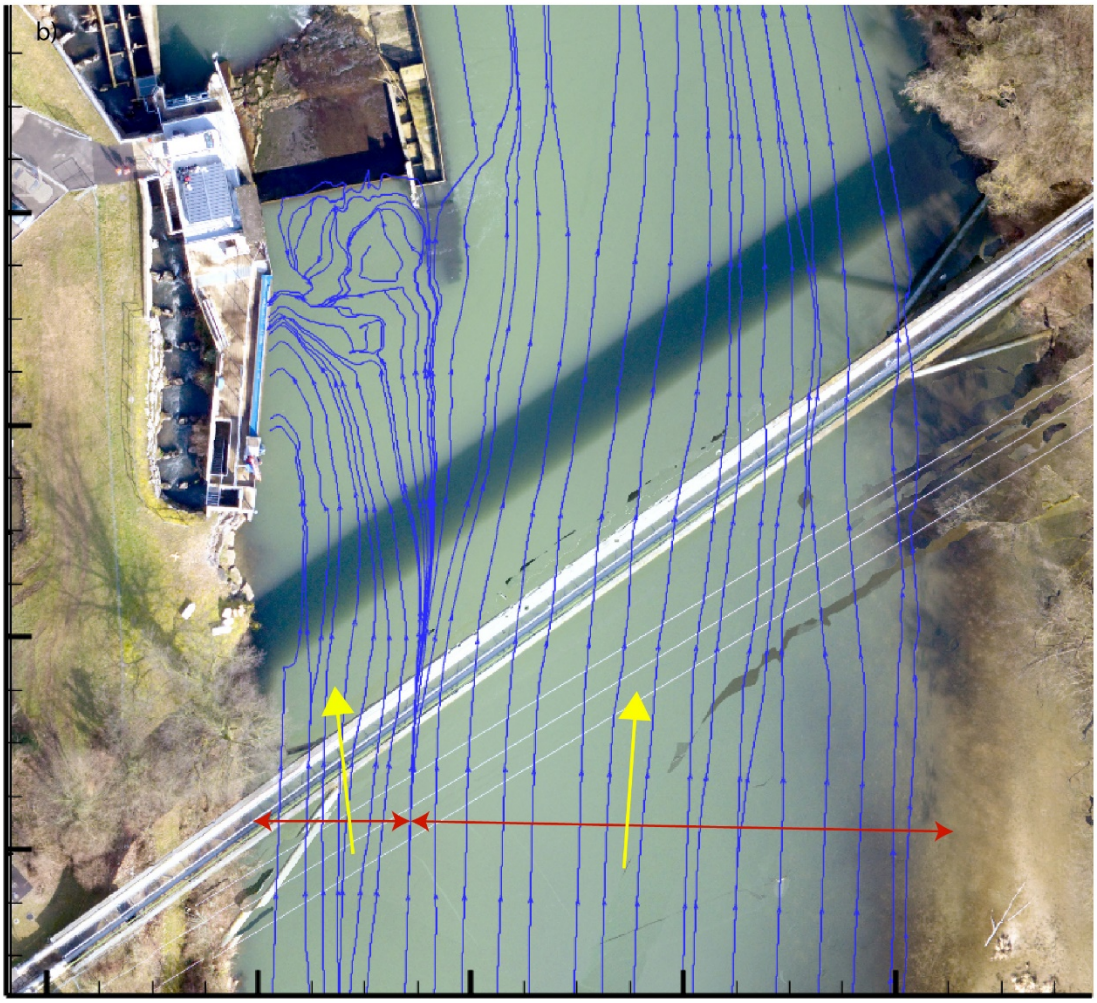

Figure 47: Depth-averaged velocity profiles (a) and streamlines (b) from ADCP measurements at HPP Schiffmühle in October 2018.

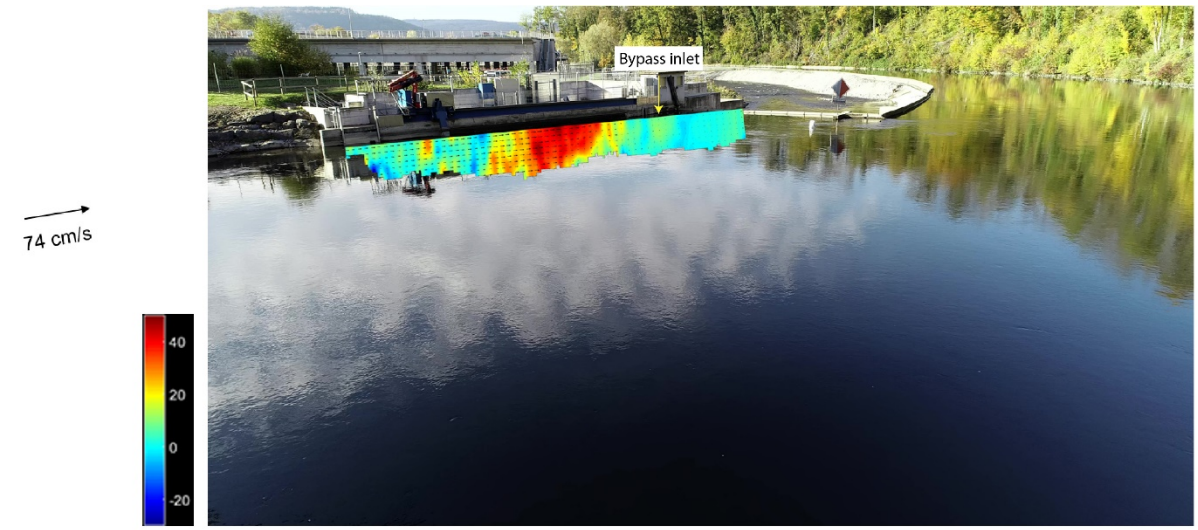

Figure 48: Velocity distribution along the HBR-BS in October 2018.

a)

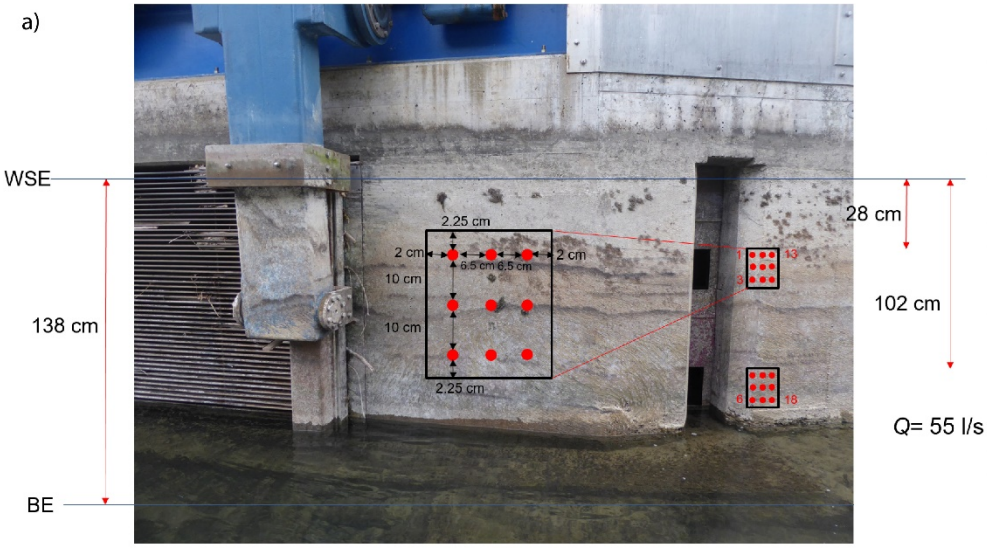

Point	Velocity (m/s)
1	0.66
2	0.72
3	0.70
4	0.66
5	0.73
6	0.64
7	0.65
8	0.66
9	0.75
10	0.75
11	0.72
12	0.66
13	0.65
14	0.63
15	0.52
16	0.48
17	0.63
18	0.70

b)

Figure 49: Velocity measurement points inside the bypass and velocity data (a) and average velocity in front of the bypass (b).

3.3.3.2 Hydraulics (AIV)

Figure 50 shows the resulting time-averaged surface velocity field. Note that according to Le Coz et al. (2010), depth-averaged velocities can be estimated by multiplying the surface velocity by factors of between 0.79 and 0.89, with a central value close to 0.85. Figure 51 presents the corresponding streamlines. It becomes obvious how the main flow is deflected to the outer bend of the headrace channel. The main flow must be accompanied by a strong streamwise-clockwise rotating secondary current that dives down a few meters before it reaches the right bank. There, a smaller streamwise-anticlockwise rotating secondary current is indicated by much slower flow velocities. The turbine approach flow upstream of the HBR-BS at the residual flow HPP has surface flow velocities of around 0.6–0.7 m/s, with the streamlines being deflected towards the turbine only a few meters upstream of the horizontal bar rack, which is in a good agreement with ADCP data (Figures 46a and 47b). The reach of the residual flow can be subdivided into two parts: (i) The area around the fish pass is affected by the turbine outlet of the residual flow power plant with surface velocities slightly above 1.0 m/s and (ii) the transverse ground sill downstream of the nature-like fish pass entrance that retains the water and slows down the surface velocity to 0.6–0.7 m/s. Downstream of the ground sill the flow is quite inhomogeneous and locally reaches surface velocities of up to 2.0 m/s in maximum.

Unfortunately, some areas show misleading flow velocities that obviously do not represent reliable flow physics. They are exemplarily highlighted in Figure 50. There are multiple reasons for this noise, such as a lack of seeding, white water, sun reflections, and higher riparian vegetation apparently moving with the moving camera position. Currently, VAW develops adequate techniques to avoid such noise directly during the video recording and to filter out falsified velocity vectors afterwards. As wrong velocity vectors in AIV are, in tendency, smaller than the real velocity, falsified time-averaged velocities are typical too low. Thus, local velocities have to be compared with neighboring velocities every time, and, in case of doubts, faster velocities are supposed to be closer to real–world situations.

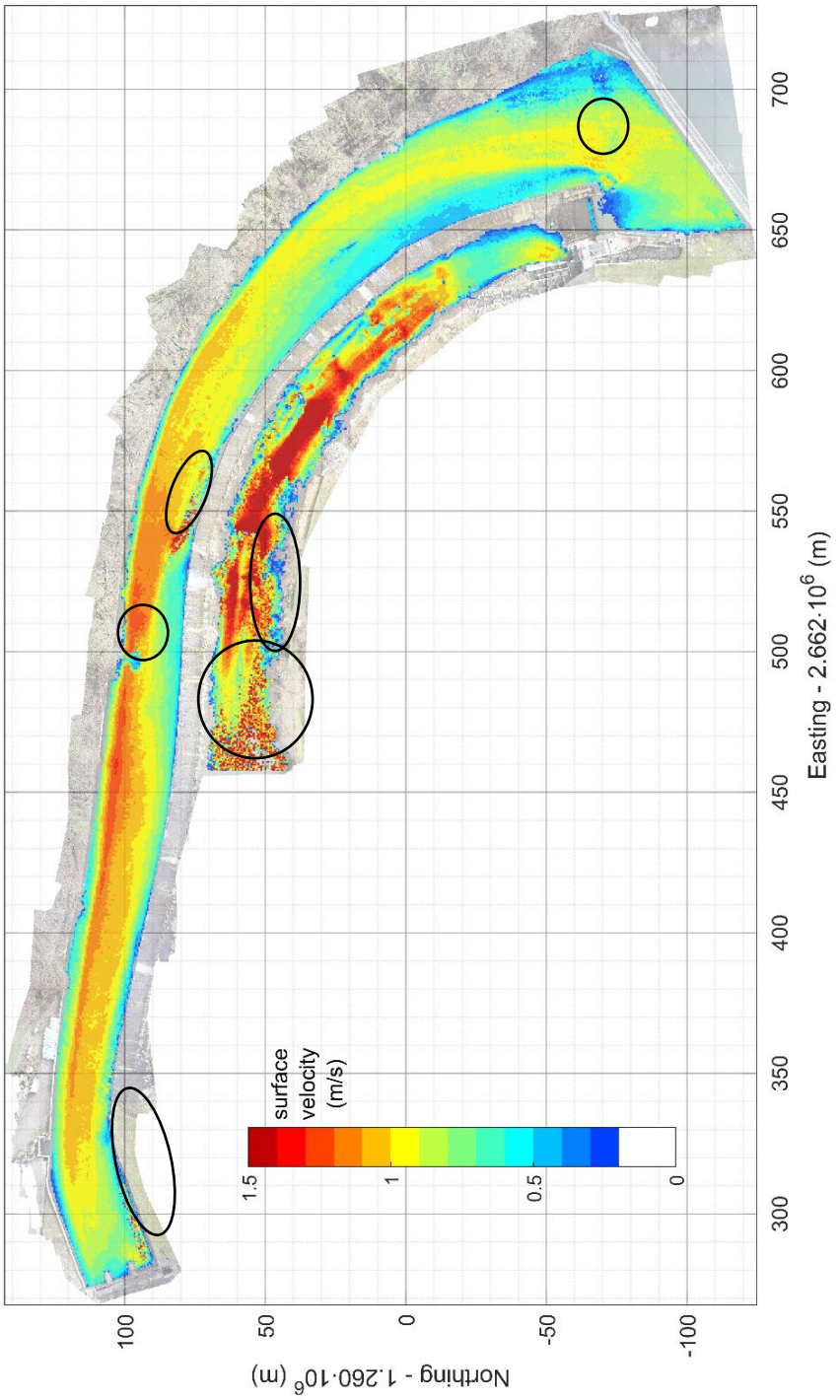

Figure 50: Geo-referenced surface velocity field measured using AIV on 2018/03/13 between 11:00-11:45 at a flow discharge of 71–72 m^3/s, with exemplary areas of misleading (noisy) velocity data highlighted by black ellipses.

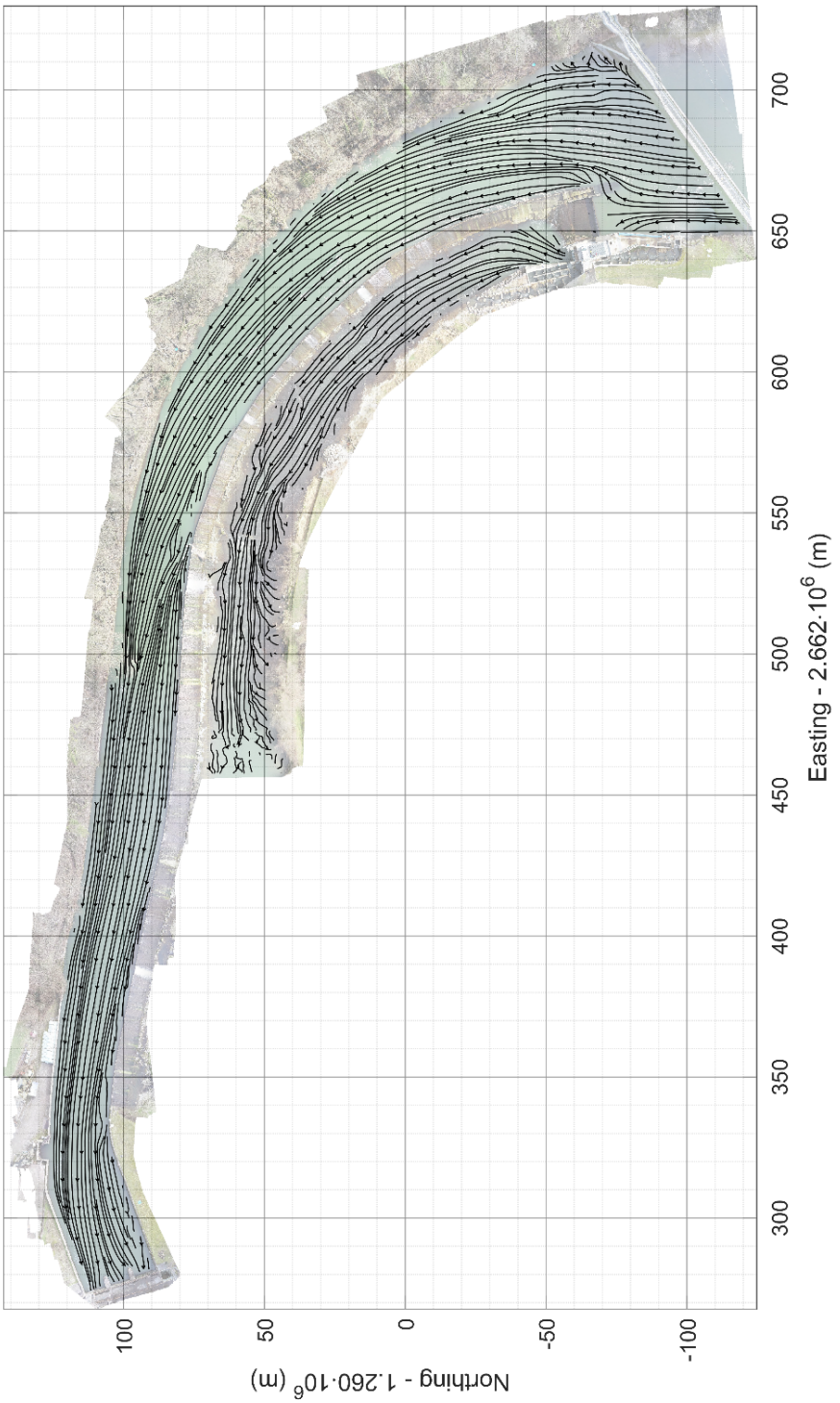

Figure 51: Geo-referenced surface velocity streamlines computed from AIV results.

3.3.3.3 Hydraulics (Numerical modelling)

Validation of 3D model

The validation of 3D model was made by comparing the ADCP data of VAW from velocity field measurements during March and October/November 2018. For the residual flow reach, the data from March 2018 were used, since the bathymetry was similar to the numerical model. For the headrace channel and the river discharge, the data from October/November 2018 were used, since the gravels in the power channel were already removed and the bathymetry in the numerical model is the same.

For the numerical validation the following discharges were used, corresponding to the discharges measured with ADCP in October/November 2018:

- River Limmat discharge: $Q_r = 45$ m^3/s
- Residual flow HPP turbine discharge: $Q_t = 8$ m^3/s and discharges at fish passes and the bypass system: $Q_f = 0.50$ m^3/s and $Q_b = 0.17$ m^3/s, respectively
- Discharge of the main HPP: $Q_m = 36.66$ m^3/s

General Comparison

First some general comparisons between the measured and the modelled data are executed. The measurements were conducted in October /November 2018. The flow pattern and magnitude of the compared data sets match well as shown in Figure 52. Figure 53 demonstrates the streamlines in front of the intake of the residual flow HPP and the bypass system. The main current flows through the rack into the power plant. In front of the weir streamlines build turbulent structures and backwater patterns. The graphical representations of the streamlines from measured and modelled data are in a good agreement. The measured water level in the Limmat/ headrace channel, at the gauging station at the fish slot pass matches the water level value from the model (2 cm difference, compared to Figure 54).

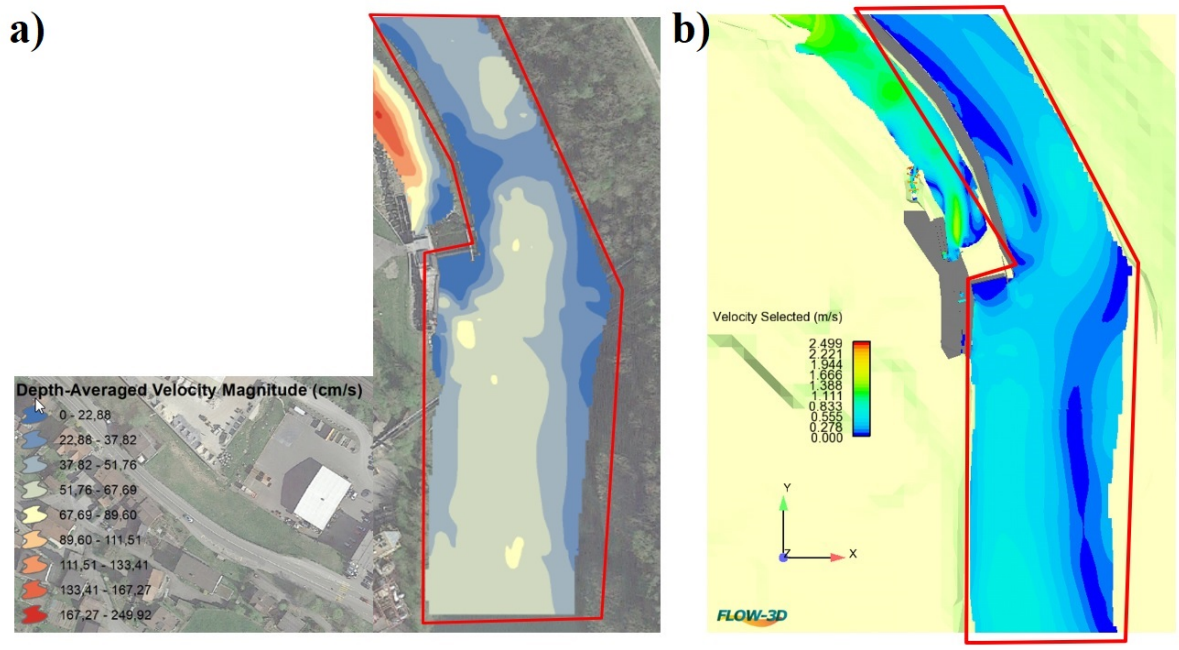

Figure 52: Velocity distributions in front of HBR-BS from ADVP data (a) and numerical model (b).

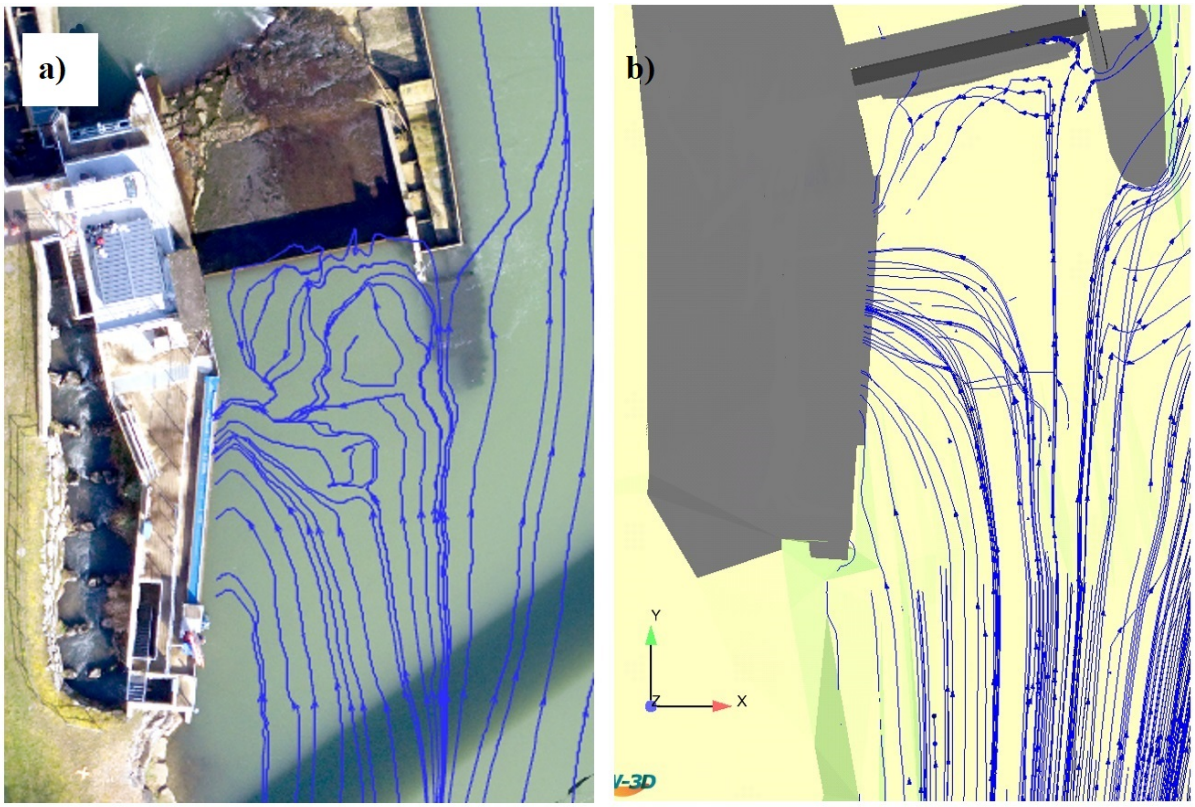

Figure 53: Streamlines in front of HBR-BS from ADVP data (a) and numerical model (b).

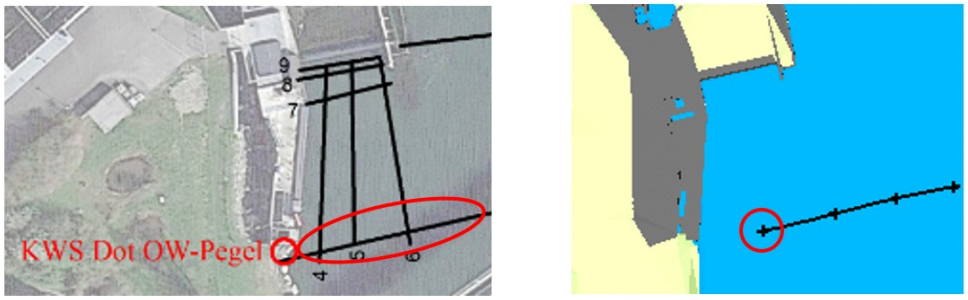

Figure 54: Flow elevations in the headwater of the residual HPP (left: ADCP data, right: Numerical model).

Velocity in Cross Sections

An optical validation of flow velocities on significant cross sections is highlighted in Figure 54. The cross-sectional velocity distributions at cross section 3 and 7 (Figure 55) are shown in Figures 56 and 57, respectively.

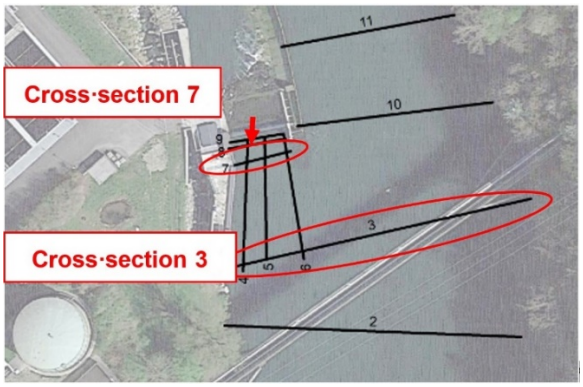

Figure 55: Cross Sections for comparison between ADCP and numerical model data.

Figure 56 shows the streamwise velocity distribution from the ADCP measurements and numerical model (in case of the 3D model in y- direction) at cross section 3. The highest flow velocities (~0.6 m/s) are located right in front of the residual flow power plant whereas the flow velocities decline towards the right boundary (~0.4- 0.1 m/s). The numerical model velocity data match well with the ADCP data at this location.

Figure 57 shows the streamwise velocity distribution from the ADCP measurements and numerical model (in case of the 3D model in y- direction) at cross section 7 in front of the weir of the residual flow power plant. The flow velocities are quite low and even a reverse flow at the left part around the inlet of the bypass occurs. The highest flow velocities (~0.2 m/s) are located on the right side, close to the central pillar between the residual flow channel and the headrace channel. Right in the middle of the channel the river water is accumulated and the flow velocity declines towards 0 m/s. Once again, the numerical model velocity data match well with the ADCP data at this location.

It is clearly seen from figures 56 and 57 that typical flow patterns, like maxima, minima of the velocities and flow distribution over the cross section, are similar between the ADCP and numerical data. Water flow is only tangible for a constant point of time since flow velocity pulsates in the system. The ADCP measurements deliver a representation of a current situation, which equals the flow velocity at a particular time serving as an auxiliary value. Therefore, the modelled and measured data can differ slightly. It is concluded that the flow velocity pattern matches the measured data in general and the validation process was successful.

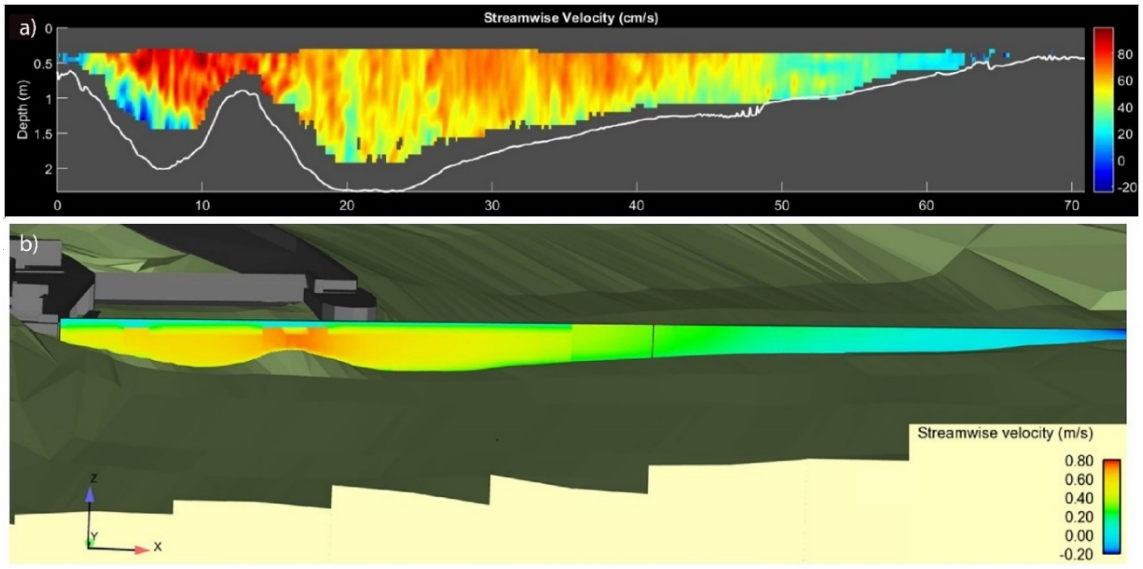

Figure 56: Streamwise velocity distribution from ADCP measurements (a) and numerical model (b) at cross section 3 (see figure 55).

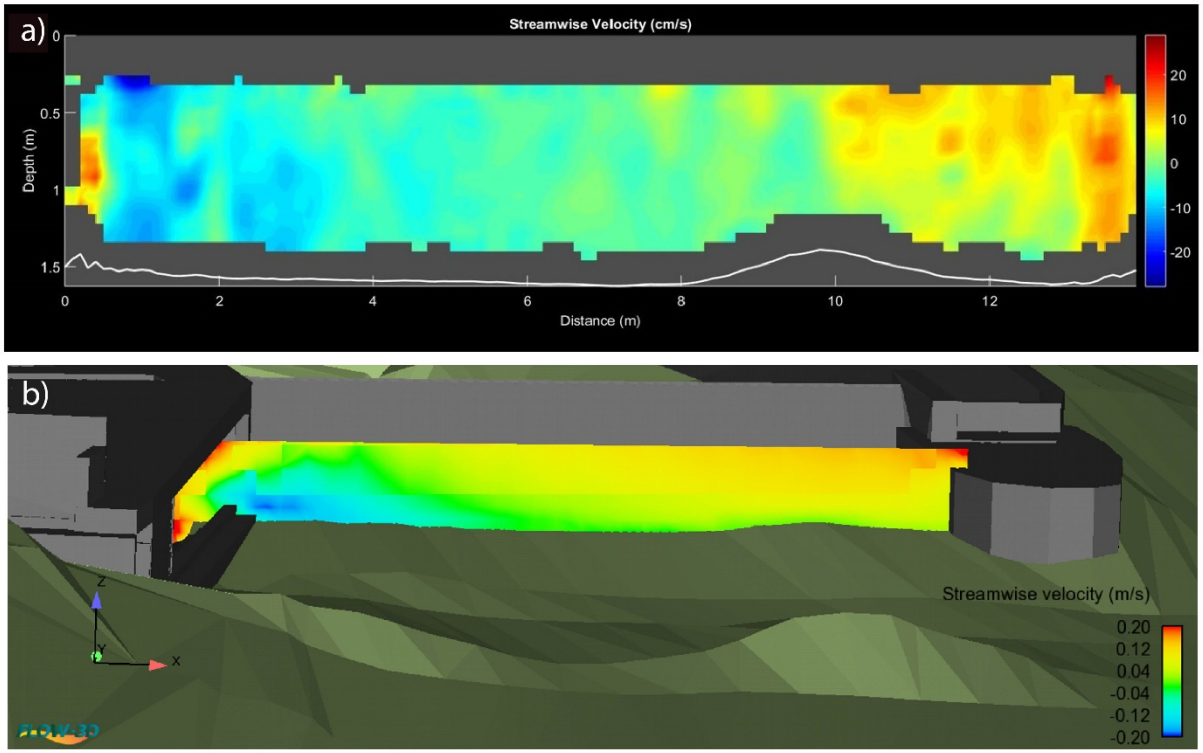

Figure 57: Streamwise velocity distribution from ADCP measurements (a) and numerical model (b) at cross section 7 (see figure 55).

Simulations for improvement of HBR-BS

To improve the fish downstream migration through the HBR-BS at HPP Schiffmühle, four different alternative bypass systems were designed and numerically modelled. This part of the study was funded by the Swiss Federal Office for Energy (SFOE) (contract number: SI/501759-01, https://www.aramis.admin.ch/Grunddaten/?ProjectID=41588).

Four variants were developed based on the bypass design of the residual HPP in Rüchlig in Switzerland, but with smaller dimensions since the design discharge is much lower at HPP Schiffmühle compared to HPP Rüchlig. All variants of the bypass include a separation wall at the left-hand side of the weir, which generates a bypass channel (approximate width of 0.5 m).

The first variant includes a vertical-axis bypass gate with top and bottom openings placed 2 m downstream of the new bypass channel inlet (Figure 58a). The gate can be fully opened to flush driftwood and floating debris when the cleaning machine works. Moreover, the weir was modified with a 0.20 m deep and 0.50 m wide top opening to bypass fish downstream of the weir. The second variant does not include such a gate and hence makes the design even simpler. In this case, the end weir includes a top and a bottom opening to bypass fish downstream (Figure 58b). Third variant has no gate but a 15° inclined ramp in the bypass channel reaching to the weir, which has a 0.50 m wide and 0.33 m high top opening to guide fish to the residual flow reach (Figure 59a). The fourth variant is similar to the third one with a vertical-axis bypass gate placed 1 m downstream of the new bypass channel inlet. The gate have two openings of 0.30 m by 0.30 m at the top and bottom near the wall side (Figure 59b).

Flow fields of all modelled variants were numerically simulated for the river discharge of $Q_r = 125$ m^3/s, the turbine discharge of $Q_t = 14$ m^3/s for the residual flow HPP, the fish pass discharge of $Q_f = 0.50$ m^3/s and the bypass discharge of $Q_b \approx 0.170$ m^3/s.

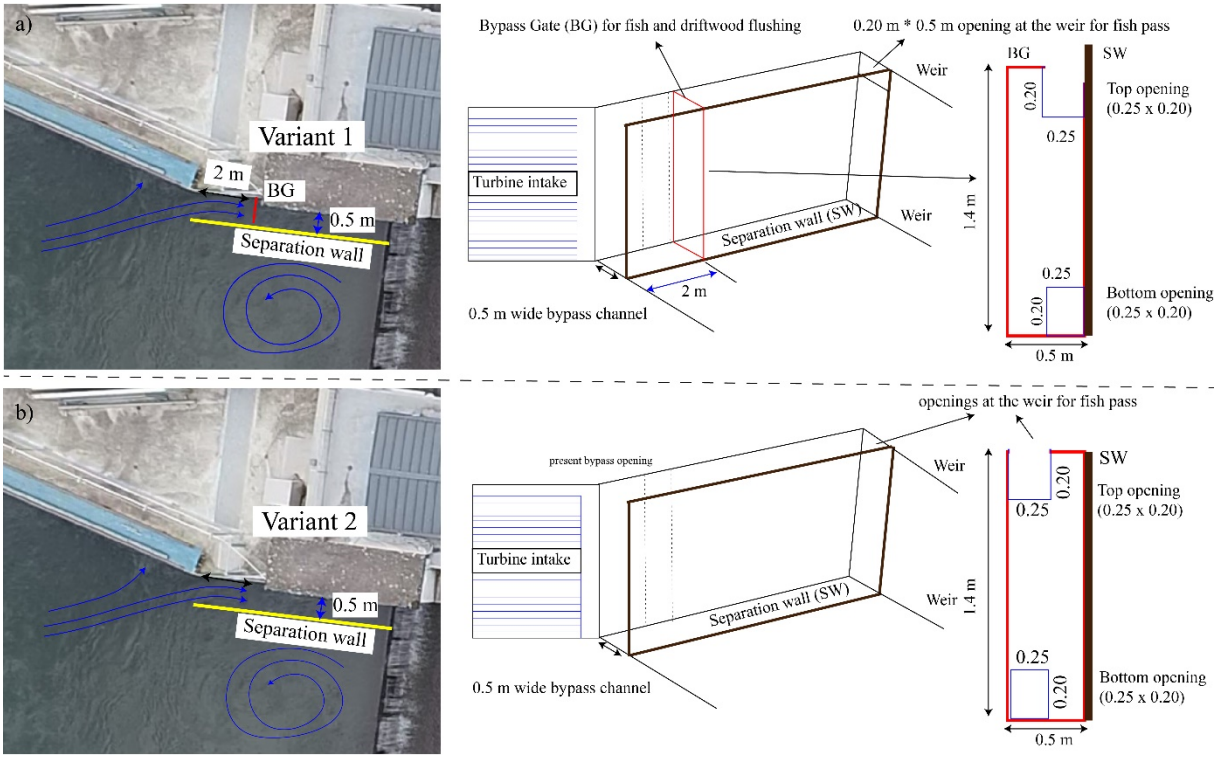

Figure 58: New bypass designs to improve HBR-BS at Schiffmühle HPP: variant 1 (a) and variant 2 (b).

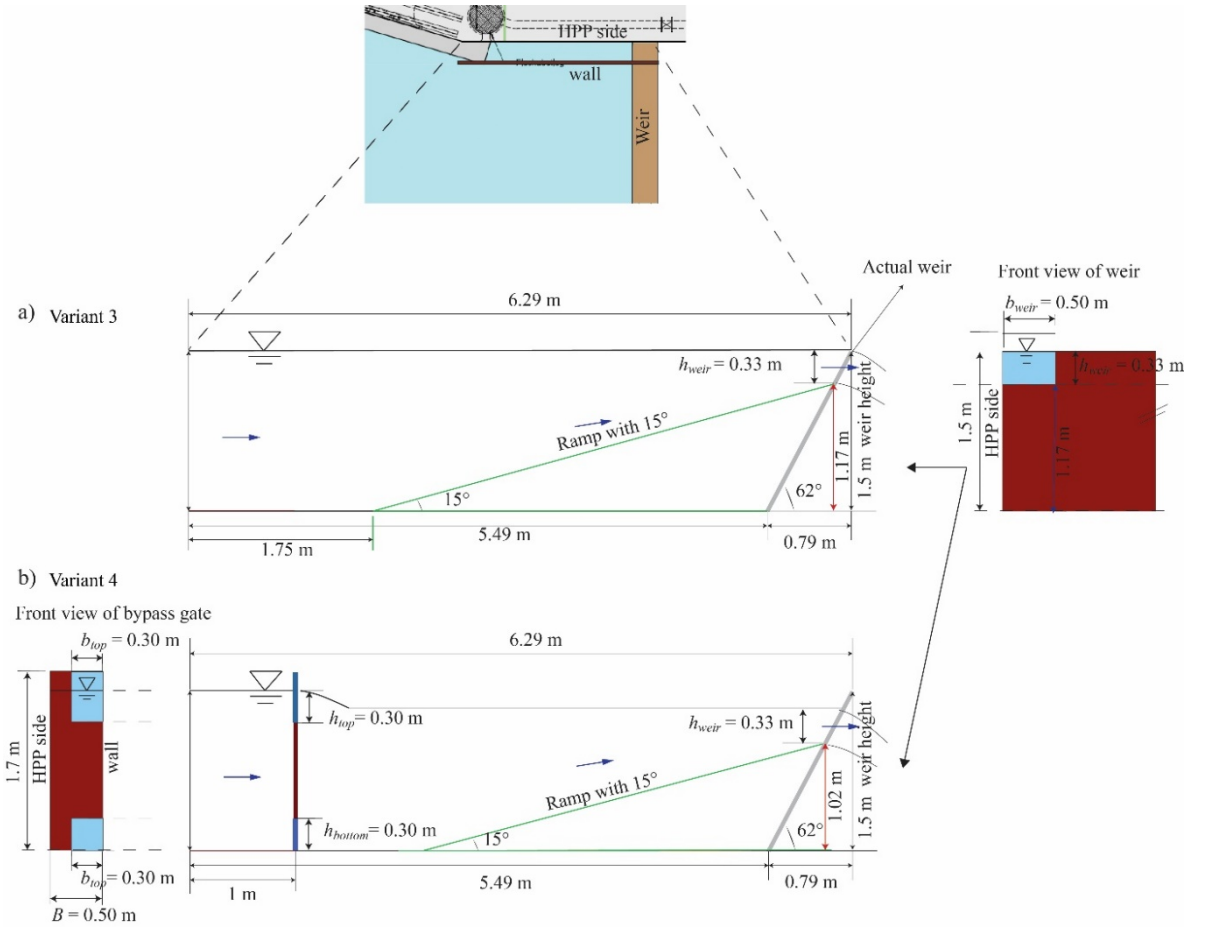

Figure 59:New bypass designs to improve HBR-BS at Schiffmühle HPP: variant 3 (a) and variant 4 (b).

Variant 1

Figure 60a shows the resulting velocity distribution with the streamlines in front of the residual power plant for variant 1. Similar flow structures occur for variant 2 but with different flow structures in the bypass channel (see below for the variant 2 section). With the new bypass design, the large return flow shown in Figure 53 is broken into two smaller counter-rotating vortices. Furthermore, a part of the flow going through the turbine is diverted to the new bypass channel. Figure 60b shows the strong flow divergence towards to the entrance of the bypass channel.

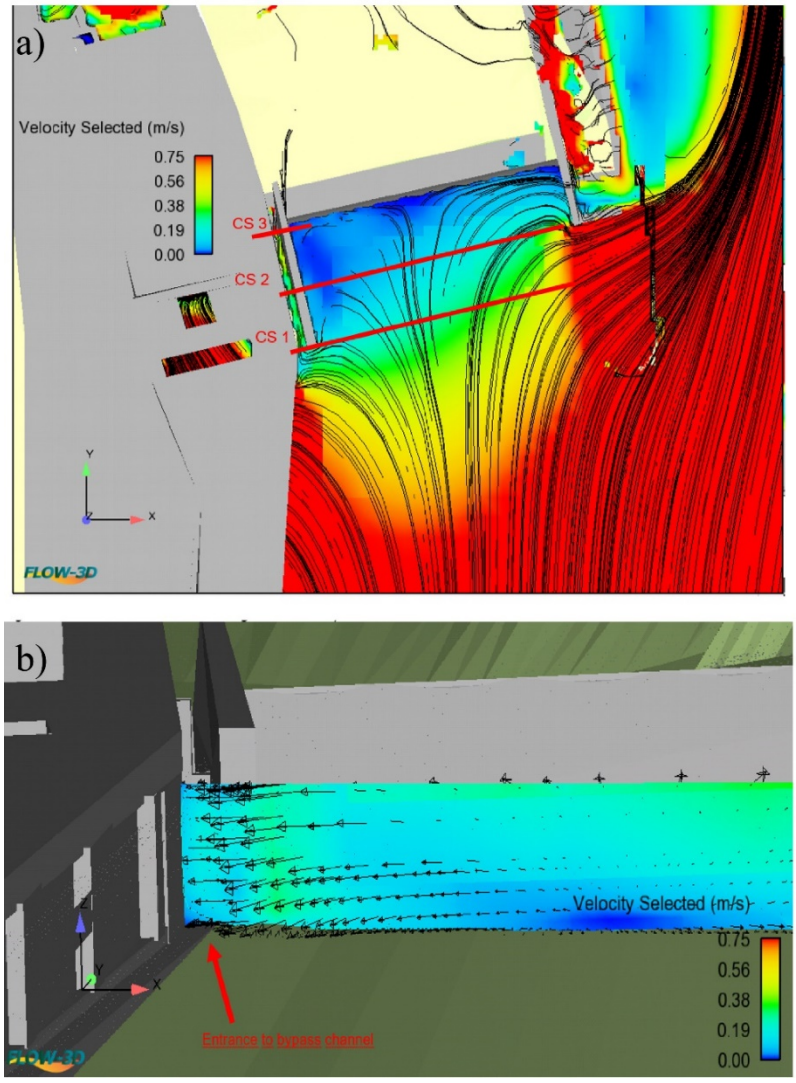

Figure 60: Resulting flow velocity distribution with streamlines for (a) variant 1 (and 2) and with 2D velocity vectors at (b) cross-section 1 (CS1).

The velocity normal to the rack, V_n, increases along the HBR and reaches 0.8 m/s near the bypass entrance before decreasing to around zero (Figure 61a and b). On the contrary, the velocity component parallel to the rack, V_p, decreases from the beginning of the turbine intake towards the bypass entrance (Figure 50c). V_p / V_n >1 at the left-hand side half of the turbine intake, indicating a good fish guidance (Courret and Larinier, 2008). However, along the right-hand side half of the turbine intake, this ratio reduces below 1, indicating a poor fish guidance (Figure 61c and d). Between the turbine intake and the bypass inlet this ratio becomes negative indicating fish guidance towards the intake (Figure 61d). From the turbine inlet along the bypass channel, V_p increases up to 0.60 m/s at the top opening of the bypass gate and then reduces to the top opening at the weir (Figure 61d). Such flow conditions at the inlet and inside of the bypass channel are more favourable for fish compared to the current bypass flow conditions

with low flow velocities at the inlet of the bypass and a large circulation zone between the bypass and weir.

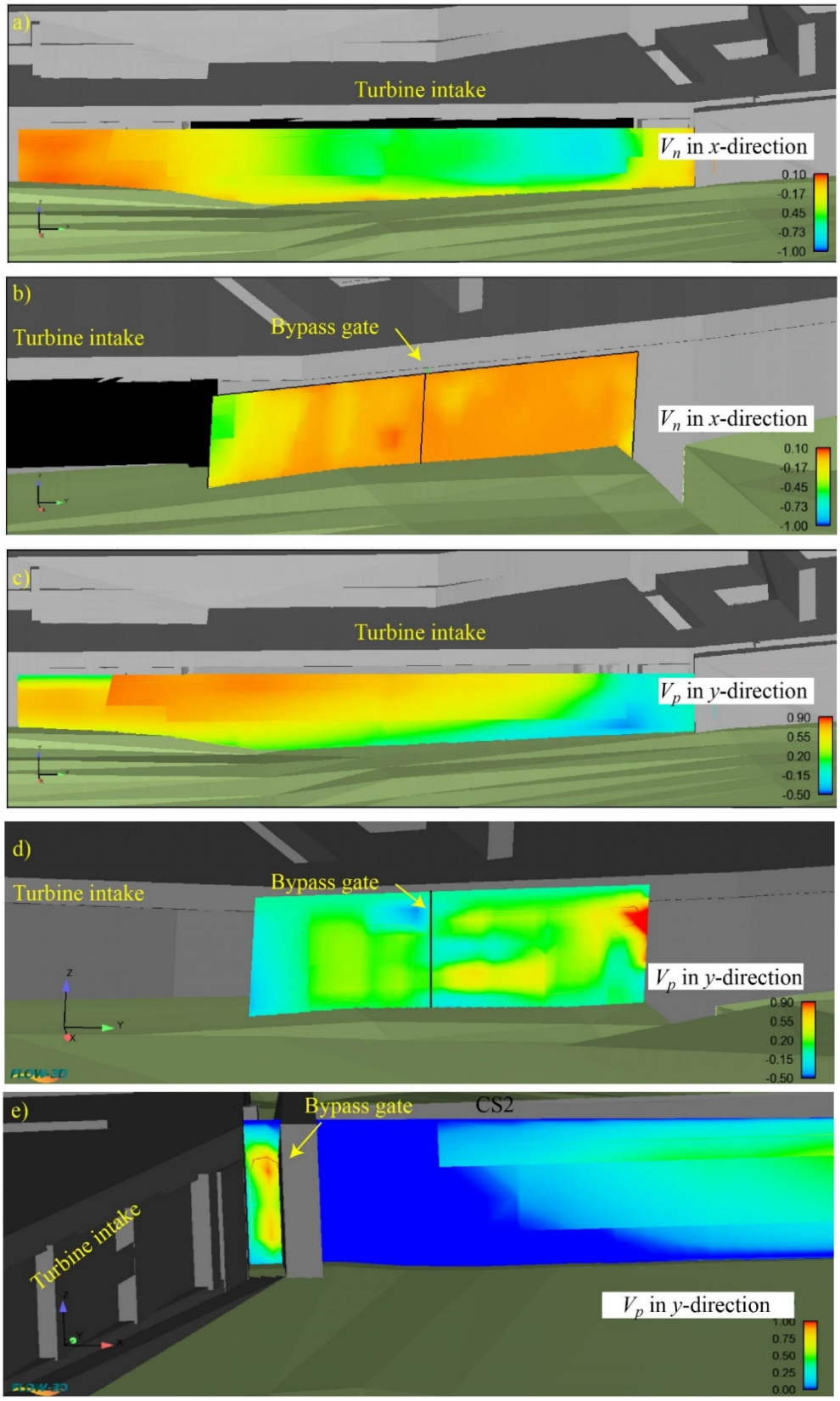

Figure 61: Distribution of normal velocities V_n, along the turbine intake (a) and the bypass channel (b), parallel velocities V_p along the turbine intake (c) and the bypass channel (d) and V_p at the bypass inlet (e) for variant 1.

Variant 2

Figure 62 shows the velocity fields for variant 2. Both normal and parallel velocity distributions in front of the turbine intake are similar to variant 1 (Figure 62a and c) while both velocity distributions deviate from variant 1 inside the bypass due to the lack of the bypass gate at the inlet of the bypass (Figure 62b and d). Only between the turbine intake and the bypass channel inlet, the flow conditions are not favourable to attract the fish towards the bypass. Despite this, V_p / V_n > 1, increasing towards the bypass openings at the weir, indicating a good fish guidance (Figure 62b, d and e). Overall, variant 1 and 2 show better results compared to the current bypass conditions.

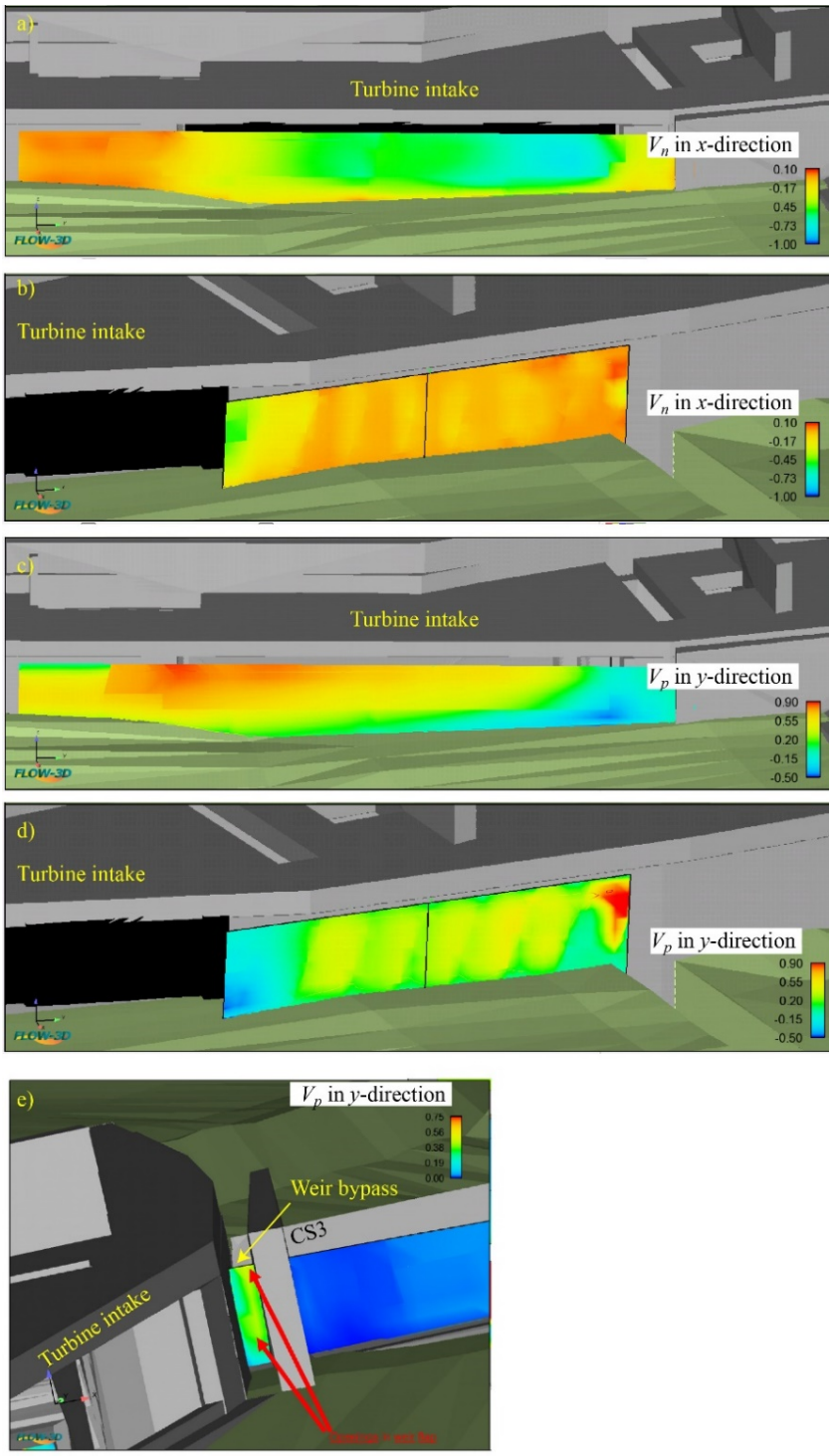

Figure 62: Distribution of normal velocities V_n, along the turbine intake (a) and the bypass channel (b), parallel velocities V_p along the turbine intake (c) and the bypass channel (d) and V_p at the bypass inlet (e) for variant 2.

Variant 3

Figure 63a shows the resulting velocity distribution with the 2D velocity vectors in front of the residual power plant for variant 3. With the new bypass design, the large return flow shown in Figure 53 is broken into two smaller counter-rotating vortices and a strong flow divergence occurs towards the entrance to the bypass channel. Overall, the flow field is similar to those of variants 1 and 2. Figure 63b shows the spatial velocity gradients (SVG) distribution. SVG is higher than 1 near the end of the HBR where the flow is strongly diverted to the turbine and it is also higher than 1 at the end of the bypass channel near and above the weir opening. At those locations, it is expected that fish may show avoidance behaviour because of high flow accelerations (Beck, 2020).

The velocity component parallel to the rack, V_p, decreases from the beginning of the turbine intake towards the bypass entrance (Figure 64a). On the contrary, the velocity normal to the rack, V_n, increases along the HBR and reaches 0.75 m/s with a circulating flow pattern near the end of the HBR before decreasing to around 0.08 m/s (Figure 64a and b). Since $V_n > V_{sustained} = 0.50$ m/s (Ebel, 2016), fish are expected to entrained into the turbine or impinge on the rack in the high normal velocity zone.

Figure 53c shows that V_p / V_n >1 at the left-hand side half of the turbine intake, indicating a good fish guidance (Courret and Larinier, 2008). However, along the right-hand side half of the turbine intake, this ratio reduces below 1 and even becomes negative near the river bed between the HBR and the bypass inlet, indicating a poor fish guidance (Figure 64c). Spatial velocity gradient distribution (Figure 64d) shows that strong velocity gradients near bed between SVG = 1 and 0.75 whereas the velocity gradient is mild near water surface. SVG is also mild being around 0.25 between the HBR and the bypass inlet showing an unattractive flow pattern for fish to find the bypass (Figure 64).

Distribution of flow quantities along the bypass channel at the centre line (Figure 65a) is shown in Figure 54. From the turbine inlet along the bypass channel, V_p increases from 0.15 m/s up to 0.90 m/s at the top opening at the weir (Figure 65b). The mean flow velocity at the bypass entrance is 0.429 m/s and the bypass discharge is $Q_r = 0.232$ m^3/s. The inflow velocity at the turbine intake is around 0.75 m/s (Figure 63a). The ratio between the bypass to the approach flow velocities (bypass Velocity Ratio = *VR*) is *VR* = 0.429/0.75= 0.57, which is well below the recommended values of 1.2-1.4 by Beck (2020), 1.0-2.0 by Ebel (2016) and 1.1-1.5 by USBR (2006). The normal velocity V_n, is near zero as expected but with some velocity patches with smaller 0.25 m/s flow velocities (Figure 65c). Such patches stem from the low resolution of the numerical model. SVG distribution in the flow direction ranges from 0 to around 1.25 with higher values at the top of the weir opening where hesitation of fish passing the weir is expected (Figure 65d). Compared to the current flow condition, variant 3 creates better flow field but do not satisfy the recommended values of SVG and *VR* (Beck, 2020).

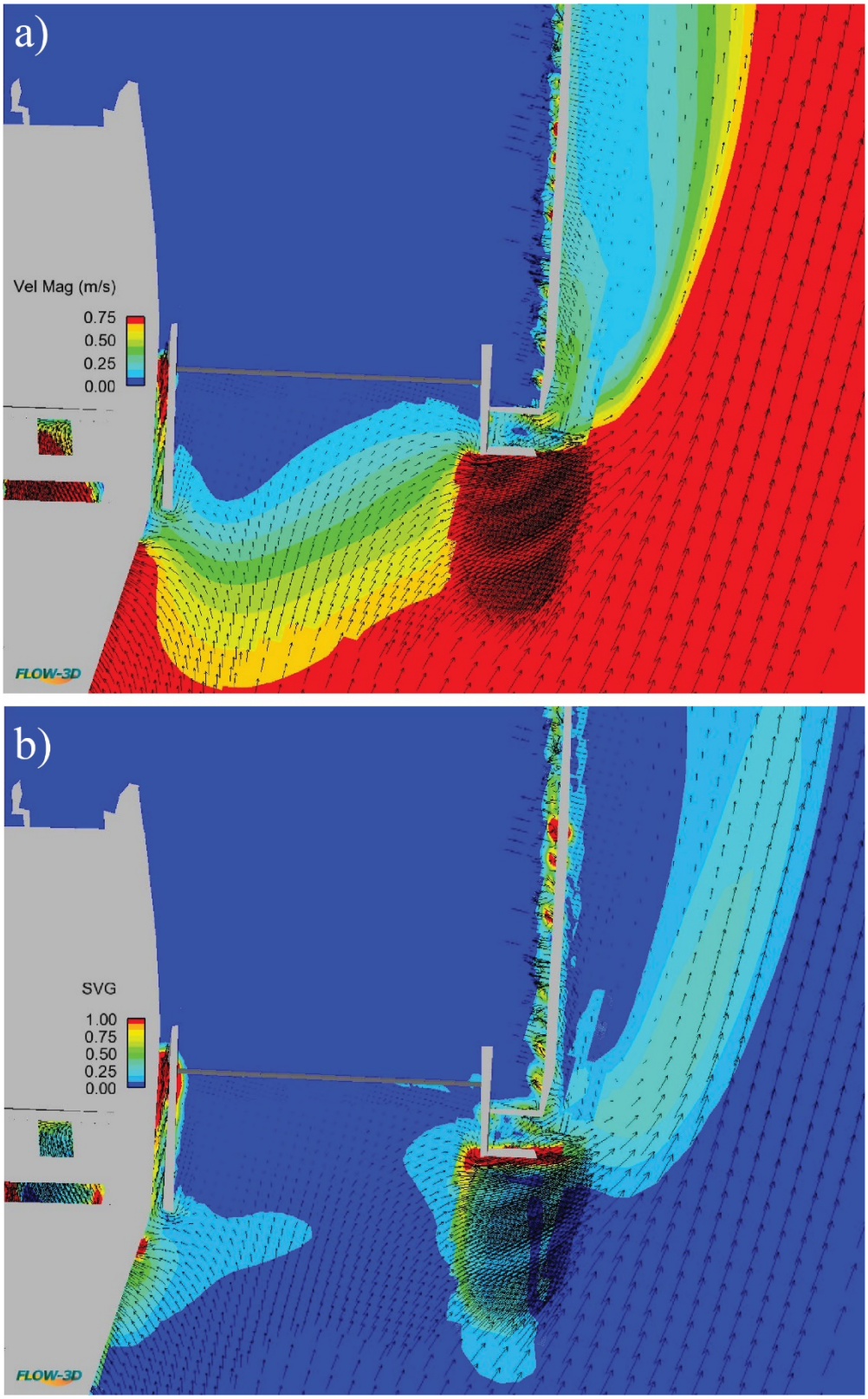

Figure 63: Resulting flow velocity distribution (a) spatial velocity gradient (*SVG*) (b) with 2D velcoity vectors at the horizontal level 0.285 m below the water surface for variant 3.

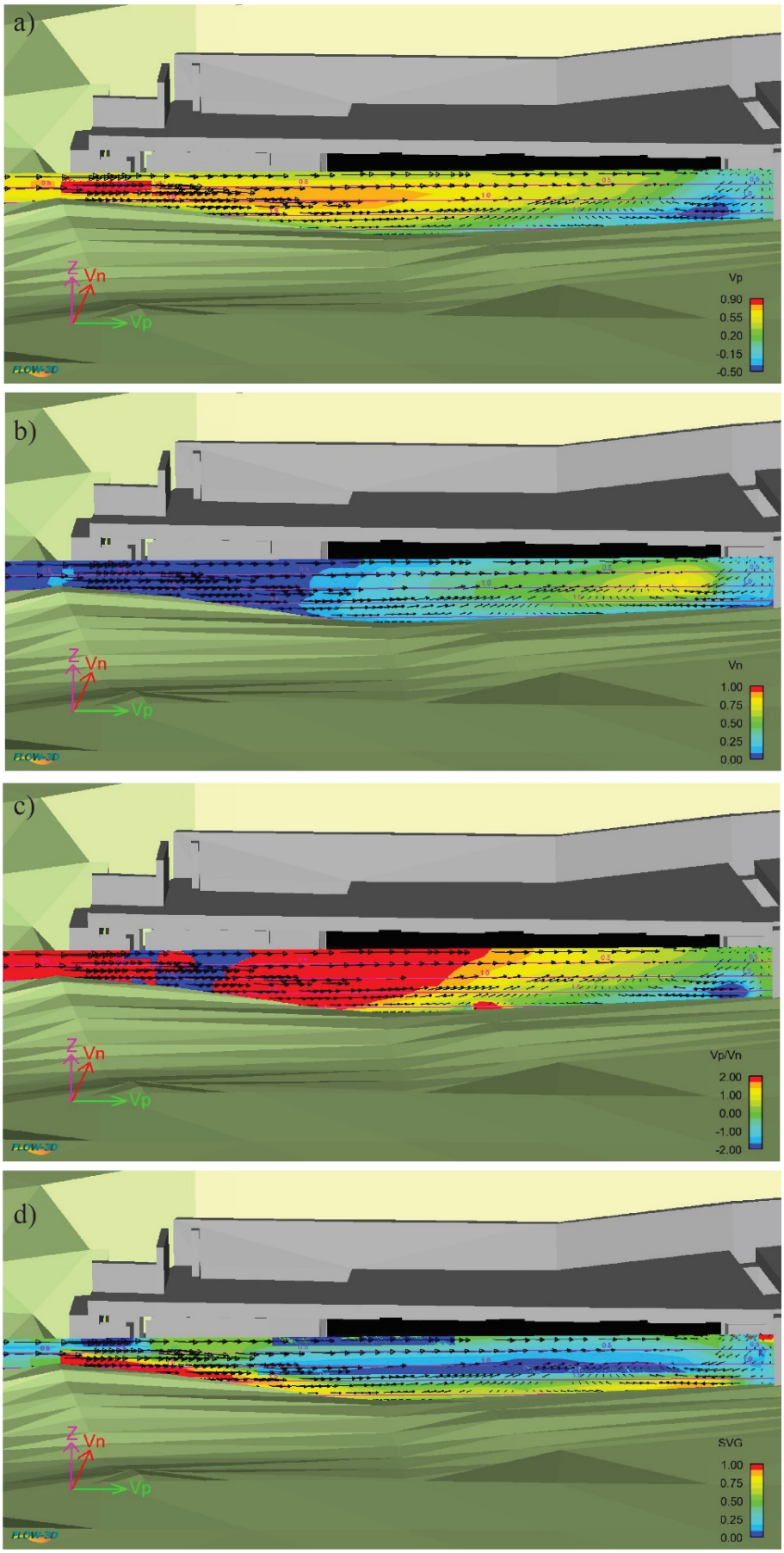

Figure 64: Distribution of parallel V_p (a), normal V_n (b) velocities, V_p / V_n (c) and SVG (d) along the turbine intake for variant 3.

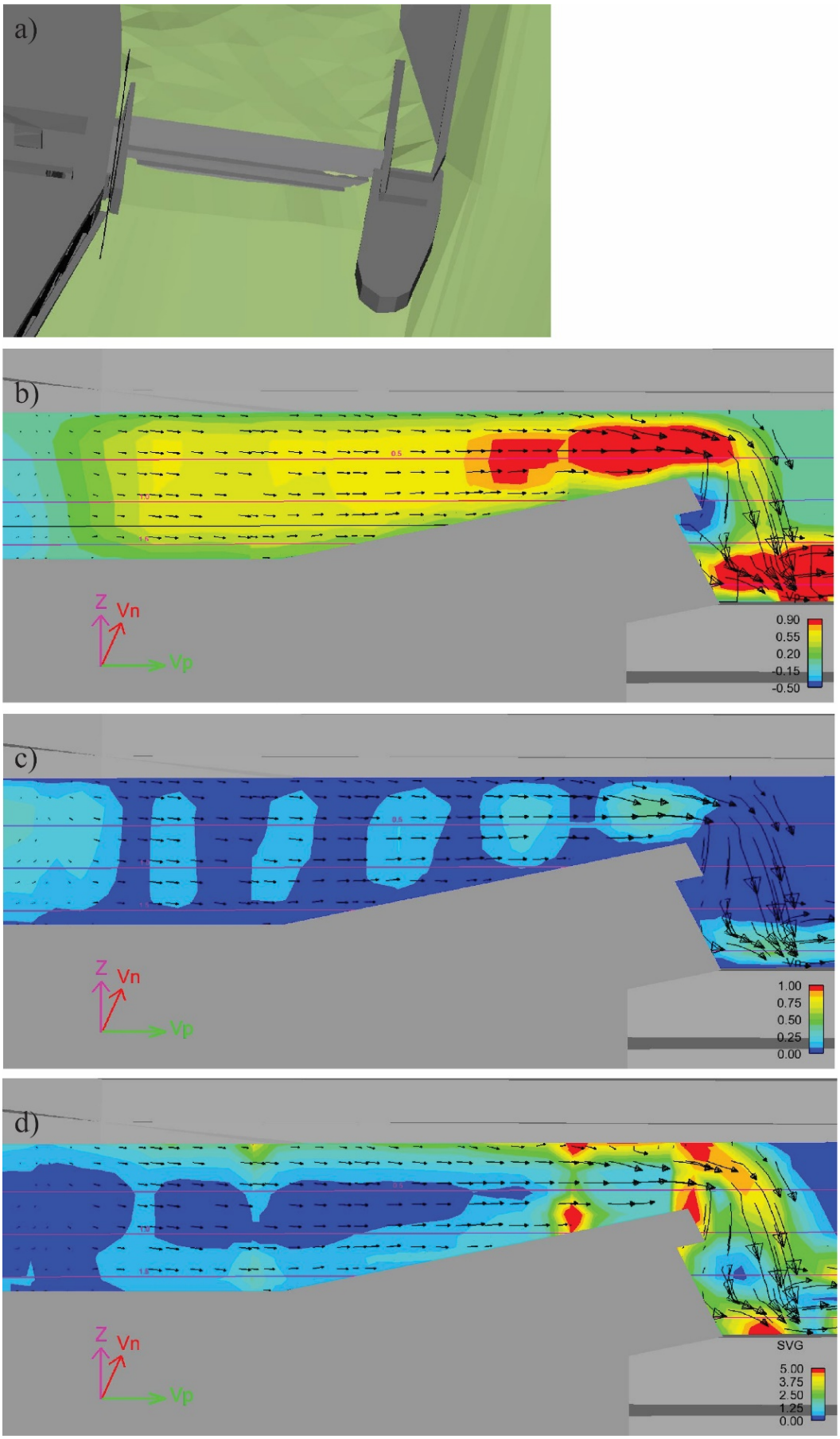

Figure 65: Plane location (a), distribution of parallel V_p (a), normal V_n velocities, V_p /V_n (c) and SVG (d) along the bypass channel for variant 3.

Variant 4

Figure 66a shows the resulting velocity distribution with the 2D velocity vectors in front of the residual power plant for variant 4. Overall, the flow field is similar to those of variants 1, 2 and 3 except near the bypass inlet. At the bypass inlet, the vertical-axis gate causes high flow velocities and acceleration i.e. SVG (Figure 66a and b). After the gate towards the weir top opening, flow velocity and as well as SVG reduce (Figure 66b).

Distribution of parallel V_p, and normal V_n, velocities, their ratio = V_p/V_n and SVG for variant 4 is quasi-similar to variant 3 in the front of the turbine intake (compare Figure 64 with 67). There is an only and slight difference between variant 3 and 4 on the flow field between turbine intake and bypass inlet, which is not visible in Figure 67.

Distribution of flow quantities along the bypass channel at the centre line is shown in Figure 68 for variant 4 and strongly and positively deviate from those for variant 3 (Figure 65) due to effect of the vertical-axis gate. Between the turbine intake and the gate, V_p gradually increases from -0.15 m/s up to 0.90 m/s (Figure 68a). A small part of the flow goes through the bottom opening of the gate while large part of the flow goes through the top opening of gate. The reason for unequal discharge distribution between the top and bottom openings results from the recirculation zone occurring between near the end of the HBR i.e. turbine intake and the gate (Figure 67). The velocity at the top and bottom openings are around 0.90 m/s and 0.30 m/s, respectively (note that these velocities are along the centre axis of the bypass channel). The average flow velocity at the bypass openings are around 1 m/s and the bypass discharge is 0.177 m^3/s. The inflow velocity at the turbine intake is around 0.75 m/s (Figure 66a). The ratio between the bypass to the approach flow velocities is $VR = 1/0.75 = 1.33$, which is in the range of the recommended values of 1.2-1.4 by Beck (2020), 1.0-2.0 by Ebel (2016) and 1.1-1.5 by USBR (2006). The normal velocity V_n, along the bypass channel is near zero as expected but with some velocity patches with smaller 0.25 m/s flow velocities (Figure 68b). SVG distribution in the flow direction increases from 0 to around 1.25 at the top opening and reaches 5 after the top opening. The location of the highest SVG is downstream of the gate and covers an half of the water depth. At this location, fish passing the top opening of the gate has no chance to the return but continue moving over the ramp towards the weir opening. Along the ramp, SVG changes between 0 and 1.25 and becomes roughly between 1.25 and 2.5 over the weir opening (Figure 68c). Compared to the current flow condition and variants 1, 2 and 3, variant 4 creates much better flow field and quasi- satisfy the recommended values of SVG and *VR* and hence we can conclude that variant 4 is the best option with favourable flow conditions for fish bypass.

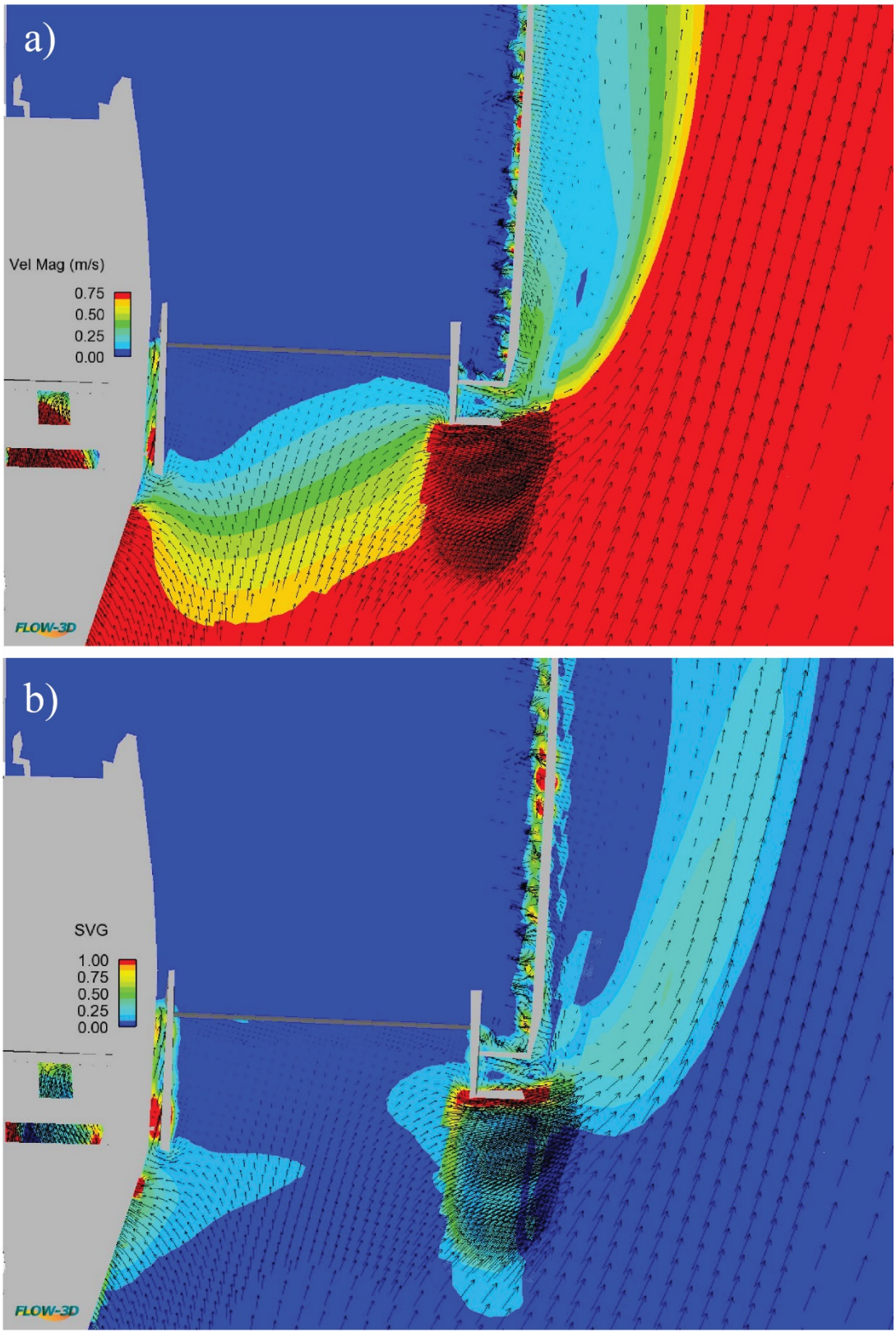

Figure 66: Resulting flow velocity distribution (a) spatial velocity gradient (*SVG*) (b) with 2D velcoity vectors at the horizontal level 0.285 m below the water surface for variant 4.

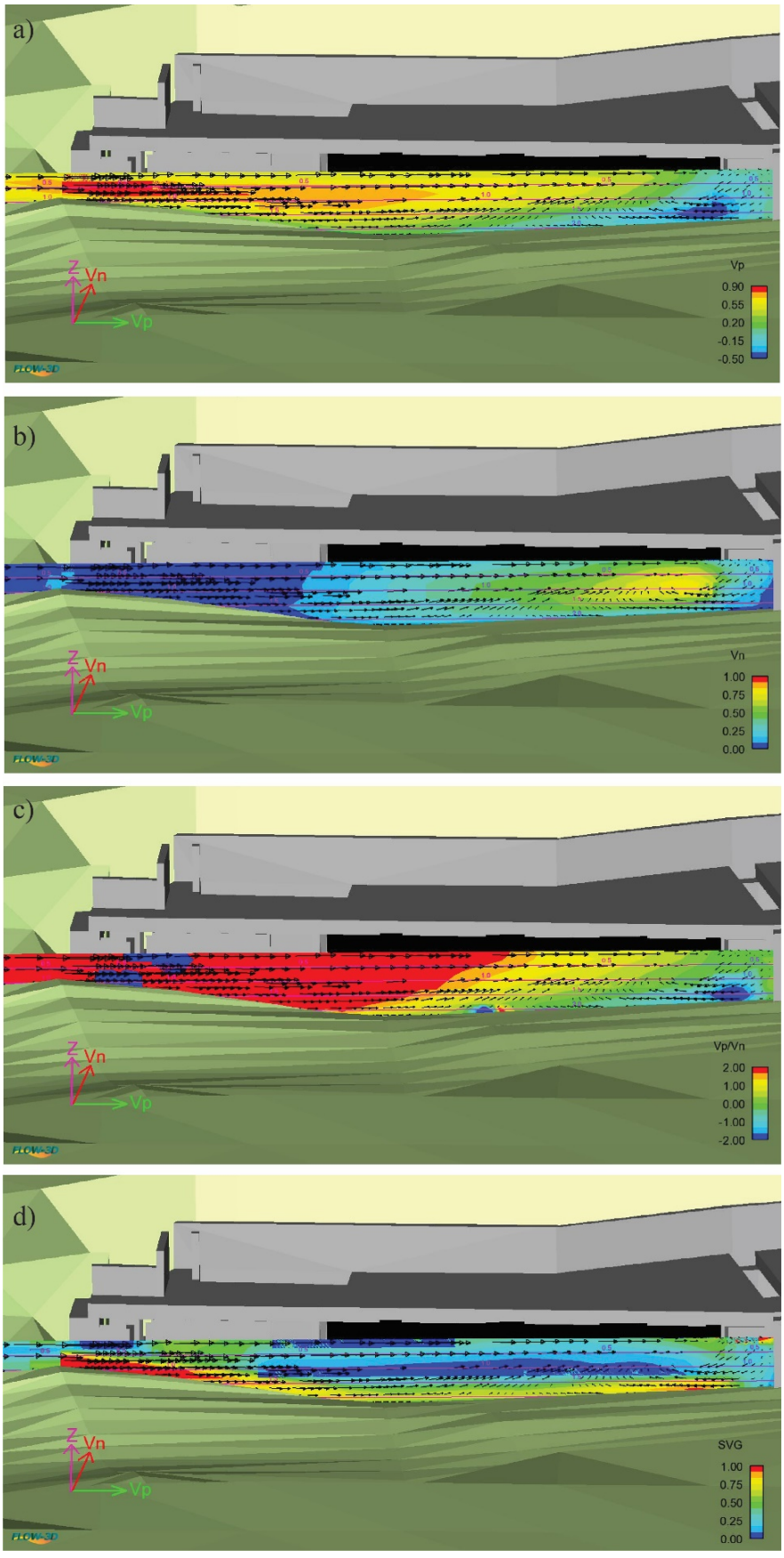

Figure 67: Distribution of parallel V_p (a), normal V_n (b) velocities, V_p / V_n (c) and SVG (d) along the turbine intake for variant 4.

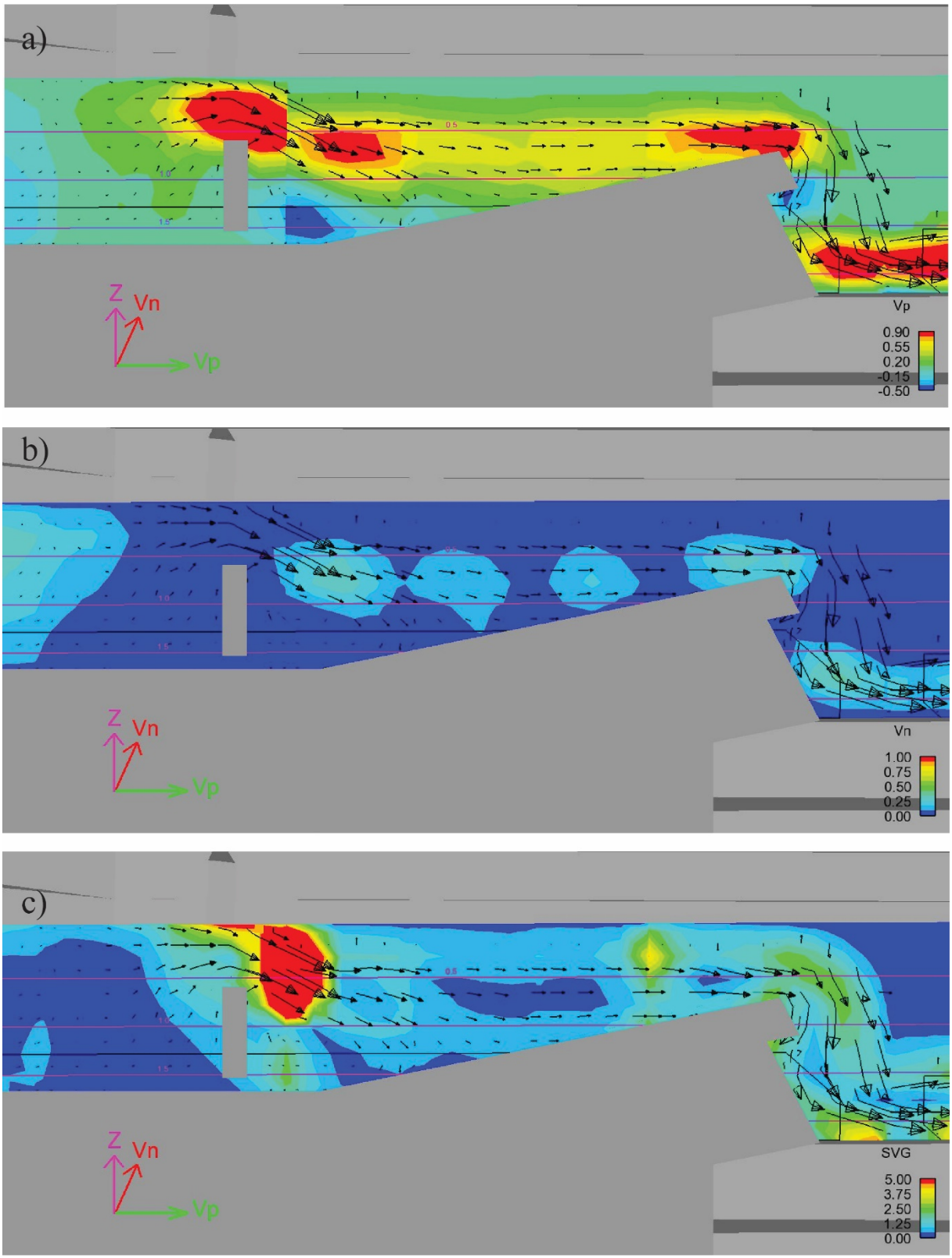

Figure 68: Distribution of parallel V_p (a), normal V_n (c) velocities and SVG (d) along the bypass channel for variant 4.

3.3.3.4 Fish monitoring

3.3.3.4.1 Upstream migration

The lengths of 2890 tagged fish caught in the counting facilities at the fish pass ranged from 82 to 900 mm (median 130 mm) (Figure 69). Between 28 September 2017 and February 2020 hundreds of thousands detections were registered at the installed antennas. Figure 69 shows the length distribution of each fish species detected at different locations i.e. Vertical Slot Fish Pass (VSFP), Nature-Like Fish Pass (NLFP). An overview of the detected fishes in VSFP, NLFP and unknown path of fish accent is presented in table 2. 1'946 of the tagged fishes (67.3 % of total number of tagged fish) were detected. This is considered as a high rate. 1'858 tagged fish (95.5 %) entered the fish ladder and 81.4 % of them successfully ascended the fish pass. Barbel preferred the entrance of the VSFP, while chub, roach and especially dace preferred to enter the NLFP (see table 12).

The attraction efficiency is defined as a ratio between the number of the fish registered at the first antenna of the fish pass entrance and the number of the tagged and released fish. It differs between the species but is always in the range between 60 – 90 % (except species with only a few individuals). Bleak do not have a specific preference for one of the two entrances into the ladder, however, dace showed a high preference for the NLFP (79.3 % of the individuals). Roach showed also a preference for the NLFP (69.1 % of the individuals). Chub and perch had a lower, but still a clear preference for the same entrance. Mainly the barbel preferred the entrance into the VSFP with 42.3 % of the individuals compared to only 24.3 % of the individuals in the NLFP. Spirlin seem to have the same preference. The total passage efficiency for all tagged fish in the counting facility is high (81.4 %). The total (whole fish ladder) attraction efficiency is 67.3 % which is considered to be good to high. The total attraction efficiency for fishes caught in the forebay is 78 % and therefore higher (Table 12).

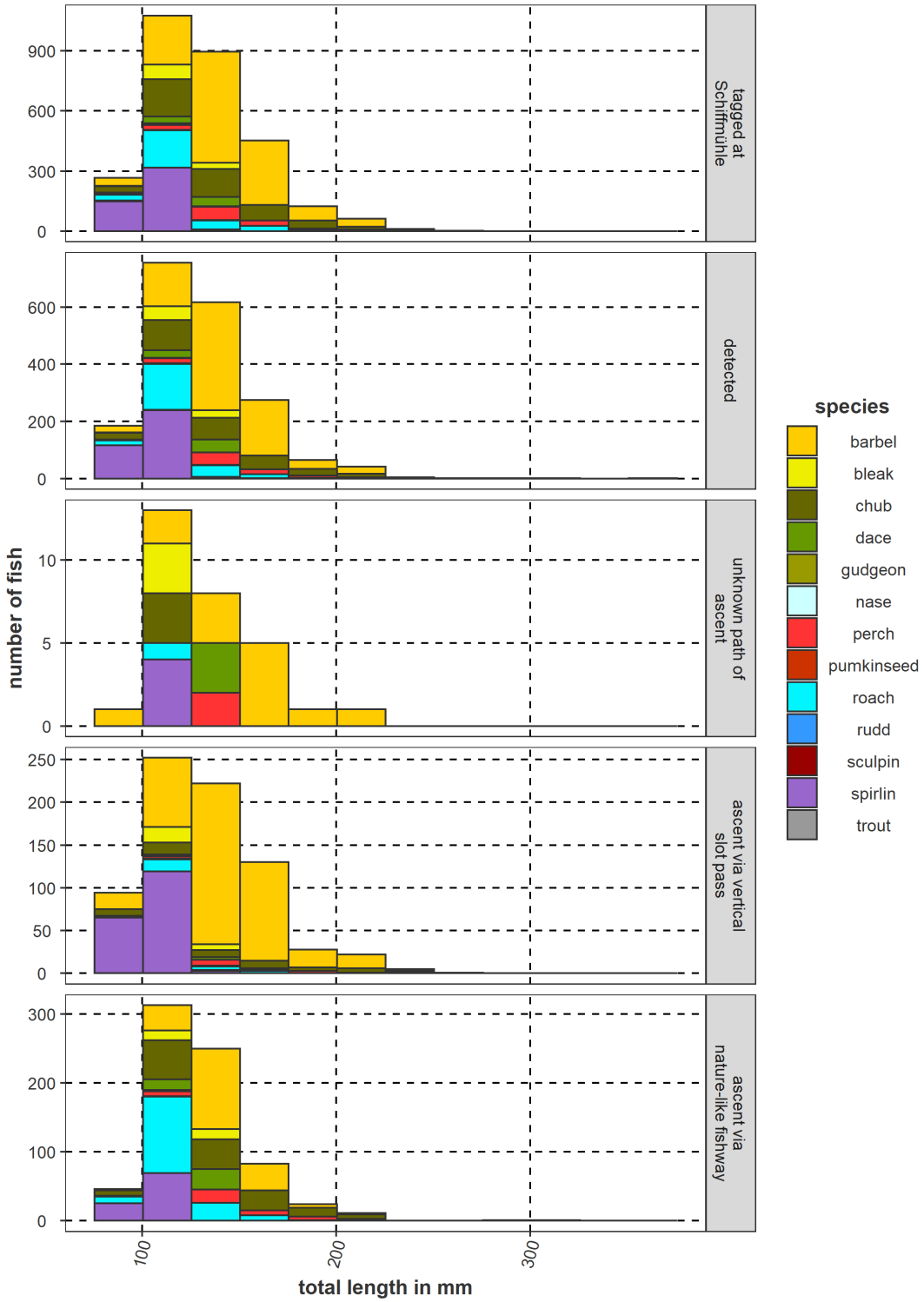

Figure 69: Total length of tagged fishes caught in the counting facilities (N=2’890) belonging to 13 fish species.

Table 12: Monitoring results of fishes caught in the counting facilities. VSFP= vertical slot fish pass, NLFP=nature-like fish pass

species	N tagged	N detected	N entered	Unknown path of ascent	Acscended in the vertical slot pass	Ascended in the nature-like fish ladder	Attraction efficiency of VSFP in %	Entrance efficiency of VSFP in %	Passage efficiency of VSFP in %	Attraction efficiency of NLFP in %	Entrance efficiency of NLFP in %	Passage efficiency of NLFP in %	Attraction efficiency of whole fishpass in %	Entrance efficiency of whole fishpass in %	Passage efficiency of whole fishpass in %
chub	496	292	281	3	50	158	14.3	100	70.4	50.8	90.9	69	58.9	96.2	75.1
Brown trout	2	2	1	0	1	0	50	100	100	50	0	-	100	50	100
barbel	1278	806	777	13	442	202	42.3	97.8	83.6	24.3	84.2	77.4	63.1	96.4	84.6
perch	134	90	88	2	17	41	23.1	100	54.8	50.7	95.6	63.1	67.2	97.8	68.2
bullhead	3	0	0	0	0	0	0	-	-	0	-	-	0	-	0
gudgeon	16	1	0	0	0	0	0	-	-	6.2	0	-	6.2	0	0
dace	82	73	64	3	6	46	9.8	100	75	79.3	84.6	83.6	89	87.7	85.9
bleak	105	76	74	3	25	29	35.2	100	67.6	40	90.5	76.3	72.4	97.4	77
nase	5	3	2	0	0	2	0	-	-	60	66.7	100	60	66.7	100
roach	291	237	213	1	23	156	16.2	100	48.9	69.1	87.6	88.6	81.4	89.9	84.5
rudd	3	2	1	0	1	0	33.3	100	100	33.3	0	-	66.7	50	100
spirlin	472	361	354	4	187	94	49.8	99.1	80.3	38.3	90.1	57.7	76.5	98.1	80.5
pumpkinseed	3	3	3	0	2	1	100	66.7	100	33.3	100	100	100	100	100
Total	2890	1946	1858	29	754	729	33.7	98.5	78.5	39	87.9	73.6	67.3	95.5	81.4

Passage duration: The values of the median in the VSFP (Table 13) are very meaningful. For most of the fish species at least 50 % of the individuals had a passage duration of less than 60 minutes. The passage duration in the NLFP is a little bit longer than in the VSFP (Tables 13, 14). The values of the median increased by 24.8 minutes (species without spirlin). The passage duration of spirlin was 502.8 minutes. The spirlin remained for a long time in the NLFP. However, the fastest spirlin passed within 36.4 minutes which can be interpreted that spirlin were not restricted in the passage possibility.

Table 13: duration of passage (in minutes) from the last registration at the lowest antenna in the VSFP until the upper antenna at the exit of the fish pass.

species	average	median	minimum	maximum	N
eel	76.1	76.1	76.1	76.1	1
chub	77.5	38.0	15.0	927.4	53
Brown trout	29.4	29.4	29.4	29.4	1
barbel	217.9	62.6	12.2	28809.0	434
perch	71.4	59.8	19.6	217.9	17
dace	33.2	29.0	14.2	67.0	6
bleak	70.4	42.3	18.0	580.8	24
roach	61.5	42.4	16.0	429.5	23
rudd	52.8	52.8	52.8	52.8	1
spirlin	1549.6	136.7	15.0	53952.9	179
pumpkinseed	759.9	759.9	106.4	1413.4	2

Table 14: duration of passage (in minutes) from the last registration at the lowest antenna in the NLFP until the upper antenna at the exit of the fish pass

species	average	median	minimum	maximum	N
chub	191.1	56.8	6.4	7844.3	182
barbel	252.5	97.4	24.5	8406.1	196
perch	225.9	88.7	31.0	926.6	33
dace	56.0	47.8	22.4	211.3	47
bleak	109.1	62.9	22.2	764.0	27
nase	290.0	290.0	96.3	483.6	2
roach	117.6	69.2	27.6	1408.3	148
spirlin	1225.8	639.5	36.4	21518.8	77
pumpkinseed	88.4	88.4	88.4	88.4	1

In conclusion, the detection rate and attraction efficiency at Schiffmühle is quite high. In other studies, lower attraction efficiencies were found. Benitez et al. (2018) found in Belgium a value of 32.9 %. Peter et al. (2016) reported values up to 30 % at the HPP Rheinfelden in the Rhine River. However, Bunt et al. (2012) found average attraction efficiencies of 66 % for different species and different types of fish ladders. Both entrances at Schiffmühle were equally used and entrance efficiencies were high for both types. But there was a difference between species in the preference of the fishpass type. The entrance efficiency was higher in the vertical slot pass. The passage efficiencies for the whole fish ladder is very high (81.4 %). Bunt et al. (2012) reported a passage efficiency of 45 % for VSFPs and 70 % for NLFPs. The duration of passage is less than 60 minutes for most of the species. This passage can be classified as fast. No length selectivity was observed. In summary, both fish passes (VSFP & NLFP) at Schiffmühle is assessed to be functional. All the parameters can be characterized as good or very good. The two entrances complement one another; both are preferred by different species. However, the attraction efficiency could not be tested for salmonids.

3.3.3.4.2 Downstream migration

During the whole study period (29 months) only 2 individuals used the Bypass System (BS) of Horizontal Bar Rack (HBR) installed at the residual flow HPP Schiffmühle: one barbel with a total length of 151 mm and one spirlin with 96 mm. However, other downstream corridors were used more often.

A total of 445 downstream movements were observed. 265 unknown descents were detected corresponding to 60% of the total number of the downstream moving fish (445) (Table 15). These fish were using the side weir along the headrace canal, the weir next the residual flow HPP or the turbines of the main or residual flow HPP as a downstream migration corridor. They were later again detected on the antennas in the fish passes, indicating that they were survived from the unknown decent paths. 178 fish (40%) used the fish passes for downstream movement. The VSFP had a double downstream migration frequency compared to the NLFP.

Overall, the BS of the HBR for the downstream migration is not functional. Fish should be guided to enter the bypass by the 20 mm HBR. On the one hand, the pipe of the BS is often clogged with woody debris. On the other hand, flow field is not favourable between the HBR and the BS entrance and from there to the entrance of the bypass pipe. In addition, the velocity increase in the bypass pipe is very high. Therefore, the bypass can be regarded to have no function for downstream migrating fish. From the

ecological point of view, it is questionable if there has to be a functional bypass into the residual flow section. However, it is very important that a downstream fish protection and guidance system will be built at the main HPP (see the conclusion section below).

Table 15: Origin of down migrated fishes. Some individuals were counted different times if they used several corridors or the same corridor more than once

	HPP upstream of Schiffmühle	Schiffmühle forebay	Schiffmühle tailrace	Schiffmühle counting facility	Total
Descent in the bypass	0	0	0	2	**2**
Descent in nature-like fishway	0	1	0	55	**56**
Descent vertical slot pass	0	1	1	120	**122**
Unknown descent	4	6	10	245	**265**
Total	**4**	**8**	**11**	**422**	**445**

3.3.4 Conclusions & Outlook

We documented the current situation and evaluated the hydraulics and fish guidance efficiency of a Horizontal Bar Rack-Bypass System (HBR-BS) installed at the residual HPP Schiffmühle by conducting velocity measurements, fish monitoring and numerical modelling.

The monitoring comprise:

- characterization of the flow field and river bathymetry using ADCP
- 3D numerical simulation
- survey of the fish movements using PIT-tagging technique

High-resolution 3D velocity as well as bathymetry measurements were conducted using an Acoustic Doppler Current Profiler (ADCP) mounted on a high-speed remote control boat in March and October 2018. The bathymetry and velocity data were analyzed in-depth and provided to our partner AF-Consult for numerical modelling of the HPP. Based on these, AFRY (former AF-Consult) set-up, calibrated and validated a 3D numerical model. Since the hydraulic conditions at the bypass were not favorable, four variants of new bypass systems were modelled and their hydraulic conditions were simulated. Peter Fish Consulting (FCO) conducted fish monitoring at the HBR-BS and both at a technical and nature-like fish passes by PIT-tagging more than 3000 fish belonging to 13 different fish species. The key results of these works include:

1) ADCP velocity measurements indicate that most fish in the river are expected to follow the main current towards the headrace channel, while a small portion swims towards the residual flow HPP.
2) The attraction flow to the bypass for downstream migration seems inefficient and a re-circulation zone possibly affects fish searching and finding the bypass entrance.
3) 2 fish out of 445 was detected in the bypass pipe, confirming the poor velocity field around the bypass.

4) Clogging of the bypass pipe is a problem affecting the bypass discharge and velocity.
5) 178 fish out of 445 (40%) were detected in the fish pass, indicating that the hydraulic conditions at the exit and along the fish pass are attractive and favorable enough to guide fish downstream, presenting an alternative downstream passage route for fish.
6) 265 fish out of 445 (60%) used either the weir or turbines of the residual flow or main HPP powerhouse, indicating 100% survival rate independent of these routes.
7) The present downstream bypass system needs optimization.
8) Four variants of new bypass systems as an alternative to the present one were developed and 3D numerically modelled.
9) Variant 4 with a vertical-axis gate with top and bottom openings and a 15° inclined ramp between the gate and weir show the best flow conditions compared to the other three variants and would likely improve the fish guidance efficiency of the HBR.
10) Alternatively, an effective fish protection and guidance system such as HBR-BS or newly developed Curved-Bar Rack-Bypass System (CBR-BS, Beck 2019 and 2020; Beck et al. 2020a and b) should be realized at the main HPP of Schiffmühle instead of making an effort to improve the current HBR-BS at the residual HPP because most fish in the river are expected to follow the main flow towards the headrace channel.
11) Both vertical slot and nature-like fish passes at HPP Schiffmühle function well for upstream moving fish with attractiveness, entrance and passage efficiencies.

The above-listed findings of the present study at HPP Schiffmühle indicate that design, location and operation of a bypass system are of prime importance for a successful implementation and high fish guidance efficiency of HBR-BS. Furthermore, these findings have a wide range of applications for other similarly sized HPPs and will serve as a basis for an optimal design of HBR-BS.

As an outlook, we recommend to improve the existing downstream migration facility followed by an additional tagging campaign confirming the function of the downstream migration. This could be done by an additional video, PIT-tagging analysis or radio telemetry technique. Furthermore, a high resolution 3D model of the studied alternative bypass system with improved geometry and more numerical simulations for various discharge scenarios are recommended to obtain a final bypass design. We also recommend to consider implementing an effective fish protection and guidance system such as HBR-BS or newly developed CBR-BS at the main HPP of Schiffmühle.

3.4 Habitat modelling (SJE, TUT)

The attraction flow from the fish pass outlets will be investigated with the habitat simulation system CASiMiR. A Lateral Line Probe (LLP) will be used to study fish habitats and potential migration pathways using machine learning algorithms which are based on a spectral analysis of the recorded narrowband pressure fields. The results from LLP and CASiMiR will be compared.

To characterize the relationship between the local hydrodynamic conditions in the fishway outlet flow ("attraction flow") and the spatial distribution of local flow variables, an artificial lateral line probe (LLP) as well as an acoustic Doppler velocimeter (ADV) are used and are shown in Figure 70. The use of the ADV provides velocity data comparable to available studies on attraction flows, and the use of a LLP provides body-oriented differential pressure fluctuations in order to explore the additional data gained using the lateral line probe (higher sampling rate and distributed sensing). Compared to point velocity measurements delivered by ADV, LLP captures the physical metrics (body-oriented pressure gradients) which may be closer to the "fish's perspective".

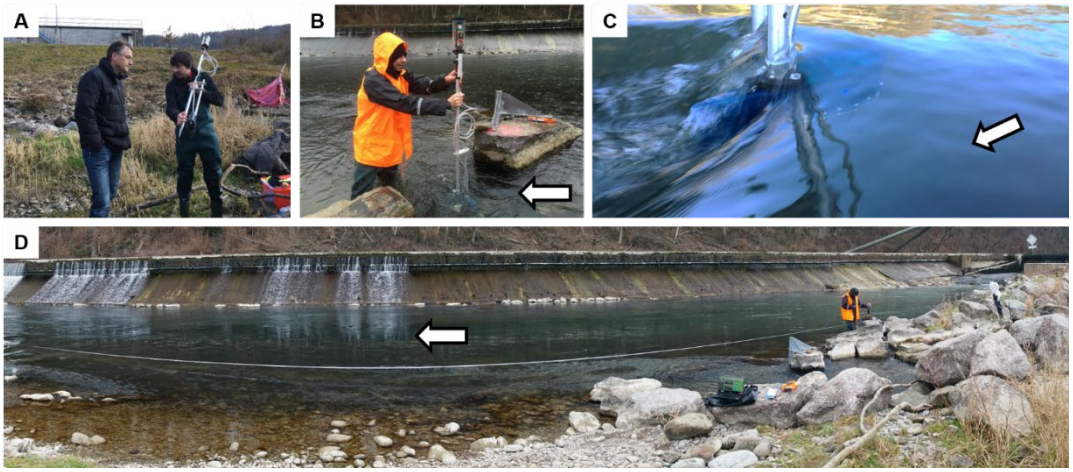

Figure 70: A) Lateral line probe can be used easily, and requires a short field training. B) The LLP measurements can be made directly in the attraction flow jet. C) Close-up view of the LLP near the top of the water column, illustrating the water flow around the probe body. D) A measuring tape extended in the field along the jet core facilitates reproducible measurement locations for future studies using ADV or LLP.

3.3.1 Data

Data are collected as pressure time series from the ADV (velocity U,V,W) and LLP (differential pressure sensor readings, water temperature, water depth). All data files are stored on a secured server and shared with FITHydro project partners as required in the consortium agreement.

3.3.2 Methodology

CASiMiR and LLP

The results of the bathymetric and hydrodynamic model are the basis for the analysis of fish migration; yet they are currently not available (as of January 2019). The telemetric investigations in the test case Schiffmühle do not deliver tracks of fish approaching the fish pass, but the fish entering and leaving the fish pass are counted. Thus, it is not possible to use the telemetric data for the development of CASiMiR migration which aims on the assessment of attraction flow. The test case Schiffmühle will instead be used for testing the migration model, which is developed based on data from the test case Altusried, Iller, where fish tracks are available. The intention is to find relations between the flow rates that provide good conditions in terms of attraction flow and the number of fish entering the fish ladder from downstream.

The lateral line probe measurements were performed by TUT and SJE on March 13 and 14, 2018 along the center of the jet core at the bottom, mid-depth and top of the water column (Figure 71). This was done for two reasons: 1) Some fish species are known to be bottom-oriented, but there is no available information on the hydraulic conditions in-situ near the bottom for attraction flow studies. 2) 2D models cannot capture the vertical distribution of the velocity and it is therefore important to determine the

physical differences between the bottom, mid (velocity in 2D models is depth-averaged and corresponds roughly to this region), and top of the water column.

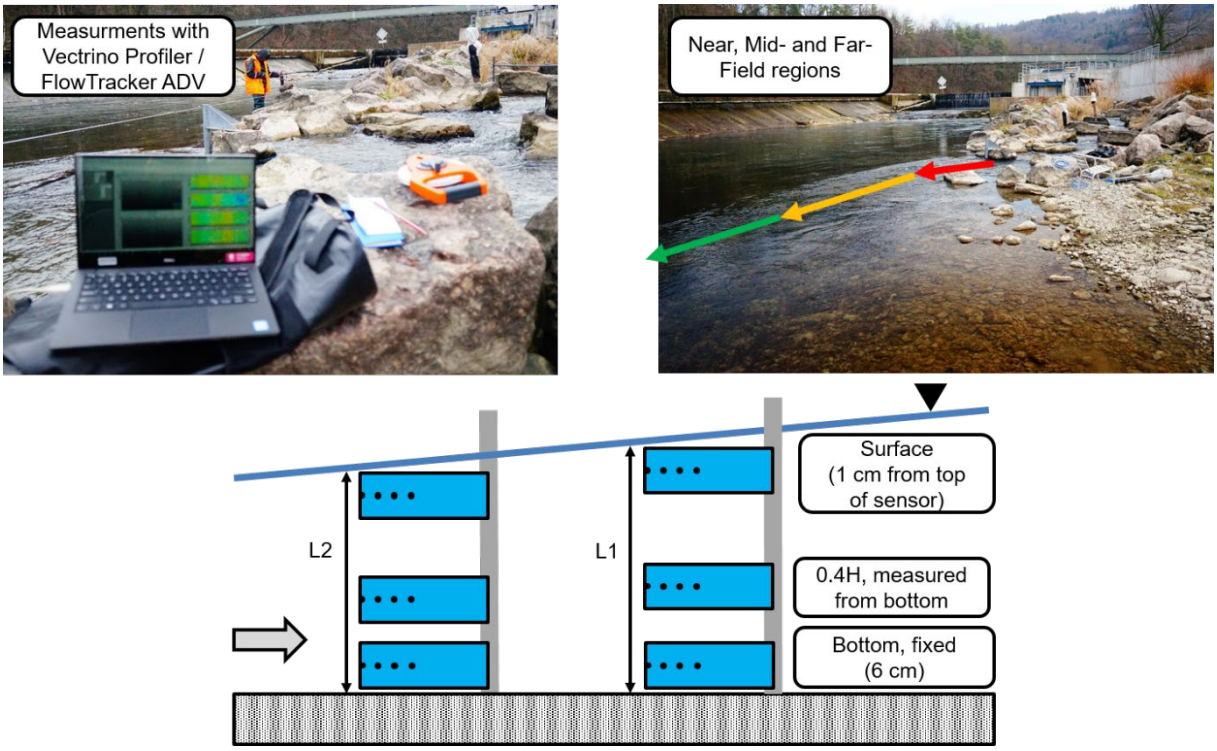

Figure 71: Top images show LLP and ADV measurement locations at the Schiffmühle case study site which correspond to the near, mid- and far-field regions of the jet core. Lower image depicts the vertical measurement locations for the LLP and ADV in order to capture the hydrodynamic conditions of the jet core at the bottom, middle and top of the water column.

3.3.3 Results

Data processing from the LLP is currently ongoing. Based on our work using the LLP as part of the live fish behaviour studies in Portugal, as series of best-performing LLP pressure metrics has been compiled and will be compared to the ADV data and are listed in Table 16.

Table 16 : Pressure-based variables from LLP measurements.

Variables	Equation
Mean pressure[1]	$\overline{p}_i = \frac{\sum_{j=1}^{n} p_{i,j}}{N}$
Mean fluctuations[1]	$\overline{p}'_i = \frac{\sum_{j=1}^{n} \lvert p_{i,j} - \overline{p}_i \rvert}{N}$
Mean front pressure ($\overline{p}_{12}$)	$\overline{p}_{12} = \frac{\sum_{j=1}^{n} p_{1,j} + p_{2,j}}{N}$
Mean pressure ($\overline{p}_{1-6}$)	$\overline{p}_{1-6} = \frac{\sum_{j=1}^{n} \frac{\sum_{k=1}^{6} p_{k,j}}{6}}{N}$
Mean front fluctuations ($\overline{p}'_{12}$)	$\overline{p}'_{12} = \frac{\overline{p}'_1 + \overline{p}'_2}{2}$

Mean fluctuations ($\overline{p}'_{1-6}$)	$\overline{p}'_{1-6} = \frac{\sum_{i=1}^{n} \overline{p}'_i}{N}$
Mean front pressure asymmetry ($\Delta\overline{p}_{12}$)	$\Delta\overline{p}_{12} = \frac{\sum_{j=1}^{n} \left(p_{1,j} - p_{2,j}\right)^2}{N}$
Mean pressure asymmetry ($\Delta\overline{p}_{1-6}$)	$\Delta\overline{p}_{1-6} = \frac{\sum_{k}^{m} \frac{\sum_{j=1}^{n} \left(p_{2k-1,j} - p_{2k,j}\right)^2}{N}}{M}$
Mean front fluctuations asymmetry ($\Delta\overline{p}'_{12}$)	$\Delta\overline{p}'_{12} = \frac{\sum_{j=1}^{n} \left(p'_{1,j} - p'_{2,j}\right)^2}{N}$
Mean fluctuations asymmetry ($\Delta\overline{p}'_{1-6}$)	$\Delta\overline{p}_{1-6} = \frac{\sum_{k}^{m} \frac{\sum_{j=1}^{n} \left(p'_{2k-1,j} - p'_{2k,j}\right)^2}{N}}{M}$

[1]Only for the variable definition above. Sensors are not considered individually.

3.3.4 Conclusion

Results for the forthcoming LLP evaluation will be published in the form of a peer-reviewed paper in 2019. Results of the attraction flow assessment can only be delivered after the hydrodynamic model is available and after the migration model based on the correlation between fish tracks and hydrodynamic measurements and modelling from the test case Altusried will be available.

4 Reference

Atkinson, E. (1994a). Vortex-tube Sediment Extractors. I: Trapping Efficiency. *Journal of Hydraulic Engineering*, 120(10), 1110-1125.

Atkinson, E. (1994b). Vortex-tube Sediment Extractors. II: Design. *Journal of Hydraulic Engineering*, 120(10), 1126-1138.

Awasthi, A.K. (2001). Desanding for Small Hydro - An Innovative Approach. *Proceedings of the 2nd International Conference 'Silting Probems in Hydropower Plants'*, Bangkok, Thailand.

Barrière, J., Krein, A., Oth, A., and Schenkluhn, R. (2015). An advanced signal processing technique for deriving grain size information of bedload transport from impact plate vibration measurements. *Earth Surf. Process. Landforms*, 40, 913– 924.

Beck, C., Albayrak, I., Boes, R.M. (2018). Improved hydraulic performance of fish guidance structures with innovative bar design. In *Proc. 12th International Symposium on Ecohydraulics*, Tokyo, Japan. https://doi.org/10.3929/ethz-b-000289463.

Beck, C. (2019). Hydraulic and fish-biological performance of fish guidance structures with curved bars. In *proc. 38th International Association for Hydro-Environmental Engineering and Research*

(IAHR) World Congress, Panama City, Panama., https://doi.org/10.3929/ethz-b-000371526. https://doi.org/10.3929/ethz-b-000371526.

Beck, C. (2020). Fish protection and fish guidance at water intakes using innovative curved-bar rack bypass systems. *VAW-Mitteilung 257* (R.M. Boes, ed). VAW, ETH Zurich, Switzerland. https://vaw.ethz.ch/en/the-institute/publications/vaw-communications/2010-2019.html.

Beschta, Robert L., and William L. Jackson. 1979. 'The Intrusion of Fine Sediments into a Stable Gravel Bed'. Journal of the Fisheries Research Board of Canada 36 (2): 204–10. https://doi.org/10.1139/f79-030.

Benitez, J. P., Dierckx, A., Nzau Matondo, B., Rollin, X., Ovidio, M. (2018). Movement behaviours of potamodromous fish within a large anthropised river after the reestablishment of the longitudinal connectivity. *Fisheries Research*, *207* (June), 140–149.

Bizzi, S., B. Blamauer, G. Braca, and M. Bussettini. 2014. 'Thematic Annexes of the Multi-Scale Hierarchical Framework'. Deliverable D2.1 Part 2. Reform - REstoring Rivers FOR Effective Catchment Management.

Bunt, C. M., Castro-Santos, T., Haro, A. (2012). Performance of fish passage structures at upstream barriers to migration. *River Research and Applications*, *28* (4), 457–478.

Bunte, K., Abt, S.R. (2001). Sampling surface and subsurface particle-size distributions in wadable gravel- and cobble-bed streams for analyses in sediment transport, hydraulics, and streambed monitoring. *Gen. Tech. Rep. RMRS-GTR-74*. Fort Collins, CO: US Department of Agriculture, Forest Service, Rocky Mountain Research Station. 428 p.

Bunte, Kristin, Steven R. Abt, John P. Potyondy, and Sandra E. Ryan. 2004. 'Measurement of Coarse Gravel and Cobble Transport Using Portable Bedload Traps'. Journal of Hydraulic Engineering 130 (9): 879–93. https://doi.org/10.1061/(ASCE)0733-9429(2004)130:9(879).

Buscombe, D., D. M. Rubin, and J. A. Warrick. 2010. 'A Universal Approximation of Grain Size from Images of Noncohesive Sediment: GRAIN SIZE FROM IMAGES OF SEDIMENT'. Journal of Geophysical Research: Earth Surface 115 (F2): n/a-n/a. https://doi.org/10.1029/2009JF001477.

Detert, M., and Weitbrecht, V. (2013). User guide to gravelometric image analysis by BASEGRAIN. *Advances in science and research* (S. Fukuoka, H. Nakagawa, T. Sumi, and H. Zhang eds.), Taylor & Francis, London, 1789-1795.

Detert, M., Johnson, E.D., Weitbrecht, V. 2017. Proof-of-concept for low-cost and non-contact synoptic airborne river flow measurements. *International Journal of Remote Sensing* 38(8–10), 2780–2807. doi:10.1080/01431161.2017.1294782.

Ebel, G. (2016). Fischschutz und Fischabstieg an Wasserkraftanlagen — Handbuch Rechen und Bypasssysteme. Ingenieurbiologische Grundlagen, Modellierung und Prognose, Bemessung und Gestaltung (Fish Protection and Downstream Passage at Hydro Power Stations — Handbook of Bar Rack and Bypass Systems. Bioengineering Principles, Modelling and

Prediction, Dimensioning and Design). 2nd edn. *Büro für Gewässerökologie und Fischereibiologie Dr. Ebel*, Halle (Saale), Germany [in German].

Fierz, Jean-Martin. 2009. 'Einfluss von Habitatsparametern Auf Die Populationsstruktur Und Biomasse von Bachforellen (Salmo Trutta Fario) Sowie Die Artenvielfalt Der Fischfauna', 3–39.

Finstad, A.G., Einum, S., Forseth, T., Ugedal, O., 2007. Shelter availability affects behaviour, size-dependent and mean growth of juvenile Atlantic salmon. *Freshwater Biology* 52, 1710–1718. https://doi.org/10.1111/j.1365-2427.2007.01799.x

Flow Science, Inc (2014): FLOW-3D Version 11.0.3 – User manual.

Flussbau AG (2017). Geschiebehaushalt Limmat, Geschiebedurchgängigkeit Streichwehre (Bedload balance Limmat, bedload conveyance of side weirs). *Technical Report* [unpublished, in German].

Forseth, T., Harby, A., Ugedal, O., Pulg, U., Fjeldstad, H.-P., Robertsen, G., Barlaup, B.T., Alfredsen, K., Sundt, H., Salveit, S.J., Skoglund, H., Kvingedal, E., Sundt-Hansen, L.E.B., Finstad, A., Einum, S., Arnekleiv, J.V., 2014. *Handbook for environmental design in regulated salmon rivers* (NINA temahefte No. 53). Norsk institutt for naturforskning.

Graham, D.J., Rollet, A.-J., Piégay, H., and Rice, S.P. (2010). Maximizing the accuracy of image-based surface sediment sampling techniques. *Water Resources Research*, 41(7), 1-12.

Gray, J.R., Laronne, J.B., Marr, J.D.G. (2010). Bedload-surrogate Monitoring Technologies, *US Geological Survey Scientific Investigations Report 2010-5091*. US Geological Survey: Reston VA.

Guthruf, J. (2008). *Fischaufstieg am Hochrhein. Koordinierte Zählung 2005/06*. Bern. 163 S.

Harb, Gabriele, Stefan Haun, Josef Schneider, and Nils Reidar B. Olsen. 2014. 'Numerical Analysis of Synthetic Granulate Deposition in a Physical Model Study'. International Journal of Sediment Research 29 (1): 110–17. https://doi.org/10.1016/S1001-6279(14)60026-3.

Haun, Stefan, and Nils Reidar B. Olsen. 2012. 'Three-Dimensional Numerical Modelling of the Flushing Process of the Kali Gandaki Hydropower Reservoir: 3D Modelling of Reservoir Flushing'. Lakes & Reservoirs: Research & Management 17 (1): 25–33. https://doi.org/10.1111/j.1440-1770.2012.00491.x.

Jocham, Stefan. 2010. 'An Approach to Link Shelter Abundance and Grain Size Distribution for the Assessment of Sediment Quality for Juvenile Atlantic Salmon'. Master`s Thesis, Trondheim, Norway: University of Stuttgart.

Kemp, Paul, David Sear, Adrian Collins, Pamela Naden, and Iwan Jones. 2011. 'The Impacts of Fine Sediment on Riverine Fish'. Hydrological Processes 25 (11): 1800–1821. https://doi.org/10.1002/hyp.7940.

Kjelland, Michael E., Christa M. Woodley, Todd M. Swannack, and David L. Smith. 2015. 'A Review of the Potential Effects of Suspended Sediment on Fishes: Potential Dredging-Related Physiological, Behavioral, and Transgenerational Implications'. Environment Systems and Decisions 35 (3): 334–50. https://doi.org/10.1007/s10669-015-9557-2.

Kzyzagorski, S., Gabl, R., Seibl, J. et al. (2016) Implementierung eines schräg angeströmten Rechens in die 3D-numerische Berechnung mit FLOW-3D. *Österr. Wasser- und Abfallw.* 68: 146. doi:10.1007/s00506-016-0299-2

Lake, Randal G, and Scott G Hinch. 1999. 'Acute Effects of Suspended Sediment Angularity on Juvenile Coho Salmon (Oncorhynchus Kisutch)'. Canadian Journal of Fisheries and Aquatic Sciences 56 (5): 862–67. https://doi.org/10.1139/f99-024.

Le Coz, J., Hauet, A., Pierrefeu, G., Dramais, G., Camenen, B. 2010. Performance of Image-Based Velocimetry (LSPIV) Applied to Flash-Flood Discharge Measurements in Mediterranean Rivers. *Journal of Hydrology* 349(1–2), 42–52. doi:10.1016/j.jhydrol.2010.05.049.

Magee, James P., Thomas E. McMahon, and Russell F. Thurow. 1996. 'Spatial Variation in Spawning Habitat of Cutthroat Trout in a Sediment-Rich Stream Basin'. Transactions of the American Fisheries Society 125 (5): 768–79. https://doi.org/10.1577/1548-8659(1996)125<0768:SVISHO>2.3.CO;2.

Meister, J. (2020). Fish protection and guidance at water intakes with horizontal bar rack bypass systems. *VAW-Mitteilung 258* (R.M. Boes, ed.). Laboratory of Hydraulics, Hydrology and Glaciology, ETH Zurich, Switzerland.

Meister, J.; Fuchs, H.; Beck, C.; Albayrak, I.; Boes, R.M. (2020a). Head Losses of Horizontal Bar Racks as Fish Guidance Structures. Water, 12(2): 475. http://dx.doi.org/10.3390/w12020475.

Meister, J.; Fuchs, H.; Beck, C.; Albayrak, I.; Boes, R.M. (2020b). Velocity Fields at Horizontal Bar Racks as Fish Guidance Structures. Water, 12(1): 280. http://dx.doi.org/10.3390/w12010280

Meusburger, H. (2002): Energieverluste an Einlaufrechen von Flusskraftwerken. VAW Mitteilungen Nr. 179 (H.-E. Minor, ed.), ETH Zürich. http://people.ee.ethz.ch/~vawweb/vaw_mitteilungen/179/179_g.pdfMtalo, F. (1988). Geschiebeabzug aus Kanälen mit Hilfe von Wirbelröhren (Bedload diversion from channels with vortex tubes). *Report No. 58*, Hydraulic Research Institute Obernach, Technical University of Munich, Germany [in German].

Michel, Christian, Heike Schmidt-Posthaus, Patricia Burkhardt-Holm, and John Richardson. 2013. 'Suspended Sediment Pulse Effects in Rainbow Trout (Oncorhynchus Mykiss) — Relating Apical and Systemic Responses'. Canadian Journal of Fisheries and Aquatic Sciences 70 (4): 630–41. https://doi.org/10.1139/cjfas-2012-0376.

Müller-Hagmann, M. (2017). Hydroabrasion by High-Speed Sediment-Laden Lows in Sediment Bypass Tunnels. In R.M. Boes (Ed.), *VAW Mitteilungen Nr. 239*. Laboratory of Hydraulics, Hydrology and Glaciology (VAW), ETH Zurich, Switzerland.

Noonan, M. J., Grant, J. W. A. & Jackson, C. D. (2012). A quantitative assessment of fish passage efficiency. *Fish and Fisheries*, *13* (4), 450–464.

Olsen, Nils Reidar B. 1994. 'SSIIM - a Three-Dimensional Numerical Model for Simulation of Water and Sediment Flow'. Transactions on Ecology and the Environment 8.

Osmundson, D. B., R. J. Ryel, V. L. Lamarra, and J. Pitlick. 2002. 'Flow–Sediment–Biota Relations: Implications For River Regulation Effects On Native Fish Abundance'. Ecological Applications 12 (6): 1719–39. https://doi.org/10.1890/1051-0761(2002)012[1719:FSBRIF]2.0.CO;2.

Peter, A., Mettler, R., Schölzel, N. (2016). Kurzbericht zum Vorprojekt „ PIT-Tagging Untersuchungen am Hochrhein – Kraftwerk Rheinfelden ". 45 p.

Rachelly, C., Albayrak, I., Boes, R.M., Weitbrecht, V. (2019). Bed-Load Diversion with a Vortex Tube System. *Proceedings of the 38th International Association for Hydro-Environmental Engineering and Research World Congress (IAHR 2019), Panama City, Panama*, 5900-5909.

Rickenmann, D., Turowski, J.M., Fritschi, B., Klaiber, A., Ludwig, A. (2012). Bedload transport measurements at the Erlenbach stream with geophones and automated basket samplers. *Earth Surface Processes and Landforms*, 37, 1000-1011.

Rüther, Nils, Sonja Huber, Stephan Spiller, and Jochen Aberle. 2013. 'Verifying a Photogrammetric Method to Quantify Grain Size Distribution of Developed Armor Layers'. In Proceedings of the 35th IAHR Congress, Chengdu, China. Vol. 7. Schälchli, Ueli. 1992. 'The Clogging of Coarse Gravel River Beds by Fine Sediment'. Hydrobiologia 235–236 (1): 189–97. https://doi.org/10.1007/BF00026211.

Stähly, S., Friedrich, H., Detert, M. (2017). Size Ratio of Fluvial Grains' Intermediate Axes Assessed by Image Processing and Square-Hole Sieving. *Journal of Hydraulic Engineering*, 143(6).

Schultz, Al, Ha Malcolm, M Linklater, Ar Jordan, T Ingleton, and Sda Smith. 2015. 'Sediment Variability Affects Fish Community Structure in Unconsolidated Habitats of a Subtropical Marine Park'. Marine Ecology Progress Series 532 (July): 213–26. https://doi.org/10.3354/meps11311.

Summerfelt, L. . & Smith, R. C. (1990). Anaesthesia, surgery and related techniques. In P. Schreck & B. Moyle (Hrsg.), *Methods for Fish Biology* (S. 213–272). American Fisheries Society: Bethesda, Maryland.

Szabo-Meszaros, Marcell. 2015. 'Shelter for Juvenile Atlantic Salmon: Availability and Prediction in Rivers with and without Hydropower Regulation.' Master`s Thesis, Trondheim, Norway: NTNU.

Teichert, M. A. K., E. Kvingedal, T. Forseth, O. Ugedal, and A. G. Finstad. 2010. 'Effects of Discharge and Local Density on the Growth of Juvenile Atlantic Salmon Salmo Salar'. Journal of Fish Biology 76 (7): 1751–69. https://doi.org/10.1111/j.1095-8649.2010.02614.x.

Thielicke, W., Stamhuis, E. J. 2014. PIVlab – Towards User-Friendly, Affordable and Accurate Digital Particle Image Velocimetry in MATLAB. *Journal of Open Research Software* 2:e30. doi:10.5334/jors.bl.

USBR - US Bureau of Reclamation (2006). Fish protection at water diversions - a guide for planning and designing fish exclusion facilities. Denver (CO): US Department of the Interior. p. 480.

VAW (2001). Kraftwerk Schiffmühle (Hydropower plant Schiffmühle). *VAW-Report 4158*, ETH Zurich, Laboratory of Hydraulics, Hydrology and Glaciology (VAW), Switzerland [unpublished, in German].

VAW (2017). Wirbelröhre Kraftwerk Turgi (Vortex tube hydropower plant Turgi). *VAW-Report 4343*, Laboratory of Hydraulics, Hydrology and Glaciology (VAW), ETH Zurich, Switzerland [unpublished, in German].

Voser, P., Bolliger, A. (2004). Die Fischfauna im Aargauer Limmattal. Umwelt-Aargau, 26, 5–8.

Westerweel, J., Scarano, F. 2005. Universal outlier detection for PIV data. Experiments in Fluids 39(6), 1096–1100. doi:10.1007/s00348-005-0016-6.

Wilkes, Martin A., Ian Maddock, Fleur Visser, and Michael C. Acreman. 2013. 'Incorporating Hydrodynamics into Ecohydraulics: The Role of Turbulence in the Swimming Performance and Habitat Selection of Stream-Dwelling Fish'. In Ecohydraulics, 7–30. Wiley-Blackwell. https://doi.org/10.1002/9781118526576.ch2.

Wilmsmeier, L., Schölzel, N., Peter, A. & Baumann y Carmona, A. (2020). Fischzählbecken - die unterschätzte Bedeutung der Reusenkehle. *WasserWirtschaft*, *110* (2–3), 55–62.

Woschitz, G., Gumpinger, C., Ratschan, C., Guttmann, S. & Zeiringer, B. (2020). *Richtlinie 1/2003 i.d.F. 2020 Mindestanforderungen bei der Überprüfung von Fischaufstiegshilfen (FAH) und Bewertung der Funktionsfähigkeit. Richtlinien der Fachgruppe Fischereisachverständige beim Österreichischen Fischereiverband*. 47 S.

Wyss, C.R., Rickenmann, D., Fritschi, B., Turowski, J.M., Weitbrecht, V., Boes, R.M. (2016a). Measuring Bed Load Transport Rates by Grain-Size Fraction Using the Swiss Plate Geophone Signal at the Erlenbach. *Journal of Hydraulic Engineering*, 142(5): 04016003.

Wyss, C.R., Rickenmann, D., Fritschi, B., Turowski, J.M, Weitbrecht, V., Boes, R.M. (2016b). Laboratory flume experiments with the Swiss plate geophone bed load monitoring system: 1. Impulse counts and particle size identification. *Water Resources Research*, 52, 7744-7759.

Wyss, C.R., Rickenmann, D., Fritschi, B., Turowski, J.M, Weitbrecht, V., Boes, R.M. (2016c). Laboratory flume experiments with the Swiss plate geophone bed load monitoring system: 2. Application to field sites with direct bed load samples. *Water Resources Research*, 52, 7760-7778.

Zabah E. 2018. *KWS_26-03-2018.zip, KWS_26-03-2018ply.zip*. Regionalwerke Baden AG (pers. communication).